ABSTRACT

Title of Document:	NUMERICAL PARAMETRIC STUDY OF THE THERMOMECHANICAL EFFECT OF ENCAPSULATION ON A WELDED BEAM LEAD COMPONENT
	Joshua David Akman, M.S. Mechanical Engineering, 2014
Directed By:	Professor Abhijit Dasgupta Department of Mechanical Engineering

Encapsulation of components and assemblies has become widespread in the design of electronic products, providing protection from the environment and enhancing reliability. In this thesis, computational simulations are used to parametrically investigate the thermomechanical role played by the encapsulant when a beam-lead component is welded to slender copper busbars, encapsulated in a polymeric encapsulant, and subjected to temperature cycling. The parametric studies are conducted in two phases, using simplified two-dimensional finite element models.

In the first phase, a parametric design space is generated to systematically vary the encapsulant's thermomechanical properties, namely the Young's modulus and Coefficient of Thermal Expansion. A gull wing geometry is introduced into the lead of the component as a stress relief feature. In this case, a ramp thermal loading profile is used to understand the physics of this design and to provide relative comparisons between different combinations of

the encapsulant's material properties within the design space. Response surface models are generated over the design space.

In the second phase, a Taguchi Design of Experiments (DOE) approach, based on orthogonal arrays, is used to analyze the effects of multiple design parameters under cyclic thermal loading. This includes encapsulant properties (a subset of the properties investigated in the first phase), encapsulant dimensions, lead geometry and dimensions, and busbar dimensions. Lead geometry is considered with and without stress relief features. The loading used in this phase is three temperature cycles between -40°C and 90°C. The primary areas of concern (response variables) in both studies are the component lead and interconnect regions. Deformation and stress states in these critical regions are compared. Main factor effects and selected parameter interactions are computed in accordance with the Taguchi orthogonal arrays, to understand the dominant parameters and parameter interactions for cyclic thermomechanical stresses in this encapsulated assembly.

NUMERICAL PARAMETRIC STUDY OF THE THERMOMECHANICAL EFFECT OF ENCAPSULATION ON A WELDED BEAM LEAD COMPONENT

By

Joshua David Akman

Thesis submitted to the Faculty of the Graduate School of the
University of Maryland, College Park, in partial fulfillment
of the requirements for the degree of
Master of Science
2014

Advisory Committee:
Professor Abhijit Dasgupta, Chair
Professor Bongtae Han
Associate Professor Patrick McCluskey

© Copyright by
Joshua David Akman
2014

Table of Contents

Table of Contents ii
List of Tables iv
List of Figures v
Chapter 1: Introduction 1
1.1 Background and Motivation 1
1.2 Literature Review 3
1.2.1 Parametric study – Effects of encapsulant properties on a welded beam lead SMT component under thermal cycling using Finite Element Analysis 3
1.2.2 Design optimization of an encapsulated beam-lead component using a combined FEM and DOE approach 6
Chapter 2: Parametric study – Effects of encapsulant properties on a welded beam lead SMT component under thermal cycling using Finite Element Analysis 11
2.1 Approach 11
2.2 Component and Assembly Configuration 12
2.3 Finite Element Modeling 17
2.3.1 Thermal FEA Model – Configuration and Geometry 17
2.3.2 Material Properties 20
2.3.3 Boundary Conditions 23
2.3.4 Mesh Refinement Study 25
2.4 Parametric Study 26
2.4.1 Parametric Design Space 27
2.4.2 Loading Conditions 30
2.5 Results and Discussion 31
Section 2.5.1 Axial Forces and Bending Moments 31
Section 2.5.2 Elastic and Plastic Strain 46
Chapter 3: Design optimization of an encapsulated beam-lead component using a combined FEM and DOE approach 56
3.1 Approach 56
3.1.1 Assembly Configuration, Boundary Conditions, and Loading Conditions 57
3.2 Screening Study – Background, Test Design, and Approach 59
3.2.2 Test matrix design 66
3.3.1 Screening study - equivalent strain results 70
3.4 Characterization Study – Background, Factor Selection, and Test Design 75
3.4.1 Factor selection 75
3.4.2 Test matrix design 79
3.5 Characterization Study - Results and Discussion 83
3.5.1 Characterization study - equivalent strain results 83
Chapter 4: Summary and General Conclusions 91
Chapter 5: Thesis Contributions 94
5.1 Parametric study – Effects of encapsulant properties on a welded beam lead SMT component under thermal cycling using Finite Element Analysis 94

5.2 Design optimization of an encapsulated beam-lead component using a combined FEM and DOE approach 94
Chapter 6: Limitations and Future Work 96
Appendices 98
Bibliography 113

List of Tables

Table 1. Comparison of typical beam lead bonding techniques [46] 14
Table 2. Out-of-plane measurements of encapsulant assembly for Figure 5............. 17
Table 3. Material properties (Copper plastic properties are in Figure 9).................... 22
Table 4. Variables from Equation (2) 24
Table 5. Example of temp. dependent properties for room temp. E=1GPa, CTE=100ppm/C 29
Table 6. P_{11} of the lead adjacent to the EMC as a function of encapsulant properties 36
Table 7. P_{11} of the lead adjacent to the weld as a function of encapsulant properties 37
Table 8. P_{11} of the busbar adjacent to the weld as a function of encapsulant properties 38
Table 9. P_{22} values at the weld as a function of encapsulant properties 39
Table 10. P_{12} values at the weld as a function of encapsulant properties 40
Table 11. Axial force comparison values (N) through cross-section a various locations for multiple encapsulant property combinations.. 46
Table 12. Terms of generalized Coffin-Manson equation 47
Table 13. PEMAG + ε_{el-eq} for the lead adjacent to the EMC as a function of encapsulant properties... 52
Table 14. PEMAG + ε_{el-eq} for the lead adjacent to the weld as a function of encapsulant properties... 53
Table 15. PEMAG+ ε_{el-eq} values for lead bend as a function of encapsulant properties 54
Table 16. PEMAG + ε_{el-eq} for busbar adjacent to the weld as a function of encapsulant properties.. 55
Table 17. ATC profile characteristics 57
Table 18. Taguchi DOE screening study - factors and levels.................................... 59
Table 19. Length of busbar and encapsulant as a function of diode region................ 62
Table 20. L_{12} Taguchi screening design 68
Table 21. Equivalent total strain values for the screening study at various locations of interest.. 70
Table 22. Response table for main effect means and parameter rankings.................. 72
Table 23. Anova for L_{12} screening study 73
Table 24. Linear model fit to main effect means terms for screening study 74
Table 25. Taguchi DOE characterizing study - factors and levels 76
Table 26. L_{27} Taguchi characterization design 82
Table 27. Equivalent total strain values for the characterization study at locations of interest.. 84
Table 28. Parameter factors for characterization study 87
Table 29. Response table for main effect means and parameter rankings.................. 88
Table 30. Anova for L_{27} screening study 88
Table 31. Linear model fit to main effect means terms for characterization study 89

List of Figures

Figure 1. Flowchart of Approach for Study 1 12
Figure 2. SBR Diode schematic [44] 12
Figure 3. Resistance spot welding schematic [45] 13
Figure 4. Assembly schematic (a) Global Schematic (b) Gull wing leads local schematic 15
Figure 5. Top view schematic 16
Figure 6. (a) Schematic of thermal FEA model (b) Left half of thermal 2D FEA model (c) Right half of thermal 2D FEA model 18
Figure 7. Two localized views of the component, interconnect, and busbar meshes . 19
Figure 8. Spot weld region in the finite element model 19
Figure 9. Regular and locally hardened copper stress-strain curves 22
Figure 10. Pin displacement BC constraint along on the bottom left corner of the model 23
Figure 11. BC constraining the bottom of the model (top = left half, bottom = right half) 23
Figure 12. Displacement BC constraining the right end of the model in the horizontal x-axis 23
Figure 13. (a) Constraint equation BC on right edge of model (b) Constraint equation table 25
Figure 14. Mesh Refinement Study - meshing schemes 25
Figure 15. Potential Energy plot from mesh refinement study 26
Figure 16. Parametric design space – room temperature encapsulant material properties 28
Figure 17. Parametric design space with regions of different encapsulant properties 29
Figure 18. Thermal loading profile 31
Figure 19. Local view showing the locations of force & bending moment measurements - (i) Lead adjacent to EMC (ii) Lead adjacent to weld (iii) Weld region (iv) Busbar adjacent to weld 34
Figure 20. Response surface (top) and contour (bottom) for the axial force values calculated at the component lead adjacent to the EMC package 36
Figure 21. Response surface (top) and contour (bottom) for the axial force values calculated at the component lead adjacent to the weld region 37
Figure 22. Response surface (top) and contour (bottom) for the axial force values calculated at the busbar adjacent to the weld region 38
Figure 23. Response surface (top) and contour (bottom) for the peel force values calculated at the weld region 39
Figure 24. Response surface (top) and contour (bottom) for the shear force values calculated at the weld region 40
Figure 25. Schematic of deformed geometry of the encapsulant through the cross section adjacent to the EMC region 42
Figure 26. u_1 node locations 42
Figure 27. Difference in encapsulant edge and center u_1 nodal displacement 43
Figure 28. Measurement locations for the axial force comparisons through cross-section 45

Figure 29. Local view of locations of equivalent total strain measurements - (i) Lead adjacent to EMC (ii) Lead bend (iii) Lead adjacent to weld region (iv) Busbar adjacent to weld region 48
Figure 30. Response surface (top) and contour (bottom) for the average equivalent strain values calculated at the lead adjacent to the EMC package 52
Figure 31. Response surface (top) and contour (bottom) for the average equivalent strain values calculated at the lead adjacent to the weld region 53
Figure 32. Response surface (top) and contour (bottom) for the average equivalent strain values calculated at the lead bend 54
Figure 33. Response surface (top) and contour (bottom) for the average equivalent strain values calculated at the busbar adjacent to the weld regions 55
Figure 34. Flowchart of Approach for Study 2 57
Figure 35. Accelerated thermal cycle profile 58
Figure 36. (a) Global schematic (b) Flat configuration (c) Gull wing configuration . 62
Figure 37. Length of encapsulation as a function of the diode region 62
Figure 38. Busbar thickness adjustment for screening study 64
Figure 39. Taguchi L_{12} orthogonal array 68
Figure 40. Main effects of parameters from screening study - (a) individual parameters (b) all parameters plotted side-by-side 72
Figure 41. Plots of the residual means of model fit for screening study 74
Figure 42. Encapsulant property sets selected from the design space in Chapter 2 ... 77
Figure 43. (a) Global schematic (b) Flat lead (c) High gull wing lead (d) Low gull wing lead 78
Figure 44. Taguchi L_{27} orthogonal array 81
Figure 45. Taguchi L_{27} linear graph 81
Figure 46. Maximum total equivalent strain regardless of location: (top) parameter main effect plots for means (b) parameter interaction plots 87
Figure 47. Plots of the residual means of model fit for characterization study 90

Chapter 1: Introduction

This chapter contains an introduction to the problem statement. This includes background and motivation for the study, as well as a literature review.

1.1 Background and Motivation

Potting and encapsulation of components and circuit cards have become an integral part of the design of electronic products and assemblies. Components and assemblies are encapsulated for protection from the environment. The protection required varies depending on the environmental and operational conditions, but often includes protection from moisture ingress, ionic contaminants and particulates, handling and transport, shock and cyclic loading, and any other environmental factor that a particular device or component will experience through its lifetime. The large majority of today's mircroelectronic devices, for instance, are plastically encapsulated. There are several major encapsulant technologies: molding, glob-top, potting, underfill, and printing encapsulation. Encapsulation techniques can vary based on the desired material and application.

The focus of the particular studies in this thesis is on the thermomechanical stress of an electronic assembly consisting of a leaded component that is encapsulated in a large polymeric structure. In this case the encapsulant structure is significantly larger than in many conventional applications such as coating or underfilling. Mechanical stresses are generated in the assembly from thermal loading or cycling, due to expansion mismatches between the encapsulant and the remaining materials in the

assembly. This study is conducted purely through simulations based purely on finite element analysis (FEA) using commercial FEA software. This type of simulation based exploration, allows for rapid comparisons between potential design and material candidates.

Two main studies are conducted. In the first study, a single beam-lead surface mount technology (SMT) component, with a built in compliant gull wing formation, is welded to slender copper busbars and encapsulated in a polymeric material. The material properties of the encapsulant, namely the Young's modulus and CTE, are systematically varied in a design space that bounds the properties typical materials use in encapsulation applications. In the second study, a combined Design of Experiments (DOE) and FEA approach is employed. The assembly in this study the same as the one used in the first study, however some additional features are varied as part of the DOE study. The parameters varied include the encapsulant material properties, encapsulant width, lead dimensions and geometry, and busbar dimensions. In both studies the objective is to determine the effect of varying these material properties and design parameters on the deformation and stresses in the SMT component and its interconnect regions. Typically, the fatigue life models used to analyze the durability of such designs are based on a strain based model developed by Coffin-Mason [1] and are given as follows in equation (1):

$$\frac{\Delta\varepsilon_{el}}{2} + \frac{\Delta\varepsilon_{pl}}{2} = \frac{\left(\sigma_f - \sigma_m\right)}{E}\left(2N_f\right)^b + \varepsilon'_f\left(2N_f\right)^c \qquad (1)$$

Although no cycles to failure or acceleration factors are calculated in this paper, the fatigue model is instructive because it highlights which elastic and plastic strain parameters are the metrics of interest for this study. The next two sections contain literature reviews relating to the two studies conducted in this thesis.

1.2 Literature Review

A brief literature review is conducted for the topic in each of the two studies in this thesis. Additional literature review may be also included in introduction section of each of the two studies.

1.2.1 Parametric study – Effects of encapsulant properties on a welded beam lead SMT component under thermal cycling using Finite Element Analysis

This chapter contains a study that parametrically examines the effects of the encapsulant properties on the deformation and stress state of a SMT component and interconnects. A parametric design space is generated to parametrically vary the encapsulant properties, and the thermomechanical reliability is examined.

There are many studies in the literature examining the thermomechanical reliability of encapsulated components and interconnects. They can be divided into several classifications such as: embedded passive & active components, underfilled components, conformal coatings, and potted or laminated components and assemblies. Lee [2] and Qiu *et al.* [3] examined the reliability of passive components, such as capacitors and resistors that are embedded directly into the PCB substrate. Chen *et al.* [4] examined the thermomechanical reliability of high-density three-dimensional integrated package design, whereby passive and active components were

embedded into the package using a combination of a build-up process and epoxy. FEM analysis showed that thermal expansion mismatch between the encapsulant and embedded copper was the greatest source of failure.

Many studies have also been conducted on the use of an encapsulant for reliability improvement of Ball Grid Array (BGA) and flip-chip interconnects. Suryanarayana *et al.* [5] examined the effects of an underfill encapsulant (an epoxy encapsulant) on the thermal fatigue life of solder joints of a flip-chip component. Okura *et al.* [6] and Darbha *et al.* [7] examined the effects of underfills on thermomechanical fatigue durability of flip-chip-on-board (FCOB) and chip scale package (CSP) assemblies. Okura performed parametric studies, using FEM, to examine the effects of varying the Young's modulus and CTE of select underfills and compliant interposers on the fatigue durability of FCOBs and CSPs. Okura showed that fatigue durability could be enhanced by introducing underfill encapsulation. Furthermore, Okura also show that the amount of fatigue enhancement was strongly dependent on the material properties themselves, increasing as the modulus and CTE are increased. Zhong [8] performed a Design of Experiments (DOE) study that examined the fatigue durability of Flip-Chip-On-Board (FCOB) assemblies with and without underfill and with and without encapsulation. The components without underfill or encapsulation performed the worst. Interestingly, components with both underfill and encapsulation did not perform the best. This may be due to the difference in thermal expansion between the underfill and encapsulant. Young [9] and Burnette *et al.* [10] showed that underfills can enhance the reliability of BGA packages under thermal cycling. One interesting observation made by Burnette was that encapsulants with very large CTE values

actually failed faster than components without underfill. This highlights the importance of the encapsulant material properties and the consideration required for the encapsulant material selection process. There are many more examples in the literature of such reliability studies of underfilled component interconnects.

Pippola *et al.* [11] examined the effects a silicone based conformal coating and a polyurethane casting material had on the reliability of an electronic assembly under temperature-humidity and temperature-shock testing. In all tests, samples with protective coating or casting failed faster than those without protective materials. Additionally the failure mode shifted between samples with and without protective materials. Pippola showed that protective materials with large CTE values actually produced harsher mechanical stresses under thermal loading than those without protective materials. This again reiterates that although encapsulation can offer protection from environmental conditions, careful consideration must be given to the selection of the encapsulant. Zhang [12] used FEA modeling to examine a proposed a solder ball coating process for BGA packages as an alternative to underfilling. Zhang showed that coating can help improve the reliability and thermomechanical durability of BGA solder joints. Zhang also showed that increasing the modulus of the coating increased the solder joint fatigue life while increasing the CTE showed a non-linear effect on the solder fatigue life. A comprehensive review of coating materials, techniques and reliability considerations is provided by Licari [13].

Whole components and circuit cards are also potted or encapsulated in order to increase reliability. This typically occurs in larger components such as Multi-Chip-

Modules (MCM) [14-15], or in large assembly applications that require potting or encapsulation of entire modules such as automotive [16-17], under water [18], LED lighting [19] photovoltaics [20-22], among others. This is done to help enhance reliability and provide protection environmental loading conditions. The parametric study performed in this chapter focuses on encapsulation on this scale.

Several of the studies previously presented [8, 10-12] showed that although encapsulation has the potential to improve an assembly or component's reliability, it also has the potential to decrease reliability. This highlights how critical the encapsulant material selection is to the thermomechanical reliability of an assembly. Design and material selection are often some of the most complicated and costly product development processes. By parametrically varying the assembly's encapsulant's material properties (CTE and Young's modulus), approximations of different materials' effects on the package and interconnect stresses can be rapidly compared. There is significant amount of data in the literature regarding typical encapsulant material properties and considerations for such applications [23-27]. The encapsulant material property parametric study is designed based on material properties found in literature.

1.2.2 Design optimization of an encapsulated beam-lead component using a combined FEM and DOE approach

Whereas the previous chapter exclusively focuses on the effect of the encapsulant's material properties, this study examines the contributions of multiple design parameters on the deformation and stress states of an encapsulated beam-lead SMT

(Surface Mount Technology) component and its interconnects under cyclic thermal loading. The assembly of interest is similar to the one in the previous chapter, consisting of a beam-lead component that is welded to copper busbars and encapsulated in polymeric encapsulant. However, in this study, several design parameters are varied such as the encapsulant material properties, encapsulant out-of-plane thickness, lead dimensions and geometry, and busbar dimensions.

The assembly is modeled using commercial FEM software, and a combined FEM and Taguchi DOE approach is utilized [28-29]. Conventional DOE methods sometimes lend themselves to physical experiments. One such reason is that physical experiments used in DOE process control and design, often allow the experimenter to produce many replicates for the same conditions. This may not be possible when using models or simulations. With this consideration in mind, there still exist many examples in the literature of combined simulation and DOE approaches [30-35].

Typical SMT devices utilize specific lead designs (i.e. gull wing, J-shape) in order to provide compliance between the component, substrate and joint region. This is particularly critical to enhance a component's fatigue durability under cyclic loading. In this study, two gull wing lead designs are considered, as well as a flat beam-lead design. This difference in the structural compliance of these lead designs will contribute to the stresses incurred by the package and joint under thermal cycling. Kotlowitz [36-38] has previously developed analytical models to estimate lead compliance (or stiffness) for many surface mount lead designs based on the lead geometry and material properties. However, there exist several design differences

between the assembly in this study and those modeled by Kotlowitz. In Kotlowitz's cases, mechanical stresses are driven primarily by thermal expansion mismatches between the PCB substrate, solder joint, and lead. In the present study, the surface mount component is fully encapsulated in a polymeric material. The encapsulant therefore changes the overall system's structural stiffness and load transfer. This more complex heterogeneous assembly makes it hard to predict the contribution of a compliant lead type versus the contribution of the encapsulant. This is why a numerical simulation and a DOE approach are used.

As previously mentioned, in this study several design parameters are varied including the lead dimensions and geometry. In this case, a beam lead component is formed into low-profile and high-profile gull wing leads, in order to add varying amounts of compliance in the load-train for the load transfer between the component and the busbar through the interconnect. Emerick *et al.* [39] examined the reliability enhancement of a low-profile Thin Small Outline Package (TSOP) with gull wing leads by encapsulation. Emerick noted that although low-profile TSOP components allow for miniaturization, they are significantly less compliant than high-profile gull wing leads and therefore lead to solder joint failures during thermal cycling. Emerick found that encapsulation of the low-profile joint was able to enhance reliability during thermal cycling.

There exist examples in the literature where additional assembly features, such as the dimensions and geometric features of the assembly are also varied with a parametric approach. Cummings [40] compared multiple stress relief geometries for a soldered

component lead in encapsulated assemblies under mechanical loading. In this study the lead bends were covered in various sleeve materials while the whole lead was encapsulated in epoxy and foam encapsulants. Cummings concluded that leads with sleeving had enhanced performance while the stiff encapsulants were a large source of loading on the joints. Guofeng *et al.* [35] looked at the influence influences of material properties and structural geometries on thermal fatigue reliability of a TSV interposer package using a combined FEM and Taguchi approach. Guofeng concluded that underfill encapsulant properties had the most influence on the solder joint fatigue durability, with a high modulus and low CTE producing the optimal results. Hsieh and Lee [33] examined the reliability of a multilevel 3D-WLP using a combined FEA and DOE approach. As part of the study, Hsieh and Lee varied both the assemblies geometric features as well the modulus and CTE of the Ajinomoto Built-up Film (ABF) used to coat the die between levels. Hsieh and Lee found that the material properties and geometric features greatly influenced the thermal stress distributions. More examples of this type of approach in exist in the literature. Similar to these studies, the results of this study will help understand the contributions and interactions of the encapsulant properties and assembly geometry on the stresses in the assembly under thermal cycling.

There is some gap in the literature for larger laminate assemblies, where whole components are encapsulated that do not utilize of solder joint interconnects. Typically, the thermomechanical durability studies on encapsulated assemblies focus on solder interconnect failures, however the assembly of this study shifts the focus to a welded interconnect and the region surrounding the interconnect. This type of

assembly design is not as common in microelectronics and is often found in larger scale applications. While there are some studies on the thermal and thermomechanical stress analysis of beam lead components [41-42], there are few that focus on encapsulated and welded assemblies. Furthermore, there is also a lack of large parametric studies that explore different design parameters for an encapsulated and welded assembly.

Chapter 2: Parametric study – Effects of encapsulant properties on a welded beam lead SMT component under thermal cycling using Finite Element Analysis

In this chapter, the effects of encapsulation on a beam lead component subjected to thermal loading are examined. Encapsulated (or potted) surface mount devices, such as the one in this study, are incorporated into electronic assemblies for various applications. The use of an encapsulant can range from encapsulating a single component to the potting of an entire circuit cards or assembly. The encapsulation serves multiple purposes such as protection from moisture and corrosion, shock loading, fatigue and other failure modes. Common applications include areas such as automotive, telecommunications, microelectronics, photovoltaics and others. This chapter contains a study that parametrically examines the effects of the encapsulant properties on the deformation and stress state in the component and interconnects, using finite element simulations.

2.1 Approach

The simulation model consists of a welded discrete surface mount component with beam leads, which is laminated within an encapsulant material. A finite element model is developed to simulate and capture the deformation and stress states in various important regions of the assembly, due to thermal expansion mismatches within the assembly *in-situ* in the embedded condition. Inputs to the models are parametrically varied to systematically examine their effects. In this particular study, only the encapsulant material properties are varied. A 2-dimensional design space is defined, where the stiffness and the coefficient of thermal expansion (CTE) of the

encapsulant material are parametrically varied. A visual flowchart of this approach is seen in Figure 1.

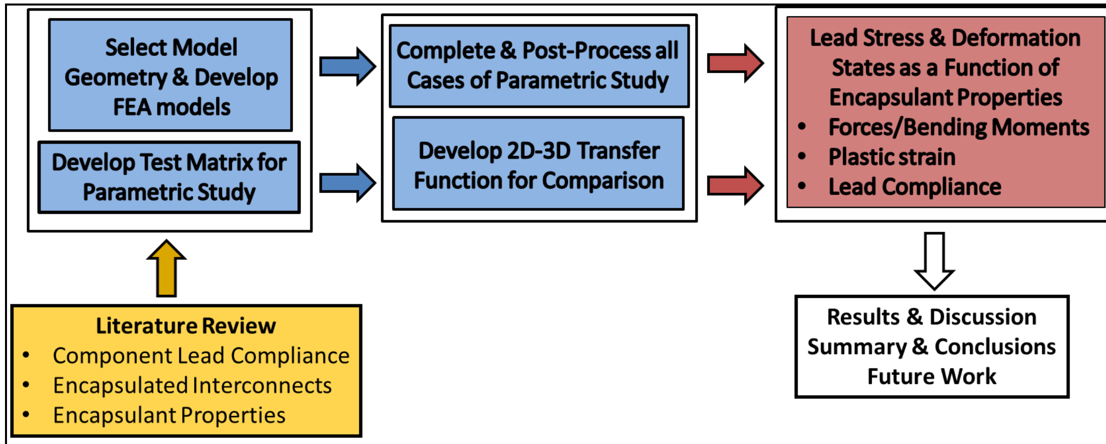

Figure 1. Flowchart of Approach for Study 1

2.2 Component and Assembly Configuration

For this study the component of interest is a low profile beam lead commercial-off-the-shelf (COTS) component. This component form factor is typically seen in discrete active and passive components such as diodes and capacitors. An example such a component is a beam lead Super Barrier Rectifier (SBR) diode, depicted in Figure 2 and the technical drawing in the Appendix section. This particular diode has a relatively flat profile, consisting of two flat beam leads, one for the anode and one for the cathode.

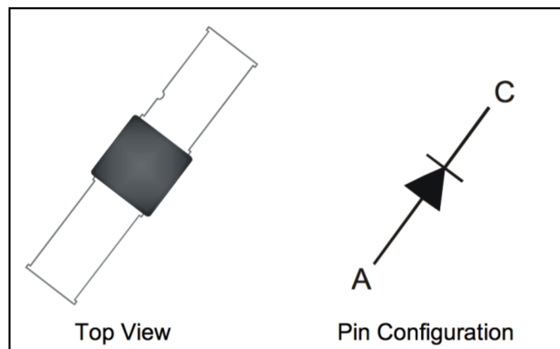

Figure 2. SBR Diode schematic [44]

The full assembly considered in this study consists of the aforementioned beam lead component, interconnected to slender strips of copper busbar, and encapsulated in a polymeric encapsulant. Due to the nature of this assembly, mechanical stresses are generated during thermal cycling, as a result of thermal expansion mismatches between various constituents. In order to mitigate some of these thermomechanical stresses, a typical design solution is to incorporate some compliance in the component-busbar interconnects by forming a gull wing bend in the component leads.

Several bonding techniques are commonly used for interconnecting such beam lead components to their respective substrates or assemblies. These techniques include thermocompression or thermosonic bonding, resistance welding, soldering, and even conductive epoxy bonding. When selecting a bonding method, several factors should be taken into consideration such as cost, substrate material, manufacturing needs and capabilities, requirements for bond strength, among other factors. Table 1 shows a comparison of a few of these bonding methods, including the advantages and disadvantages of each.

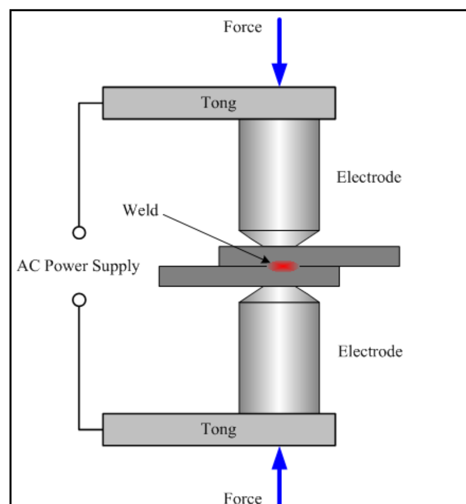

Figure 3. Resistance spot welding schematic [45]

In this particular study, the component leads are assumed to be spot welded (resistance weld) to copper busbars. This method is fairly robust and versatile, causing negligible deformation to the leads and allowing for a strong mechanical bond. This type of bonding method is relatively low cost, can work for a variety of metals and substrates, and the strength of the weld can be varied by the amount of energy put into the weld. A schematic of this welding method is included in Figure 3 and a few highlights are included in Table 1.

Table 1. Comparison of typical beam lead bonding techniques [46]

	Resistance Weld		Thermocompression		Epoxy Attach	
	– Manual	– Auto	– Manual	– Semi-Auto	– Manual	– Auto
	Hard Substrates Soft Substrates Lead Frame Packages	N/A	Hard Substrates Lead Frame Packages	Hard Substrates	Soft Substrates Hard Substrates Lead Frame Packages	Soft Substrates Hard Substrates Lead Frame
Estimated UPH	200	–	200	120-180	180	1000
Estimated Cost	7K	–	8 K	8-28 K	5.5 K	50 K
Major Vendors	Hughes Unitek	None	K&S Westbond Unitek	K&S D.P. Veen	Westbond Laurier	ASM
Major Advantages	Low Temperature Low Pressure Wide Range of Metals Easy to Use & Low Cost Simple Maintenance Excellent Bond Strength		Widely Accepted Many Equipment Vendors Low Cost Semi-Auto Available Minimum Maintenance Excellent Bond Strength		Any Substrate Most Finish Metals OK. Automation Excellent Bond Strength	
Disadvantages	Cannot Automate Have to Fixture		Cannot Use Soft Substrate Requires Heat & Pressure Limited Range of Finish Metals		Not Widely Accepted	

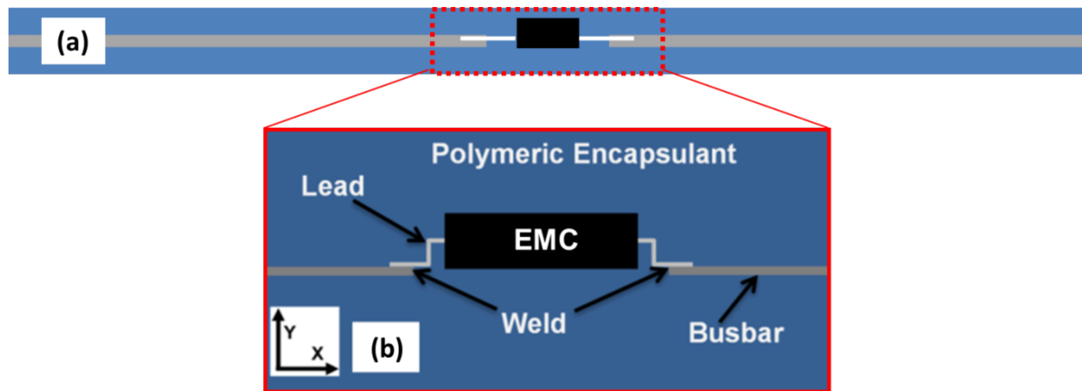

Figure 4. Assembly schematic (a) Global Schematic (b) Gull wing leads local schematic

Figure 4 contains a global and local profile schematic of the assembly used in this parametric study. Figure 4a exhibits the horizontally extended busbars connected in series with the beam lead component. The full assembly resembles a laminate style structure. Figure 4b provides a localized view of the component-busbar interconnect region. In this case the component leads are formed into a gull wing shape with radii of curvature of approximately 0.7mm and standoff height of approximately 1.35mm. The flat busbars are welded to the foot of the gull wing leads on either end of the component. The purpose of this particular lead design is to allow the compliant leads to absorb stresses generated during thermal cycling. Compliant gull wing leads are widely used in industry to allow for stress relief under variety of conditions such as mechanical and thermal cycling. Lead and interconnect stiffness often play a critical role in the reliability of the joint and of the surface mount components under cyclic loading. Ideally, this stress relief will prevents stresses from being transferred to critical areas of the assembly such as those adjacent to the package and weld regions.

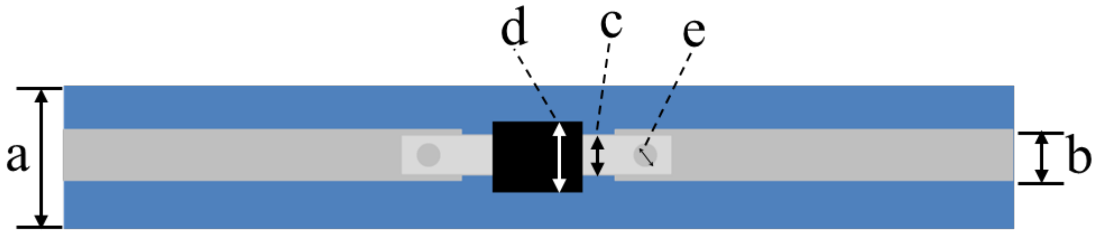

Figure 5. Top view schematic

Figure 5 is a schematic showing a top view schematic of the assembly, with Table 2 identifying all critical out-of-plane measurements. In this case the out-of-plane thickness values of the component are taken to be those of the COTS Super Barrier Rectifier (SBR) diode provided in technical drawing in the Appendix A. The out-of-plane thickness of the busbar is selected with several considerations in mind. Often, design requirements and/or several other requirements can constrain the design of an assembly and its respective components. The first consideration for the busbar thickness is the out-of-plane thickness of the component leads. The busbar thickness should be greater than or equal to that of the component lead in order to allow for sufficient area to create a robust interconnect (whether it is a solder joint, thermocompression bond, or welded joint). The design of the full assembly should also be considered. In this case the busbar should be sufficiently large enough with respect to the component leads, without being too large with respect to the rest of the assembly. A thickness that is too large for instance, may potentially interfere with other features of the assembly such as the encapsulant. Finally, the manufacturability must also be considered. The manufacturer's capabilities should be taken into consideration as far as the busbar's thickness itself, as well how the busbar can be integrated into the full assembly. This busbar thickness is well within the range of typical manufacturing capabilities. Similarly, the out-of-plane thickness of the

encapsulant requires similar considerations. The dimensions of the busbar and encapsulant thicknesses in this case are based on values in literature [21] taken from a instance where a similar laminate style assembly is used. Therefore it is reasonable to assume that the dimensions selected in this case are appropriate for such a design.

Table 2. Out-of-plane measurements of encapsulant assembly for Figure 5

	a	**b**	**c**	**d**	**e**
Feature	Encapsulant	Busbar	Diode Lead	Diode EMC	Weld
Length	11.0mm	5.3mm	4.4mm	5.8mm	2.42mm

2.3 Finite Element Modeling

This section reviews the FE model including the configuration, geometry, meshing material properties, and boundary conditions.

2.3.1 Thermal FEA Model – Configuration and Geometry

To perform this static FEA analysis, a two-dimensional finite element model is constructed to represent the assembly of interest. 4-Node bilinear quadrilateral generalized plane strain elements with reduced integration and hour glass control are utilized throughout the whole model. This generalized plane strain formulation allows for a finite amount of plane strain in the out-of-plane z-direction, which most closely mimics a three-dimensional finite element representation for the given model and environment. Quad-dominant structured meshing is utilized wherever possible, while free meshing is used for complex geometric features and transitions. Biased mesh seeding is applied from the model edges moving towards the component area, providing the finest mesh density in the component region.

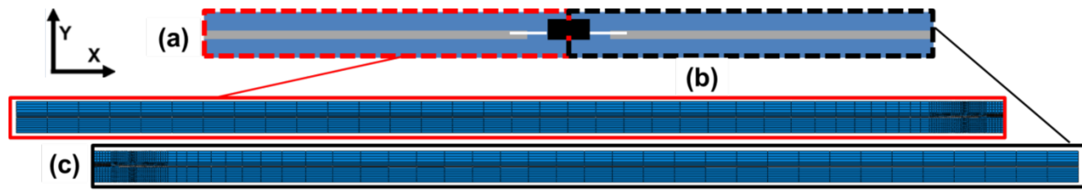

Figure 6. (a) Schematic of thermal FEA model (b) Left half of thermal 2D FEA model (c) Right half of thermal 2D FEA model

As previously mentioned, the model consists of long slender copper busbars, which are spot welded to the component's anode and cathode beam leads. A simplified schematic is shown in Figure 6a. Left and right halves of the FEA model shown in Figure 6b and Figure 6c (it is displayed as two images in order to distinguish see some of the macro level mesh features), depicting the biased seeding that allows for the mesh to increase in density as it approaches the weld region. The component is located in the center of the model. This is seen on the right half of Figure 6b and the left half of Figure 6c. Finer meshing is used in this region, as it is the primary failure area of interest. A detailed view of the mesh in the diode region is shown in Figure 7. Regions of curvature and unusual geometry often require non-trivial sectioning and free meshing. This is done in order to reduce approximation errors that arise from poor interior angles in distorted isoparametric elements. Additionally, transitioning between areas of different mesh densities often requires the use of non-structured meshing techniques. Examples of this can be seen around the lead and weld areas of Figure 7**.**

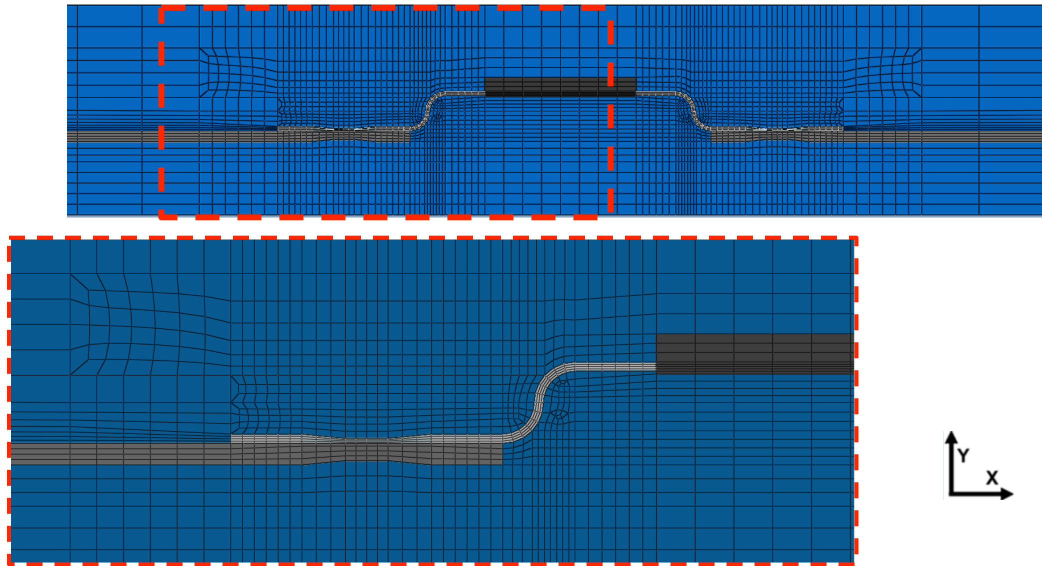

Figure 7. Two localized views of the component, interconnect, and busbar meshes

Figure 8 provides an expanded view of the spot welded region between the diode beam lead and busbar. The vertical height is locally reduced by 0.8mm in both the lead and busbar to represent the symmetric dimple created from the spot welding process. The weld region itself is given a smaller out-of-plane thickness for both the lead and busbar halves. This is because the weld is the only region where the lead and busbar are connected, and the weld itself does not span the full thickness of either the component lead or busbar. This can be seen clearly by looking at feature 'e' of Figure 5. The weld is assumed to be circular, and the out of plane thickness is assigned to be the diameter of the weld.

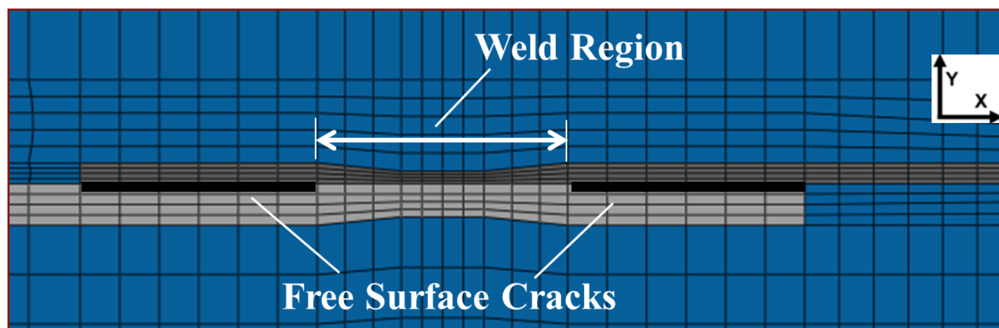

Figure 8. Spot weld region in the finite element model

Additionally, the overlapping interfaces adjacent to either side of each weld are unconnected. This is modeled using an interfacial 'crack' feature available in the FEA software. Seams are assigned to the nodes indicated with the black lines in Figure 8. This creates a duplicate set of nodes at those locations that can be allowed to separate upon loading or deformation. This also allows the ability to create interaction properties for these contact surfaces. The seams are assigned a frictionless contact property in the tangential direction and the default "hard" contact properties in the normal direction, in order to minimize the amount of overclosure during compressive loading.

2.3.2 Material Properties

The copper busbar, weld region, and leads are modeled with elastic-plastic properties in this static finite element analysis. Material properties are guided by values obtained from the literature. The encapsulant is modeled with rate-independent properties. Therefore, no viscoelastic or creep properties are incorporated into the model. This also means that some cyclic loading characteristics such as dwell times and ramp rates are assumed to have minimal effects on the results. This allows for the thermal loading profile to be simplified in such a way to significantly reduce the computation time required to populate and post-process the parametric test matrix.

The copper lead and busbar are modeled as elastic-plastic materials with kinematic hardening, using bilinear stress-strain curves (Figure 9). Kinematic hardening is used for the copper in preference to isotropic hardening, to prevent the yield strength from

becoming too large too quickly during thermal loading. This could lead to a quick elastic shakedown without a hysteresis loop. Examples of modeling copper with kinematic hardening under cyclic loading have been seen in literature [47]. The local hardening of the weld regions of the lead and busbar are modeled by adjusting the yield stress and plastic region of the stress-strain curve, as seen in Figure 9. There are examples in the literature [48-51] that show that the heat affected zone (HAZ) around welded area for metals has increased hardness and yield strength, when compared to the base metal. In some cases the HAZ is heat treated after the weld process to adjust the microstructure and mechanical properties in the HAZ. For this model, the weld region is assumed to have hardened resulting in higher yield stress. This yield strength is double for the weld region while the plastic modulus is kept the same. Experimental results of a similar laminate assembly showed no failures in the weld region itself. Rather, all failures occurred in the lead and busbar adjacent to the EMC and weld regions. These are therefore the primary areas of concern. Table 3 contains a list of material properties used as inputs to the thermo-mechanical FE models. As previously stated, material properties are obtained from literature. Some of the literature values used in this case are obtained from material characterization testing conducted by a third party lab. All polymeric materials, namely the encapsulants and diode epoxy molding compound (EMC) are modeled with temperature dependent properties. The driving forces for the mechanical stresses generated from the expansion mismatches, namely the CTE Young's modulus of the encapsulant are varied parametrically in this study. Temperature dependent linear elastic modulus and coefficient of thermal expansion values are used in all cases. The next section will

contain a detailed review of the encapsulant material properties, as this is the main subject of the parametric study.

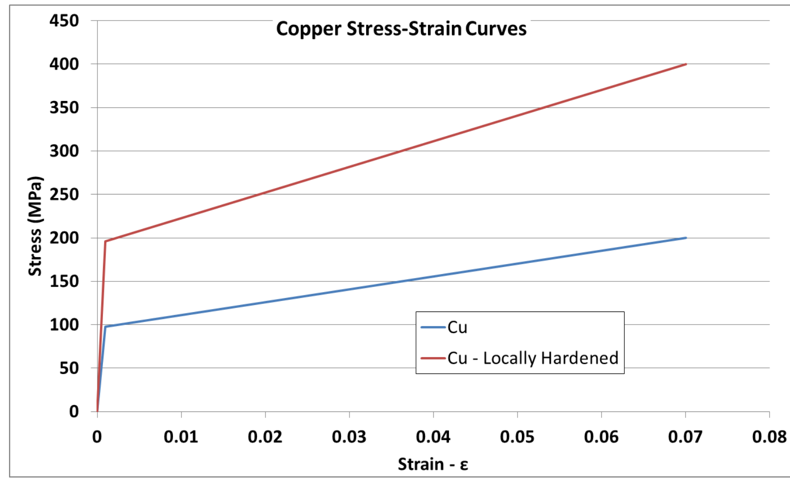

Figure 9. Regular and locally hardened copper stress-strain curves

Table 3. Material properties (Copper plastic properties are in Figure 9)

Section	Material	Temp. (°C)	Density (g/cm^3)	CTE - α (ppm/°C)	ν	E (GPa)	Material Modeling Type
Diode Lead	Copper	-	8.94	16.5	0.35	102.2	Elastic-Plastic
Locally Hardened Diode Lead	Copper	-	8.94	16.5	0.35	102.2	Elastic-Plastic
Busbar	Copper	-	8.94	16.5	0.35	102.2	Elastic-Plastic
Locally Hardened Busbar	Copper	-	8.94	16.5	0.35	102.2	Elastic-Plastic
Encapsulant	Varied	Varied	1.3	Varied	0.35	Varied	Temp. Dependent Elastic
Diode Package	EMC	25.0 75.0 175.0	1.9	5 10 50	0.35	20 1	Temp. Dependent Elastic-Plastic

Diode Package – EMC plastic properties						
Temp. (°C)	26		65		120	
Stress (MPa)	40	78	35	78	25	65
Plastic Strain	0	0.002	0	0.0025	0	0.004

2.3.3 Boundary Conditions

The model is constrained through a series of displacement boundary conditions (BCs). To eliminate rigid body motion, a pin constraint is applied to the bottom left node of each model, allowing for zero displacement in both the x-axis and y-axis, as seen in Figure 10.

Figure 10. Pin displacement BC constraint along on the bottom left corner of the model

Additionally, the entire bottom of the model is constrained to zero displacement along the y-axis (Figure 11). In other words, no warpage is allowed in the y-axis direction along the bottom of the model. This is displayed in two images, which represent the left and right half of the model (difficult to display as a single image). This represents this laminate structure being adhere to a stiff plate or fastened to a fixed structure.

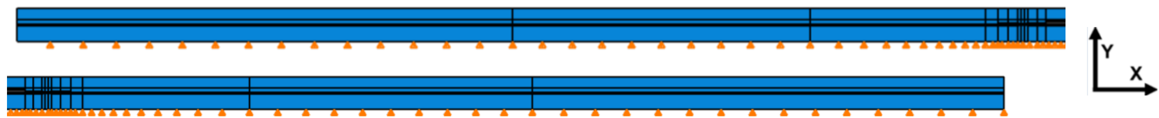

Figure 11. BC constraining the bottom of the model (top = left half, bottom = right half)

The left edge of the model is constrained to zero horizontal displacement along the x-axis (Figure 12). These boundary conditions prevent rigid body motion and attempt to represent the effects of having the assembly fastened to a stiff plate or surface.

Figure 12. Displacement BC constraining the right end of the model in the horizontal x-axis

The right edge is constrained to deform as a plane. To impose this BC a constraint equation is applied as a manually enforced boundary condition. This constraint equation requires that a linear combination of nodal variables sum to zero as displayed in Equation 2 and

Table 4:

$$A_1 u_i^P + A_2 u_j^Q + \cdots + A_N u_k^R = 0 \quad (2)$$

Table 4. Variables from Equation (2)

Variable	Meaning
u	Nodal Variable
P	Node #
i	DOF
A_N	Coefficient
N	# Nodes in Constraint Equation

Using this approach a set of nodes is constrained to move together, based on the movement of a single designated node. This coupling of a set of multiple degrees of freedom (DOFs) to a single DOF is done with a constraint equation in order to manually force the nodes of interest to take on identical values. In this study, Equation (2) is applied to the right edge of the finite element model as depicted in Figure 13a. The constraint allows the cross-sectional plane at the right edge to deform as a plane and remain orthogonal to the x-direction. Figure 13b depicts the table utilized in the commercial FEA software to define the constraint equation. As previously described, only two sets are defined: (i) a single reference node (ii) and a node set that is to be governed by said reference node. Therefore, only two coefficients need to be defined, that of the reference node and the node set.

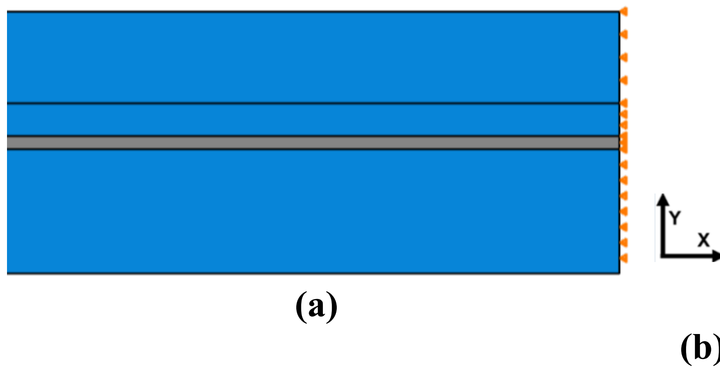

(a)

(b)

Name: Constraint-1

Type: Equation

Enter one row of data for each term in the equation

Click mouse button 3 for table options.

	Coefficient	Set Name	DOF	CSYS ID
1	-1	Cnst-SlaveNodes	1	(global)
2	1	Cnst-MasterNode	1	(global)

Figure 13. (a) Constraint equation BC on right edge of model (b) Constraint equation table

2.3.4 Mesh Refinement Study

A mesh refinement study is performed on the model for this study. Due to the number of runs that are typical in such parametric studies, it is critical to find a balance between model accuracy and computational resources. Figure 14 contains 3 different mesh densities used for this study: the top (Figure 14a) meshing scheme contains 1248 elements, the middle (Figure 14b) meshing scheme contains 4850 elements, and the bottom (Figure 14c) meshing scheme contains 19013 elements.

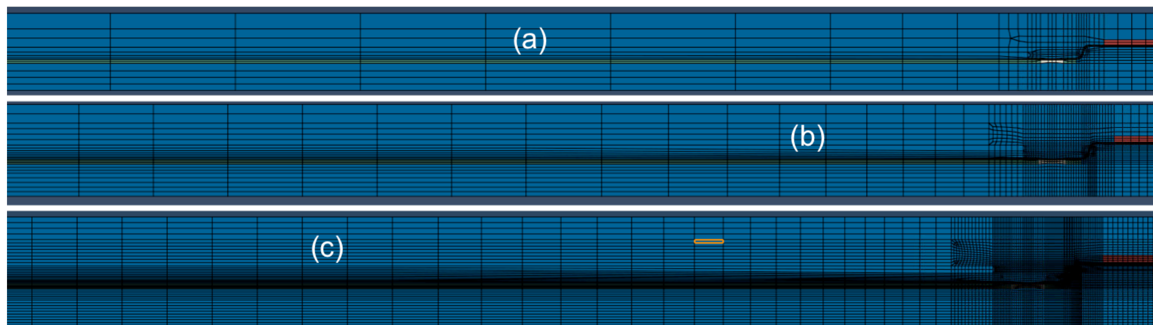

Figure 14. Mesh Refinement Study - meshing schemes

A 30°C thermal ramp cooling profile from 90°C to 60°C is used for this mesh convergence study. The whole model's potential energy is output and compared for all three meshing schemes. As the mesh density is increase that the potential energy of the model will converge asymptotically. Figure 15 contains a plot of the potential energy for all three meshing schemes overlaid on top of the thermal ramp cooling profile.

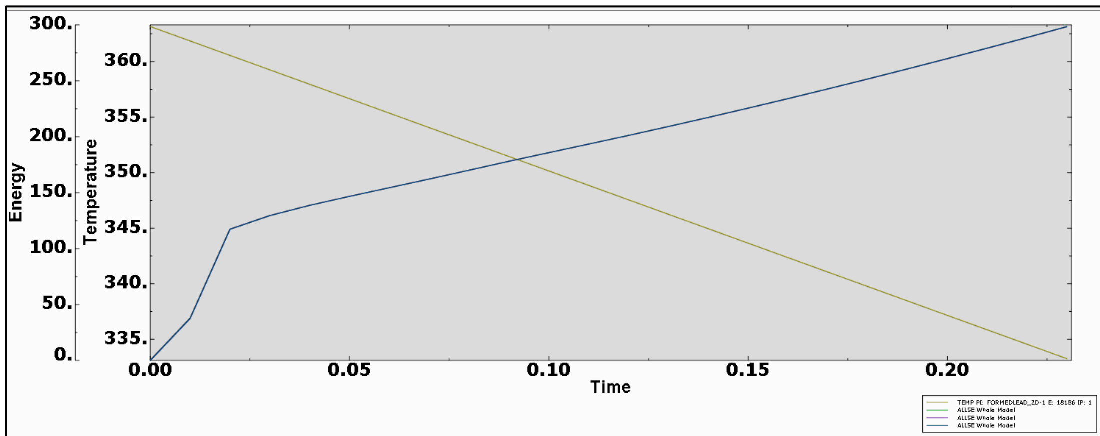

Figure 15. Potential energy plot and thermal cooling ramp profile from mesh refinement study

In this case all three models are showing almost the exact same potential energy history, and therefore the potential energy plot in Figure 15 looks like a single line. This indicates that the model has already converged. In this case the middle meshing scheme (Figure 14b) is selected as it provides a high enough mesh density to calculate stress and deformation values at the critical failure sites, while not being too computational demanding.

2.4 Parametric Study

In this section of the study, the material properties of the encapsulant are parametrically varied to examine the effect on the deformation and stress states at selected regions: the busbar, the formed beam lead component, and the interconnect

region. For an encapsulated design such as this one, a parametric approach is a cost-effective way to perform a sensitivity study and compare multiple material candidates.

2.4.1 Parametric Design Space

A two-dimensional parametric design space of material properties, consisting of the elastic modulus and coefficient of thermal expansion of the encapsulant, is constructed for this parametric study. The model is subjected to a ramp thermal loading profile for all cases in this design space. As explained in the previous section and in Table 3, the encapsulant is modeled as a (temperature-dependent) linear elastic material in each case. This simplifying assumption is made for several reasons. The first reason is that using a single encapsulant with linear elastic properties, rather than a composite laminate style structure, gives a better ability to study and understand the physics behind the problem statement. The second issue is that some of these polymers are known to have time dependent properties, in which case they need to be modeled as viscoelastic materials. Creep tests are often performed to obtain the material properties needed for model inputs or dynamic moduli tests are used to calculate prony series as model inputs. Unfortunately, the corresponding design space would consist of an intractably large and wide ranging number of material property sets. Such a study would require a prohibitive amount of resources to attempt such a large number of experiments and simulations on such a wide variety of material. Therefore, this study is limited to the effect of the (temperature-dependent) elastic properties of the encapsulant.

E (T) GPa							
	0.01 , 10	0.01, 32.5	0.01 , 55	0.01 , 77.5	0.1 , 100	0.01 , 125	0.01 , 150
	0.1 , 10	0.1, 32.5	0.1 , 55	0.1 , 77.5	0.1 , 100	0.1 , 125	0.1 , 150
	1, 10	1, 32.5	1, 55	1, 77.5	1, 100	1, 125	1, 150
	4.5, 10	4.5, 32.5	4.5, 55	4.5, 77.5	4.5, 100	4.5, 125	4.5, 150
	8 , 10	8 , 32.5	8, 55	8 , 77.5	8 , 100	8 , 125	8 , 150
E, CTE	CTE (T) °ppm/C						

Figure 16. Parametric design space – room temperature encapsulant material properties

The design space, as seen in Figure 16, consists of 35 sets of material properties (5 x 7 matrix). Each box in Figure 16 contains a combination of modulus and CTE values for the encapsulant. The elastic modulus is varied from 0.01Gpa (10MPa) to 8GPa in a manner that is almost logarithmic. The coefficient of thermal expansion is varied from 10ppm/C to 150ppm/C in increments of approximately 25ppm/C. The boundaries of the design space are selected based on typical materials used as encapsulants for electronic assemblies. As a result, some areas of this design space are not very realistic, meaning that few encapsulant materials exhibit such a combination of material properties. This is kept in mind during the analysis of the results.

The values listed in Figure 16 are actually only room temperature values. However, as previously mentioned, polymeric encapsulants are known to have fairly temperature dependent properties. In order to try and capture this temperature dependency, each combination in this matrix is set to represent its own subset of temperature dependent properties. In each case, the data set represents five temperature dependent modulus and CTE values, ranging from -50°C to 100°C. The

values vary a total of ±20% from the room temperature values. Table 5 illustrates an example of this for the data set E=1GPa, CTE=100ppm/C.

Table 5. Example of temp. dependent properties for room temp. E=1GPa, CTE=100ppm/C

Temp (C)	E(T) GPa	CTE(T) ppm/C
100.0	6.4	120
60.0	7.2	110
25.0	**1.0**	**100**
-10.0	8.8	90
-50.0	9.6	80

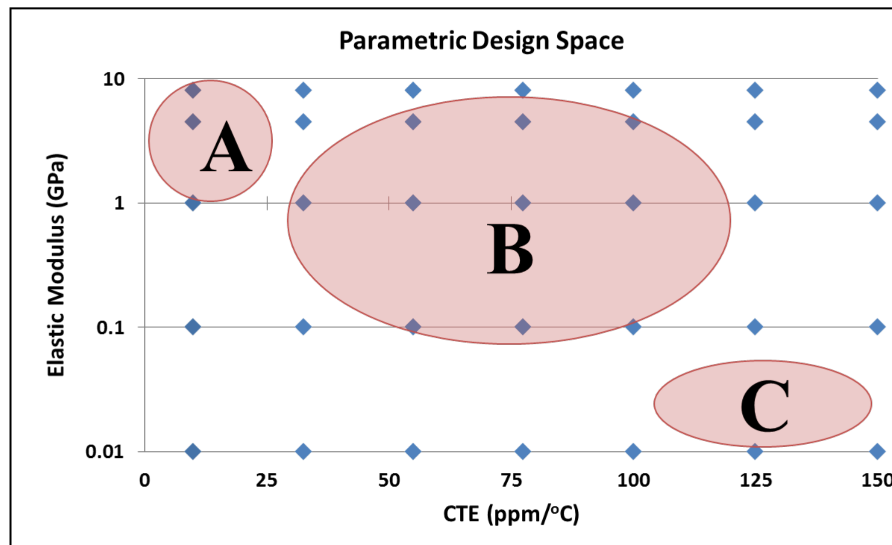

Figure 17. Parametric design space with regions of different encapsulant properties

Figure 17 illustrates the design space with three different general regions for these types of materials. Region A represents some of the stiffer thermosets such as epoxies, often with filler materials or stiffening additives. These materials tend to have low CTE values (1-15 ppm/C) and high modulus values (1-10GPa). Region B represents typical epoxies, polyimides, silicone-epoxies, select resins, among other materials. These materials tend to have both middle range moduli (0.5-4.5GPa) and CTE (30-110ppm/C) with respect to this design space. Region C represents typical elastomeric encapsulants such as silicones and polyurethanes. They tend have low

modulus values (0.1-10MPa) and high CTE values (100-150ppm/C). The design space was developed based on typical material properties found in literature [23-27] for encapsulation applications. The published mechanical properties of such encapsulants were reviewed to help establish these values and to determine the boundaries of the design space. Please refer to the [23-27] and Appendix B-1 through B-4 for a few sample tables of encapsulant material properties.

2.4.2 Loading Conditions

For this study a temperature ramp of 30°C is applied to each condition in the design space. An initial stress free temperature is taken to be at Tmax = 90°C, based on the cure process that would take place for a typical laminate or encapsulated assembly. All measured metrics of interest are measured over the length of the 34temperature ramp. This is a quasi-static analysis with rate independent material properties, therefore the results are not sensitive to dwell periods or to ramp rates. Hence, no dwells or ramp rates are specified. This allows for reasonable computation time to run all cases within the design space. It is important to note that this thermal loading is applied as a field condition. This assumes that there are no gradients in the model. Figure 18 shows the temperature ramp loading profile used in this study:

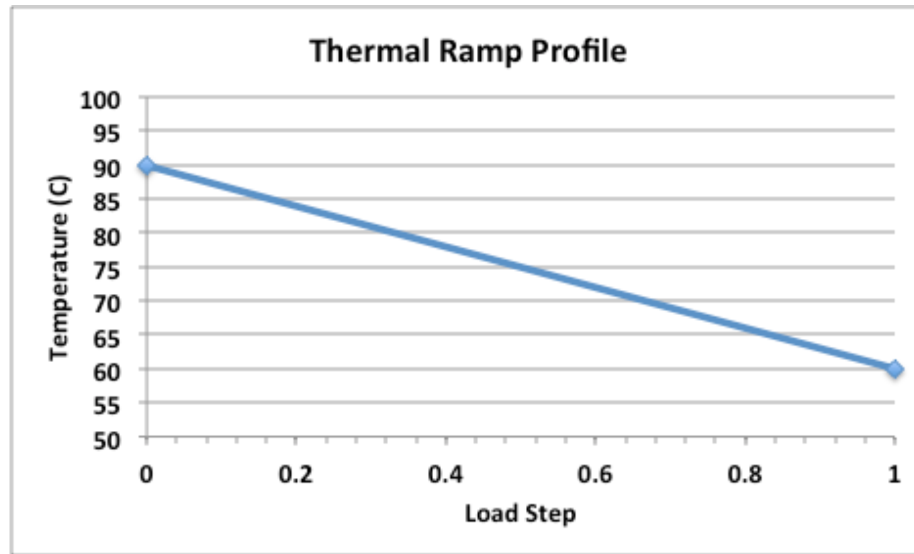

Figure 18. Thermal loading profile

2.5 Results and Discussion

This section provides a review and general discussion of the results of the design space parametric study. Two sets of metrics are measured to compare the effects of the different combinations of encapsulant properties over the entire design space. The first set consists of the axial forces and bending moments at multiple locations within the assembly. The second set of metrics used to compare the different combinations of encapsulant properties is a combination of elastic and plastic equivalent strain values. Response surface models are generated to visualize the responses and allow for the forces and strain values to be estimated for any combination of encapsulant properties.

Section 2.5.1 Axial Forces and Bending Moments

During thermal loading, the primary form of deformation in the assembly consists of extensional-compressional displacement along the horizontal x-axis. This is primarily due to the nature of the long and thin laminate assembly (i.e. large aspect ratio)

coupled with the boundary conditions applied. This generates compressive/tensile forces in the leads and busbar and shear/peel forces in the welds. Additionally, the gull wing formation in the component lead causes the component to be horizontally out of plane with the busbar. This introduces bending moments in the lead and busbar. The axial force and bending moments are calculated over the 30°C ramp loading profile. The axial force is calculated by integrating the axial stress in the x-axis along the cross section of the lead or busbar. The out of plane thickness of each material is assumed to be constant through the cross section. For this two-dimensional model, the stress in the out-of-plane direction is assumed to be constant. The out-of-plane thickness is therefore treated as a scalar and the integrated stress values are simply multiplied by the out-of-plane thickness. This is indicated in equation (2), where $P_{xx}(T)$ represents the axial force in the x-direction, and $\sigma_{xx}(T)$ represents the axial stress in the x-direction as a function of temperature, and *t* represents the out-of-plane sectional thickness of the material.

$$P_{xx} = P_{axial} = \int \sigma_{axial} dA = t \cdot \int \sigma_{xx}(T) \cdot dy \qquad (2)$$

Similarly, the shear and peel and forces are calculated by integrating the shear and vertical (y-axis) stresses across the length of the weld (equations 3-4), respectively, and multiplied by the out-of-plane thickness of the weld. The axial, shear, and peel forces are fairly straightforward to calculate during the Abaqus post-processing analysis.

$$P_{xy} = P_{shear} = \int \sigma_{shear} dA = t \cdot \int \sigma_{xy}(T) \cdot dx \qquad (3)$$

$$P_{yy} = P_{peel} = \int \sigma_{peel} dA = t \cdot \int \sigma_{yy}(T) \cdot dx \tag{4}$$

The bending moment (M_y) is calculated as an integration of the axial stress (in the x-direction) multiplied by the distance from neutral axis (y_{NA}) of the cross section of the lead or busbar. Represented by equation (5), the bending moment is integrated from ± h/2, which represents half the thickness of the cross section of interest. Again, the stresses in the out-of-plane (z-direction) are assumed to be uniformly distributed, therefore the integrated values are simply multiplied by the out-of-plane thickness. This calculation is more non-trivial to perform during the Abaqus post-processing analysis. The stress distribution through the cross section of either the lead or busbar is exported to Matlab, and a numerical integration is performed using a simple rectangle method to approximate the bending moment (see Appendix for Matlab source code).

$$M_y = t \cdot \int_{-\frac{h}{2}}^{\frac{h}{2}} \sigma_{axial} y_{NA} dA = t \cdot \int_{-\frac{h}{2}}^{\frac{h}{2}} \sigma_{xx}(T) \cdot y_{NA} \cdot dy \tag{5}$$

Multiple locations are considered including: (i) the component lead adjacent to the EMC package, (ii) the component lead adjacent to the weld region, (iii) the weld region, (iv) and the busbar adjacent to the weld region. Figure 19 indicates the locations of these calculations. The axial force and bending moments are calculated for locations (i), (ii), and (iv), while the shear and peel forces are calculated for location (iii).

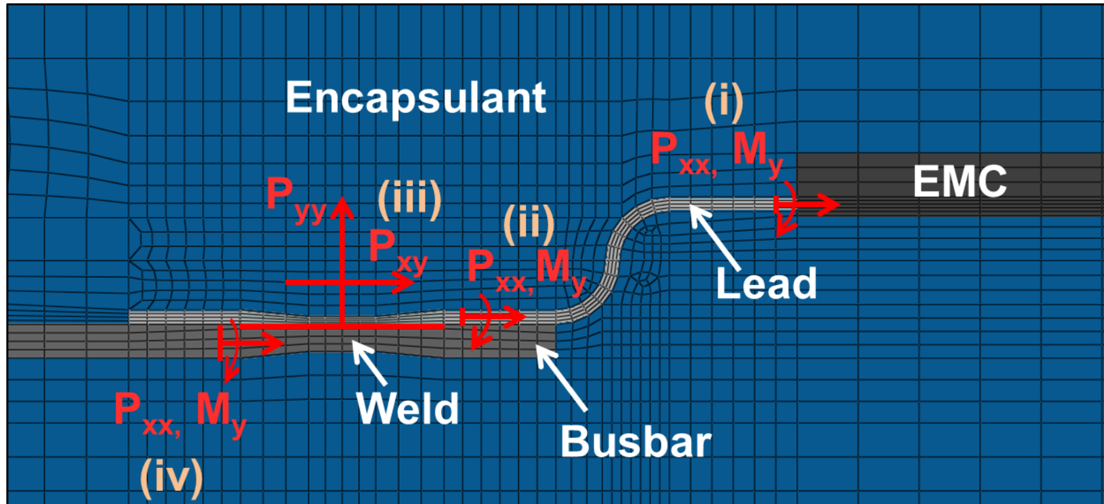

Figure 19. Local view showing the locations of force & bending moment measurements - (i) Lead adjacent to EMC (ii) Lead adjacent to weld (iii) Weld region (iv) Busbar adjacent to weld

Table 6 through Table 10 contain the axial force values calculated in each location across the design space. Response surfaces are generated in Matlab from these values at each location indicated in Figure 19. Each response surface is fitted with a piecewise cubic spline interpolant. The response surfaces allow for a useful visualization and comparison of the load values over the design space and between locations. Additionally, the response surface models can be evaluated at any location and used to estimate the force and bending moments as a function of encapsulant properties. Figure 20 through Figure 24 contain the response surfaces and corresponding contours of the axial force, peel force, and shear force values output from each location. For the axial force response surfaces, there is an initial rise in force after passing approximately either a modulus of 1GPa or a CTE of 32.5 ppm/C. For the modulus, this is may be due to the fact that the modulus of 1GPa is a considerably large jump (order of magnitude) from the previous value in the design space. For the CTE, this may be due to the fact that value of 32.5ppm/C is the first

value in the design space that crosses above the CTE of the copper busbar and lead (~16ppm/C).

A possible explanation of this phenomenon is that after a certain threshold stiffness and CTE value are reached, part of the axial load shifts to a bending moment. The nature of the gull wing stress relief is such that the diode component is out-of-plane with respect to the busbar and the center of the encapsulant. This can cause bending in the lead adjacent to the EMC package. Appendices D-1 through D-3 contain bending moment response surfaces of the lead adjacent to the EMC, the lead adjacent to the weld, and the busbar adjacent to the weld. The response surfaces show that, as expected, the lead adjacent to the EMC has higher bending moments than the lead adjacent to the weld.

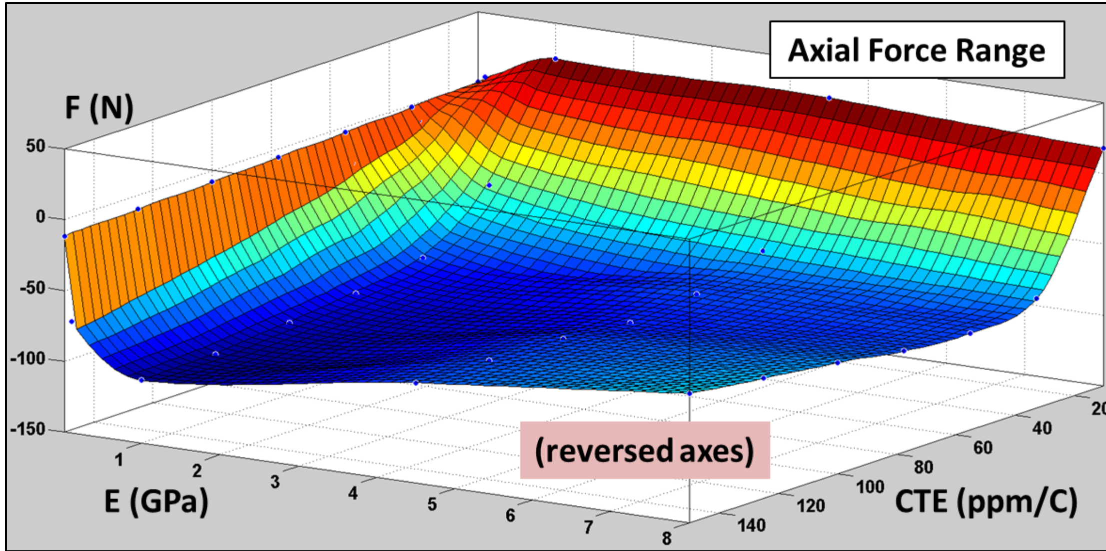

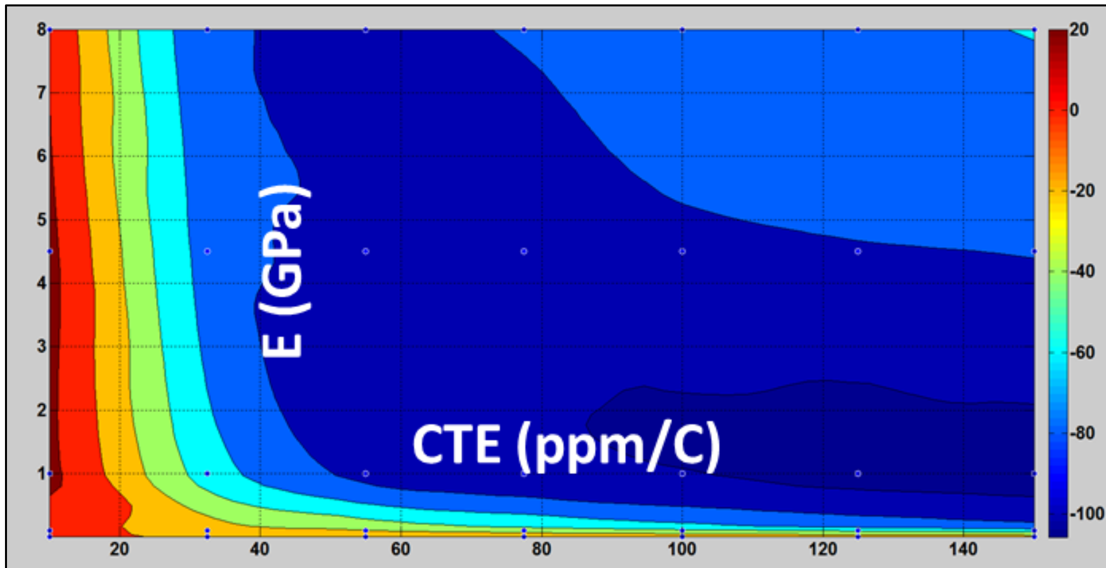

Figure 20. Response surface (top) and contour (bottom) for the axial force values calculated at the component lead adjacent to the EMC package

Table 6. P_{11} of the lead adjacent to the EMC as a function of encapsulant properties

Lead Adjacent to EMC Package		**CTE** (ppm/C)						
		10	**32.5**	**55**	**77.5**	**100**	**125**	**150**
E (GPa)	**0.01**	0.7	-1.5	-3.7	-5.8	-7.8	-9.7	-11.7
	0.1	5.3	-10.4	-24.5	-36.7	-48.4	-59.3	-71.0
	1.0	25.2	-48.6	-84.7	-94.0	-99.4	-104.4	-105.7
	4.5	25.3	-67.1	-82.4	-86.8	-82.8	-80.9	-79.3
	8.0	17.6	-72.7	-81.8	-79.0	-71.6	-65.5	-59.0

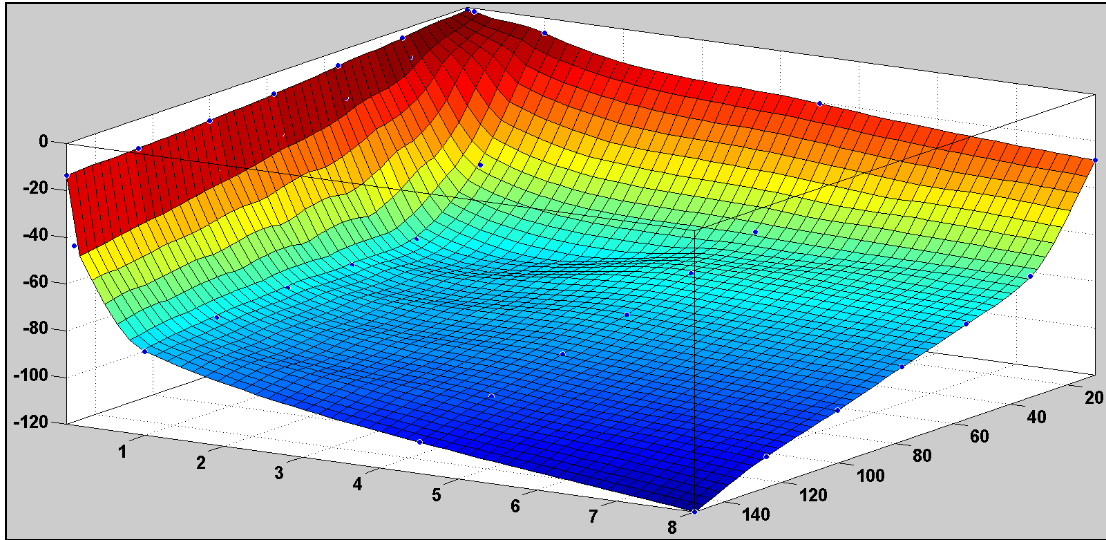

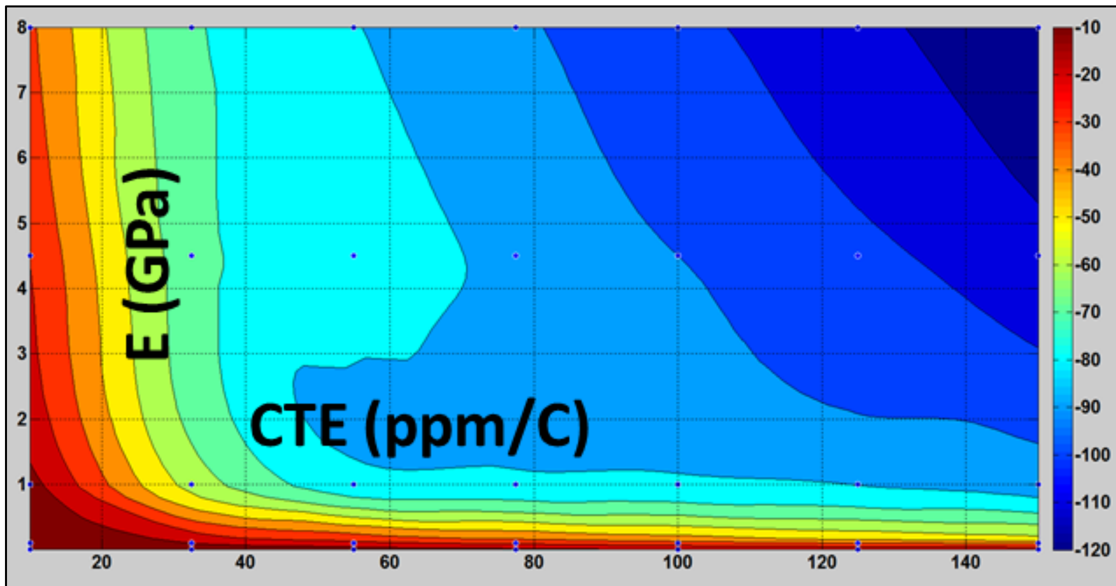

Figure 21. Response surface (top) and contour (bottom) for the axial force values calculated at the component lead adjacent to the weld region

Table 7. P_{11} of the lead adjacent to the weld as a function of encapsulant properties

Lead Adjacent to Weld Region		**CTE** (ppm/C)						
		10	**32.5**	**55**	**77.5**	**100**	**125**	**150**
E (GPa)	**0.01**	-1.2	-3.7	-6.3	-8.9	-10.9	-12.3	-13.5
	0.1	-1.4	-11.6	-19.6	-25.7	-31.6	-37.1	-43.1
	1.0	-6.6	-53.6	-76.0	-77.6	-78.0	-80.2	-84.2
	4.5	-20.4	-65.9	-74.1	-82.5	-90.0	-97.5	-106.7
	8.0	-28.2	-68.5	-79.5	-88.5	-97.6	-106.9	-120.0

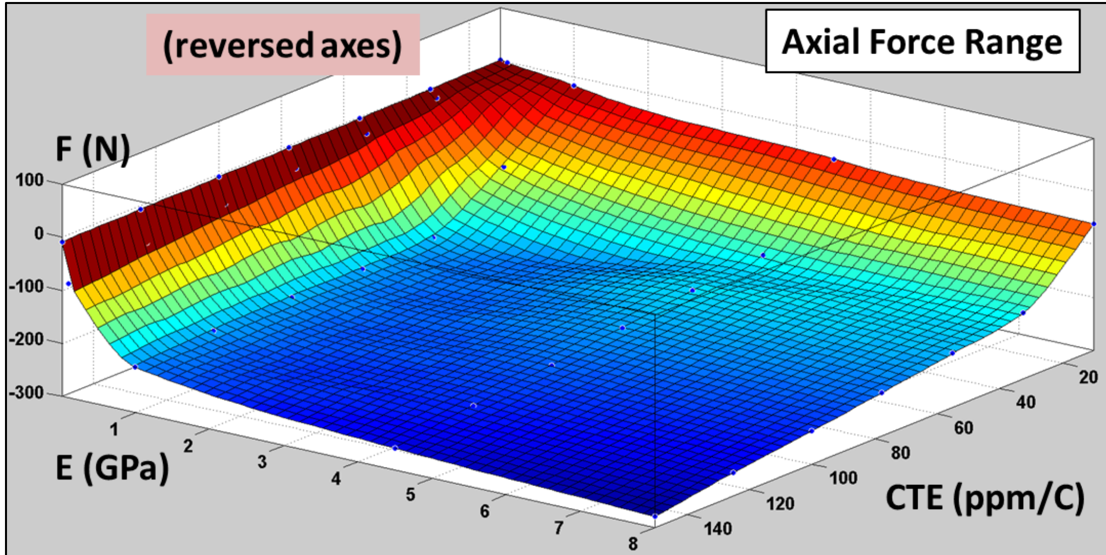

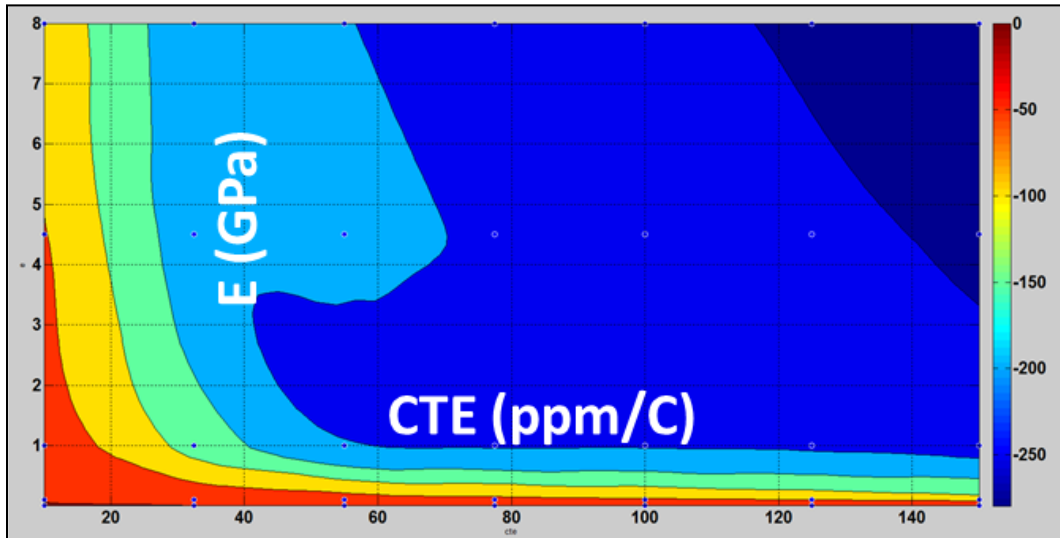

Figure 22. Response surface (top) and contour (bottom) for the axial force values calculated at the busbar adjacent to the weld region

Table 8. P_{11} of the busbar adjacent to the weld as a function of encapsulant properties

Busbar Adjacent to Weld Region		CTE (ppm/C)						
		10	**32.5**	**55**	**77.5**	**100**	**125**	**150**
E (GPa)	**0.01**	1.3	-0.3	-1.9	-3.5	-5.1	-6.7	-8.6
	0.1	-0.7	-14.3	-27.5	-40.1	-52.7	-66.7	-84.3
	1.0	-16.9	-116.4	-196.1	-202.3	-201.9	-205.8	-214.2
	4.5	-47.0	-174.5	-188.1	-205.2	-222.2	-238.9	-259.0
	8.0	-61.9	-175.5	-198.5	-218.6	-237.9	-256.8	-279.7

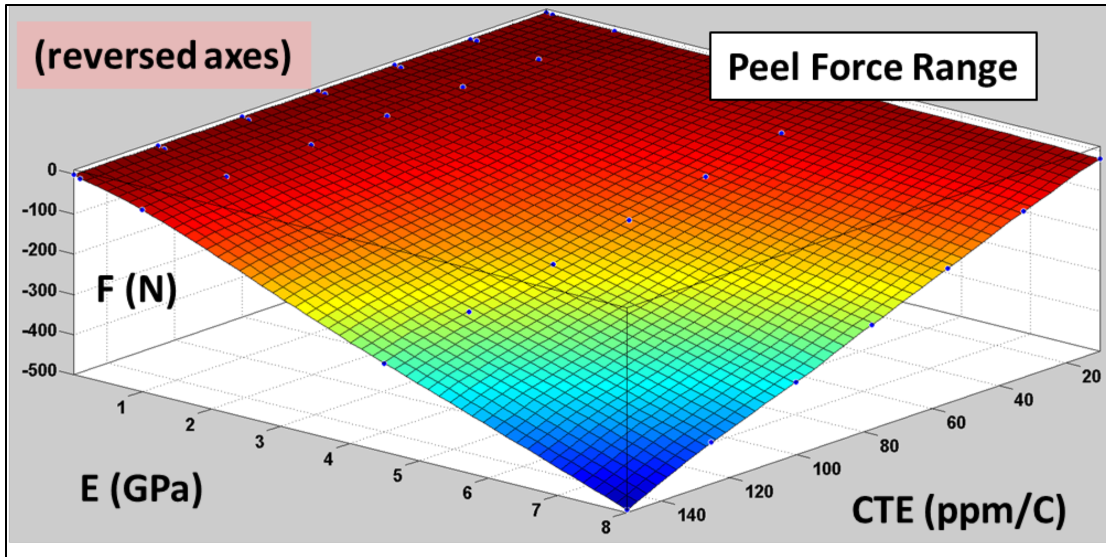

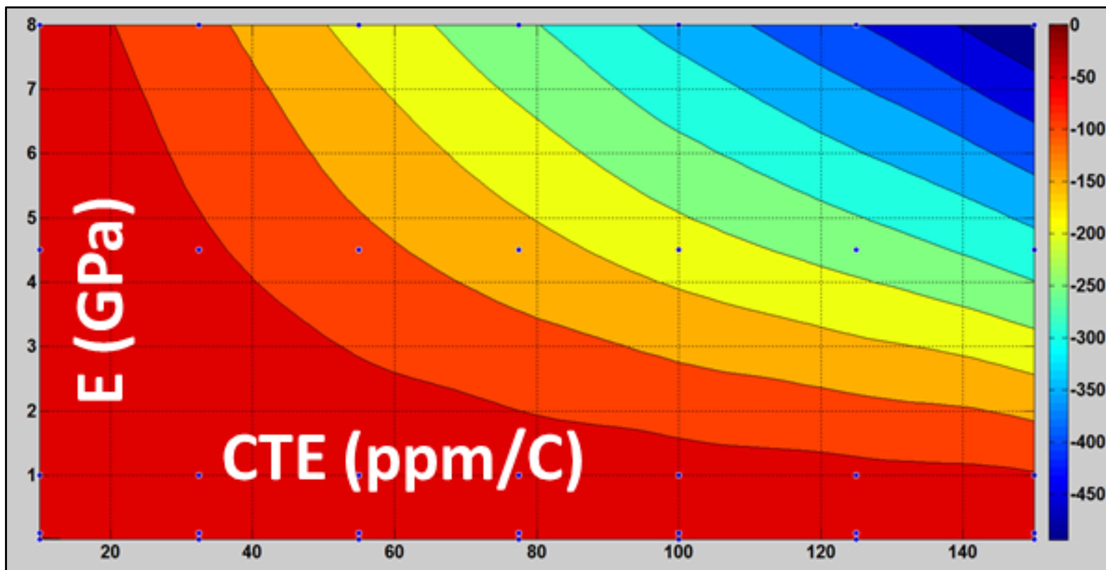

Figure 23. Response surface (top) and contour (bottom) for the peel force values calculated at the weld region

Table 9. P_{22} values at the weld as a function of encapsulant properties

Weld Region		CTE (ppm/C)						
		10	**32.5**	**55**	**77.5**	**100**	**125**	**150**
E (GPa)	**0.01**	0.2	-1.2	-1.2	-1.2	-1.4	-1.4	-1.6
	0.1	-1.2	-2.2	-3.2	-4.2	-5.6	-6.4	-7.4
	1.0	-3.8	-9.4	-13.8	-21.0	-28.0	-36.0	-46.8
	4.5	-12.8	-43.2	-87.0	-130.8	-176.2	-222.4	-279.6
	8.0	-21.2	-86.6	-164.6	-240.6	-318.8	-398.0	-493.8

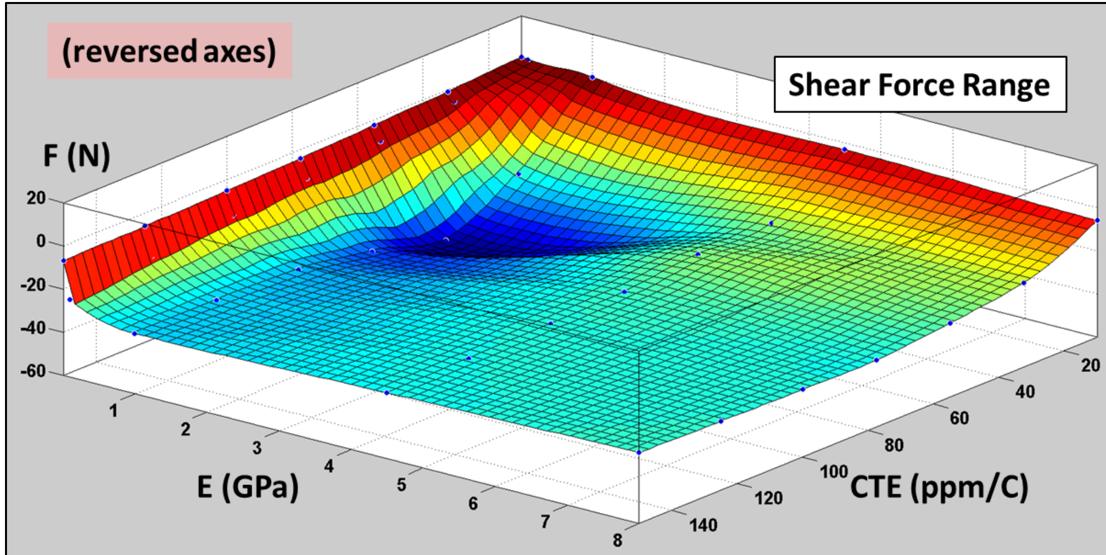

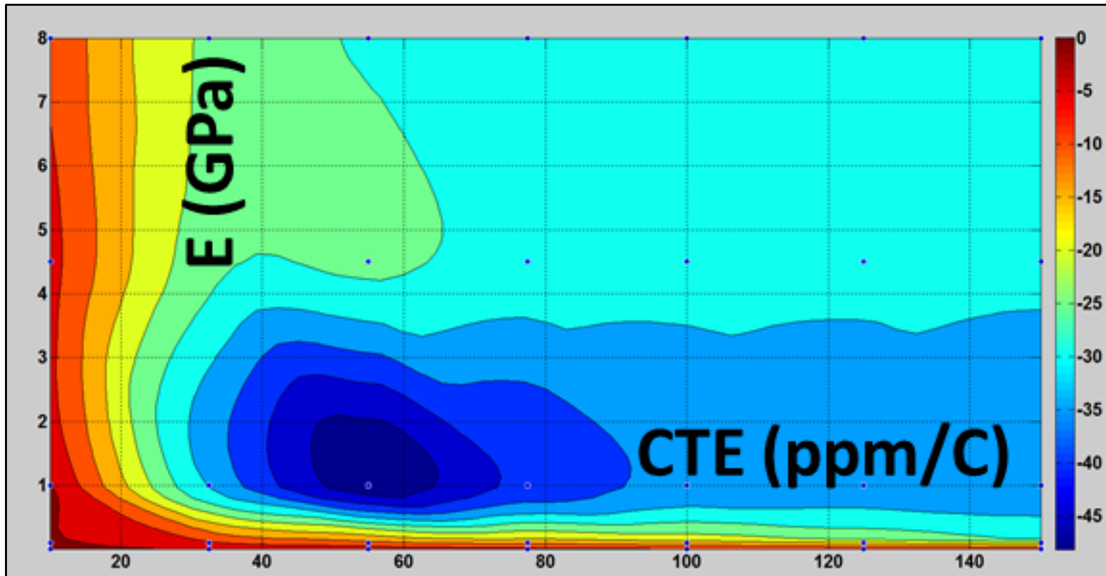

Figure 24. Response surface (top) and contour (bottom) for the shear force values calculated at the weld region

Table 10. P_{12} values at the weld as a function of encapsulant properties

Weld Region		CTE (ppm/C)						
		10	**32.5**	**55**	**77.5**	**100**	**125**	**150**
E (GPa)	**0.01**	1.3	-0.9	-2.5	-4.1	-5.3	-6.2	-6.9
	0.1	0.8	-4.9	-9.2	-12.5	-15.6	-19.3	-24.2
	1.0	0.4	-30.5	-47.6	-38.7	-33.3	-32.2	-32.0
	4.5	-3.2	-23.4	-23.9	-27.4	-28.3	-28.9	-29.4
	8.0	-5.9	-20.8	-25.7	-28.9	-28.6	-27.9	-27.0

Figure 20 contains the response surface and contour for the axial force values measured in the lead adjacent to the EMC package. For this design the maximum axial loading occurs for higher CTE levels at a modulus of approximately 1GPa. Furthermore, after peaking at about -80N to -105N, the axial force continues to decrease as the modulus and CTE are increased. This is somewhat counterintuitive as continuing to increase the stiffness and CTE of the encapsulant should increase the thermomechanically generated stresses caused during thermal expansion. However this is a complex heterogeneous assembly therefore the deformation fields are non-trivial. One explanation for this could be a change in the deformation direction of the section of the encapsulant adjacent to the EMC. This is related to expansion differences between the encapsulant and copper lead/busbar adjacent to the EMC. The outer edge of the encapsulant, which is furthert away from the lead and busbar, wants to deform further than the internal section of the encapsulant which is closer to the lower expanding copper material. The middle image in Figure 25 shows the expected deformed geometry of the encapsulant. As previously stated, the outer edge of the encapsulant is expected to deform more in the u_1 direction, as it is further away from the copper lead and busbar. However, if this deformation field was to change or reverse as a result of increasing the modulus and CTE, this change in displacement direction of the encapsulant could help reduce some of the axial forces in the lead adjacent to the EMC. This could offer some explanation to the non-monotonic trend observed in Figure 20.

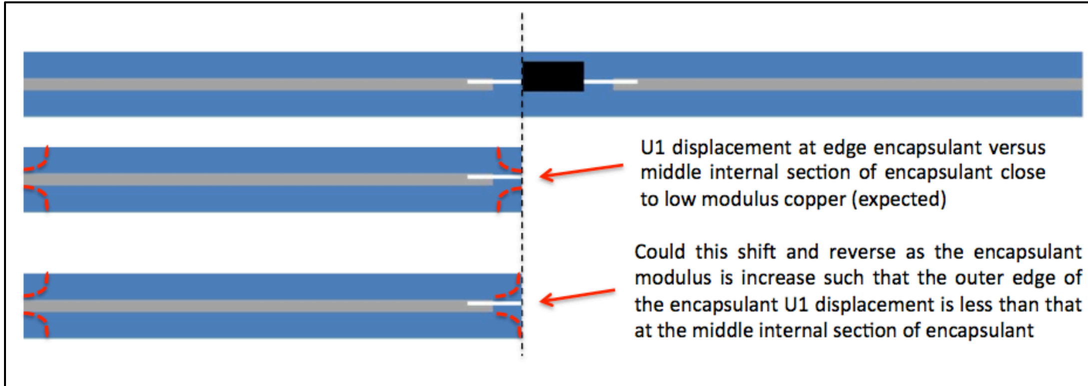

Figure 25. Schematic of deformed geometry of the encapsulant through the cross section adjacent to the EMC region

To study this, the u_1 displacements are output at node on the edge of the encapsulant and the internal part of the encapsulant adjacent to the lead (Figure 26) for each modulus. This process is repeated for two CTE values, one below (10ppm/C) and one above (77.5 ppm/C) the CTE of the copper.

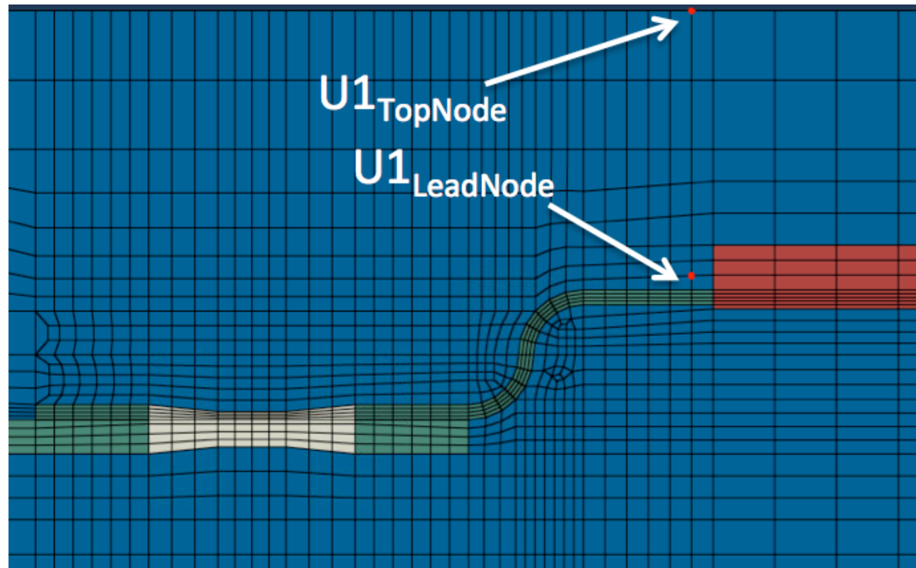

Figure 26. u_1 node locations

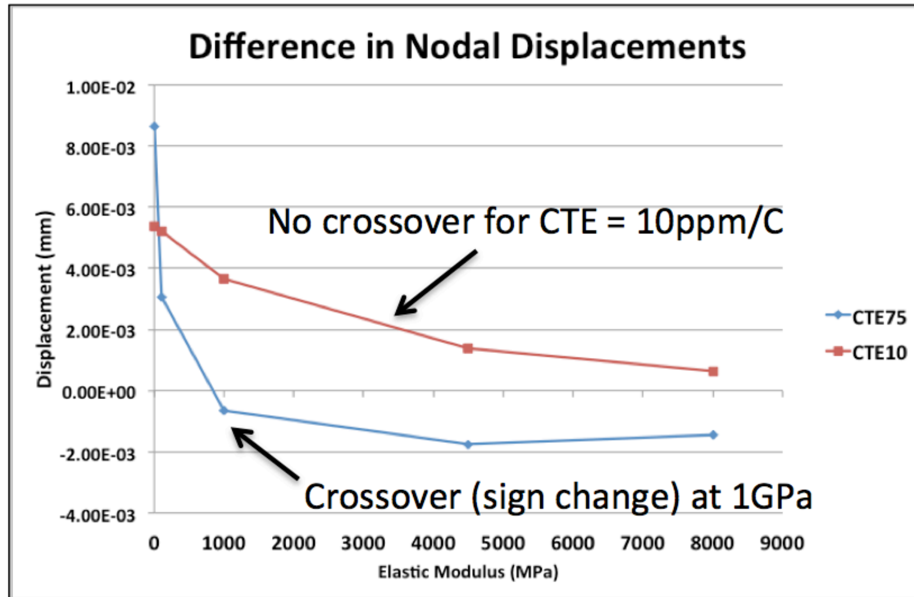

Figure 27. Difference in encapsulant edge and center u_1 nodal displacement

The difference in the two nodal u_1 displacement values are plotted as a function of modulus for both CTE values in Figure 27. For this calculation, u_1 of the edge node is subtracted from u_1 of the internal node adjacent to the lead ($u_{EdgeNode}$ -$u_{LeadNode}$). For the CTE value below that of the copper, there is no sign change in this nodal displacement difference. This signifies that the edge node is always displacing more than the internal node adjacent to the copper lead as the modulus is increased. Looking at the response surface in Figure 20, there is no monotonic behavior observed along the CTE value of 10ppm/C as function of modulus. For the CTE value above that of copper, there is a sign change in the nodal displacement difference that occurs at 1GPa. This signifies that above a certain threshold value, the internal displacement node actually displaces more than the outer edge node. This change in the deformation field could be helping reduce the axial force in the lead in this region. Looking at the response surface in Figure 20 for a CTE value of 77.5ppm/^{o}C, a non-monotonic trend begins to develop at this threshold value of 1GPa

s the axial force in the lead begins to decrease as the encapsulant modulus is increased.

Another interesting phenomenon observed is that the axial force varies across the various locations in the lead and busbar. Due to the extensional-compressional deformation of the assembly and the nature of axial load-train between the lead-interconnect-weld regions, the axial forces in these various locations would be expected to be fairly similar. The maximum axial force occurring in the lead adjacent to the EMC (Figure 20) is approximately -100N. The maximum axial force occurring in the lead adjacent to the weld region (Figure 21) is approximately -120N. The maximum axial force occurring in the lead adjacent to the weld region (Figure 22) is approximately -300N. Moreover these are just the absolute maximum values and do not all occur in the exact same locations within the design space. There is a considerable difference in the axial forces between the measured locations at each combination in the design space. One possible explanation for this phenomenon is that some of the load sharing is transferred to the encapsulant. Therefore a study was conducted to monitor the axial force through the cross-section of the entire assembly. Figure 28 shows the four locations where values are monitored. The axial stress (S_{11}) is integrated through the cross section of the assembly, including the lead, busbar, and encapsulant regions. The calculated values are broken down into axial forces in the upper section of encapsulant, lead, busbar, and lower section of encapsulant. These section values are summed to estimate the total axial force through the cross section

for each location. This is repeated for three different temperature along a diagonal of the design space.

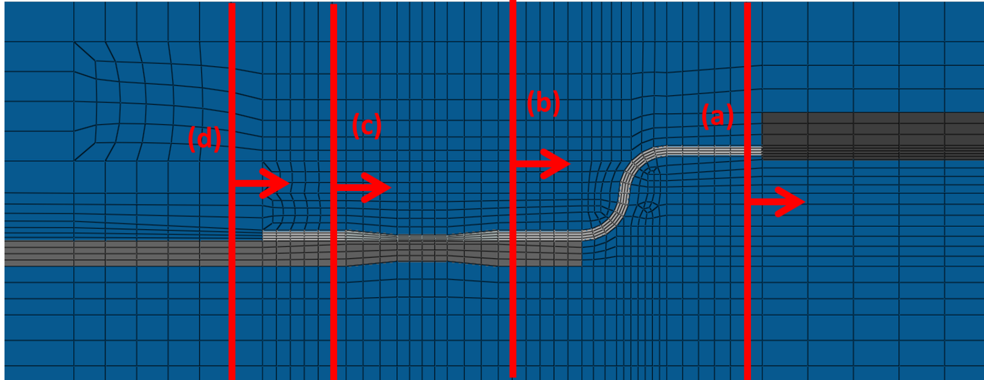

Figure 28. Measurement locations for the axial force comparisons through cross-section

Table 11 contains a comparison of these axial force values calculated through the cross section of the assembly, at multiple locations, for three combinations of encapsulant properties. The results in the table show that although the axial forces in the lead and busbar shift from location to location, the axial forces in the upper and lower portions of the encapsulant shift from location to location shift as well. The resulting net axial force through the assembly cross-section is relatively unchanged. This indicates that the encapsulant is likely absorbing some of the axial loading sharing through the load-train. The encapsulant shows the lowest amount of axial forces adjacent to the EMC package and shifts to higher values closer to the weld region. In almost all cases the encapsulant axial force is in the opposite direction of that measured in the lead and busbar.

Table 11. Axial force comparison values (N) through cross-section a various locations for multiple encapsulant property combinations

E=8.0GPa, CTE=10ppm/C				
Axial Forces (N)	(a)	(b)	(c)	(d)
Encapsulant Above Lead and Busbar	10.0	39.3	44.2	34.6
Lead	17.6	-28.2	-24.5	
Busbar		-44.4	-61.9	-75.8
Encapsulant Below Lead and Busbar	-24.7	33.2	42.0	41.1
TOTAL	3.0	0.0	-0.2	-0.1
E=4.5GPa, CTE=55ppm/C				
Axial Forces (N)	(a)	(b)	(c)	(d)
Encapsulant Above Lead and Busbar	24.2	85.1	109.4	86.4
Lead	-67.1	-65.9	-59.1	
Busbar		-135.5	-174.5	-204.4
Encapsulant Below Lead and Busbar	44.1	116.3	123.8	117.4
TOTAL	1.1	0.0	-0.4	-0.6
E=0.01GPa, CTE=150ppm/C				
Axial Forces (N)	(a)	(b)	(c)	(d)
Encapsulant Above Lead and Busbar	5.2	6.3	7.0	7.6
Lead	-11.7	-13.5	-3.2	
Busbar		2.8	-8.6	-12.3
Encapsulant Below Lead and Busbar	6.5	4.5	4.6	4.7
TOTAL	0.0	0.1	-0.2	0.0

Section 2.5.2 Elastic and Plastic Strain

Under realistic life conditions, the assembly experiences temperature cycling, leading to thermomechanical degradation. As mentioned in the introduction section, a strain based life model such as the one developed by Coffin-Manson [1] is typical for such assemblies. This life model is used for calculating cycles to failure, fatigue curves, and acceleration factors. Consequently, it is useful to compare the elastic and plastic strain values, at various locations in the assembly, over the entire design space. The

generalized Coffin-Manson equation is included again below with descriptions of each of the variables given in Table 12.

$$\frac{\Delta\varepsilon_{el}}{2} + \frac{\Delta\varepsilon_{pl}}{2} = \frac{(\sigma_f - \sigma_m)}{E}\left(2N_f\right)^b + \varepsilon'_f\left(2N_f\right)^c \qquad (1)$$

Table 12. Terms of generalized Coffin-Manson equation

Variable	Definition	Variable Type
$\Delta\varepsilon_{el}/2$	Elastic strain amplitude	Input
$\Delta\varepsilon_{pl}/2$	Plastic strain amplitude	Input
σ_f	Fatigue strength coefficient	Model constant (Material Property)
σ_m	Hydrostatic or mean stress (if non-zero)	Input
b	Fatigue strength exponent	Model constant (Material Property)
ε'_f	Fatigue ductility coefficient	Model constant (Material Property)
c	Fatigue ductility exponent	Model constant (Material Property)
N_f	Cycles to Failure	Output
E	Elastic Modulus	Material property

A custom metric consisting of the sum of the elastic and plastic equivalent strains is used for this comparison. The equivalent plastic strain is calculated in Abaqus using a metric called the plastic strain magnitude (PEMAG), which is calculated according to equation (6):

$$PEMAG = \sqrt{\frac{2}{3}\varepsilon^{pl} : \varepsilon^{pl}} = \sqrt{\frac{2}{3}\varepsilon_{ij}{}^{pl}\varepsilon_{ij}{}^{pl}} \qquad (6)$$

Here ε^{pl} represents the plastic strain. For monotonic loading, PEMAG is equal to the plastic equivalent strain (PEEQ). Since a thermal ramp loading profile is used for this design space study, PEMAG equates to PEEQ. The elastic equivalent strain is calculated as follows:

$$\varepsilon_{eq}{}^{pl} = \sigma_{vM} \frac{2(1+\nu)}{3E} = \frac{\sigma_{vM}}{3G} \tag{7}$$

$$\varepsilon_{eq}{}^{Total} = \varepsilon_{eq}{}^{el} + \varepsilon_{eq}{}^{pl} = \varepsilon_{eq}{}^{el} + PEMAG = \frac{\sigma_{vM}}{3G} + \sqrt{\frac{2}{3}\varepsilon^{pl} : \varepsilon^{pl}} \tag{8}$$

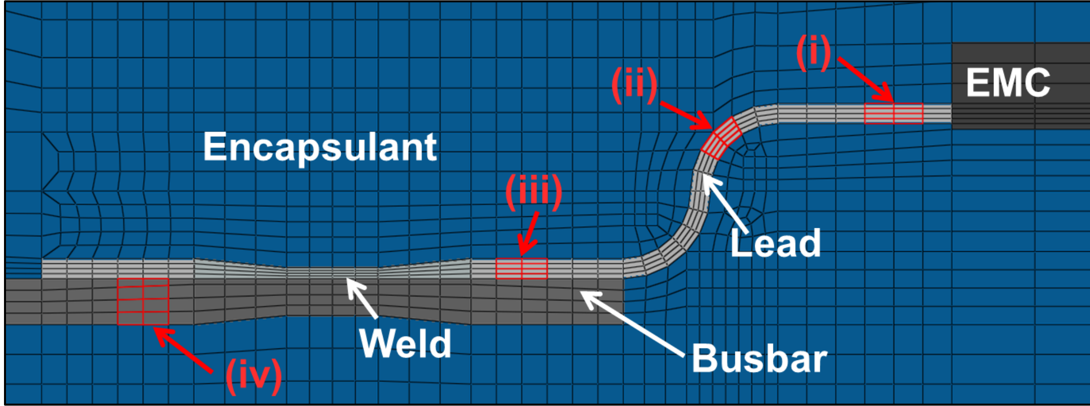

Figure 29. Local view of locations of equivalent total strain measurements - (i) Lead adjacent to EMC (ii) Lead bend (iii) Lead adjacent to weld region (iv) Busbar adjacent to weld region

The sum of these two values, seen in Equation 8, is used to generate response surfaces over the design space. Values are calculated at four locations within the model: (i) the lead adjacent to EMC; (ii) the lead bend; (iii) the lead adjacent to weld region; (iv) the busbar adjacent to weld region. These locations are selected based on failures seen in a similar laminate assembly. Furthermore, it is well established within the literature that the interconnect region and regions adjacent to the interconnect and EMC package are often the most vulnerable to fatigue failure. At each location, a

volume weighted averaging scheme is used over eight elements of approximately the same volume. This is indicated by the red areas in Figure 29.

Figure 30 through Figure 33 show the response surfaces and contour plots of ε_{eq}^{el} + ε_{eq}^{pl} for each location of interest, while Table 13 through Table 16 give the discrete volume-weighted average total equivalent strain values used to generate the response surfaces. The responses surfaces show similar general trends. For all four locations, the total equivalent strain values are relatively small (on the order of 10^{-4} to 10^{-3}) when either independent variable (stiffness or CTE) is fixed to be very small. It is also important to note that the smallest total equivalent strain values occur when the CTE values of the encapsulant are closest to that of the copper leads and busbar (~16ppm/^{o}C). Furthermore, when either the Young's modulus or the CTE are fixed to be small, regardless of how large the second independent variable is, the midpoints of the response surface models and contour plots are always larger. Put another way, the output tends to be higher when both independent variables are at their middle values, versus when once is small and one is large. This indicates a significant amount of interaction between the variables. Looking across the diagonal of the design space that passes through regions 'A', 'B', and 'C' of Figure 17. Region 'B' shows the highest total strain values while regions 'A' and 'C' are fairly low, indicating that middle range values of both the modulus and CTE produce higher strains than if either one of these parameters is very large. This indicates that there is a fair amount of interaction between the Young's modulus and CTE. Consequently the largest amount of total equivalent strain occurs, as expected, at the combination of the largest modulus and CTE values (in all cases).

Several interesting observations can be made when either the Modulus or the CTE is held constant. When the modulus is fixed, the total equivalent strain shows a fairly linear (or in some cases even slightly parabolic) trend as the CTE is increased. When the CTE is fixed, a large initial rise is seen in the total equivalent strain until the modulus crosses approximately the 1GPa value. This is followed by a slower and more gradual rise that eventually starts to follow asymptotic behavior. One reason this may occur is that after a certain threshold, the modulus may become so stiff that it completely supresses the compliant effects of the lead-interconnect region. Once this threshold is reach there is almost a saturating effect, where continuing to increase the modulus does not show a significant increase in the total equivalent strain.

It is also useful to compare the total equivalent strain values at the various locations within the assembly. The busbar adjacent to the weld region, region (iii) of Figure 29, shows the lowest strain values across all areas of the design space. Either the lead bend or the lead adjacent to the EMC package, regions (ii) and (iii) of Figure 29, show the largest total equivalent strain values depending on the location within the design space. However, for the majority of cases, the component lead adjacent to the EMC package has the largest values of total equivalent strain.

This type of response surface modeling can help identify and compare potential material design candidates. There are values within these response surfaces that are rather large (i.e. several % strain), indicating that certain combinations of material properties are too severe given the loading profile and may be unrealistic for such a design. The harshest areas of this design space are mostly outside of the three regions identified in Figure 17, suggesting that many of the harshest combinations of material

properties do not apply to the majority of encapsulants used for this type of application.

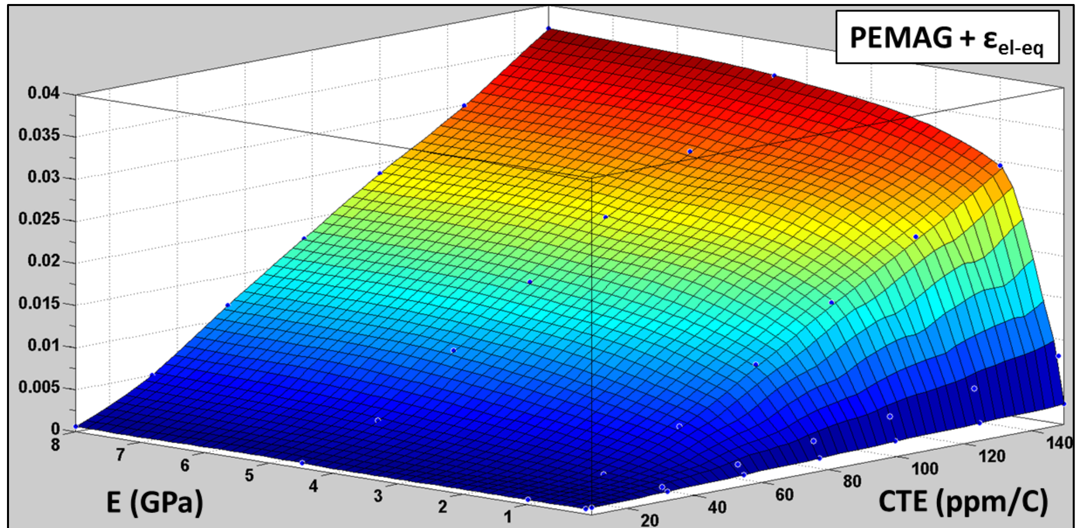

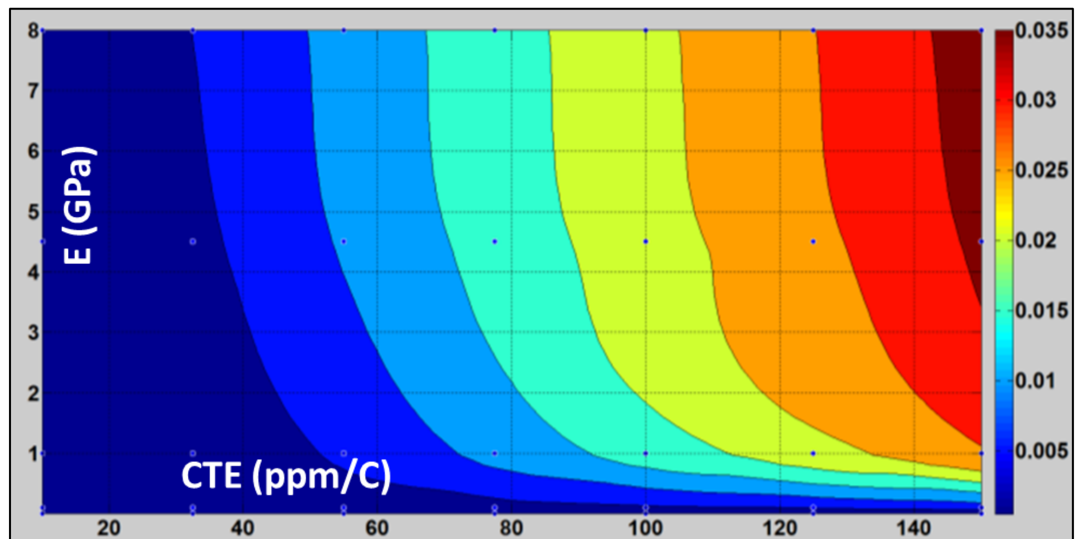

Figure 30. Response surface (top) and contour (bottom) for the average equivalent strain values calculated at the lead adjacent to the EMC package

Table 13. PEMAG + ε_{el-eq} for the lead adjacent to the EMC as a function of encapsulant properties

Lead at EMC Package		**CTE** (ppm/C)						
		10	**32.5**	**55**	**77.5**	**100**	**125**	**150**
E (GPa)	**0.01**	8.17E-04	1.04E-03	1.29E-03	1.54E-03	1.81E-03	2.08E-03	2.41E-03
	0.1	5.83E-04	1.43E-03	2.43E-03	3.49E-03	4.68E-03	6.05E-03	8.02E-03
	1.0	5.37E-04	1.87E-03	5.78E-03	1.14E-02	1.71E-02	2.30E-02	2.95E-02
	4.5	6.07E-04	3.92E-03	1.05E-02	1.69E-02	2.29E-02	2.88E-02	3.59E-02
	8.0	6.46E-04	5.04E-03	1.16E-02	1.78E-02	2.38E-02	2.99E-02	3.72E-02

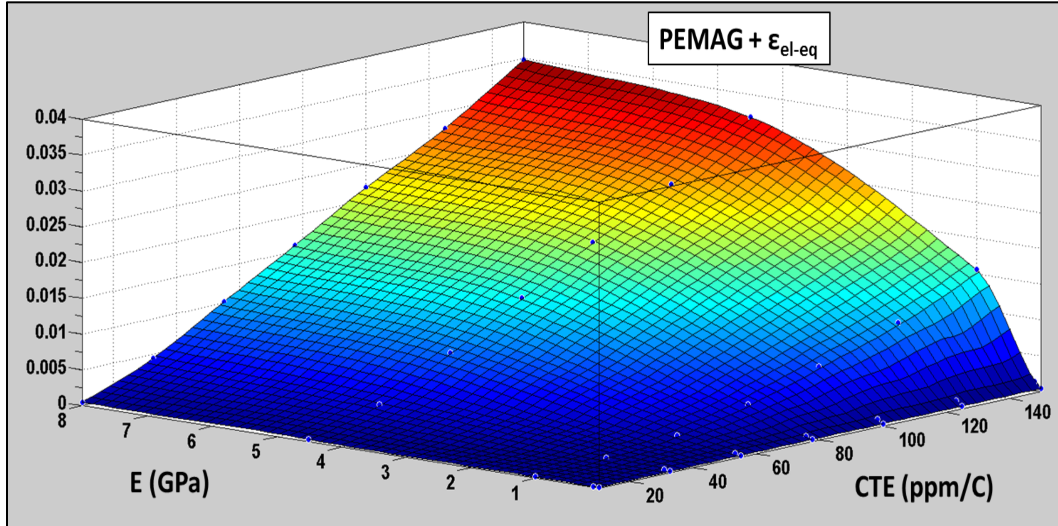

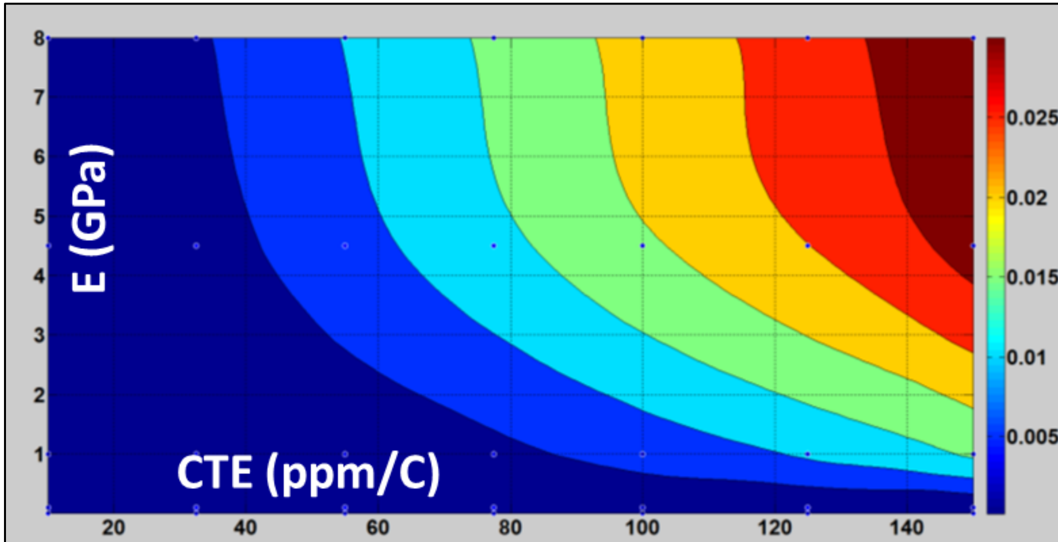

Figure 31. Response surface (top) and contour (bottom) for the average equivalent strain values calculated at the lead adjacent to the weld region

Table 14. PEMAG + $\varepsilon_{el\text{-}eq}$ for the lead adjacent to the weld as a function of encapsulant properties

Lead at Weld Region		CTE (ppm/C)						
		10	**32.5**	**55**	**77.5**	**100**	**125**	**150**
E (GPa)	**0.01**	2.11E-04	2.44E-04	2.81E-04	3.20E-04	3.59E-04	3.97E-04	4.42E-04
	0.1	1.74E-04	3.20E-04	4.79E-04	6.32E-04	7.91E-04	9.77E-04	1.26E-03
	1.0	1.96E-04	6.55E-04	1.64E-03	3.80E-03	6.90E-03	1.06E-02	1.56E-02
	4.5	3.78E-04	2.99E-03	8.14E-03	1.36E-02	1.92E-02	2.49E-02	3.18E-02
	8.0	5.07E-04	4.47E-03	1.02E-02	1.59E-02	2.18E-02	2.76E-02	3.48E-02

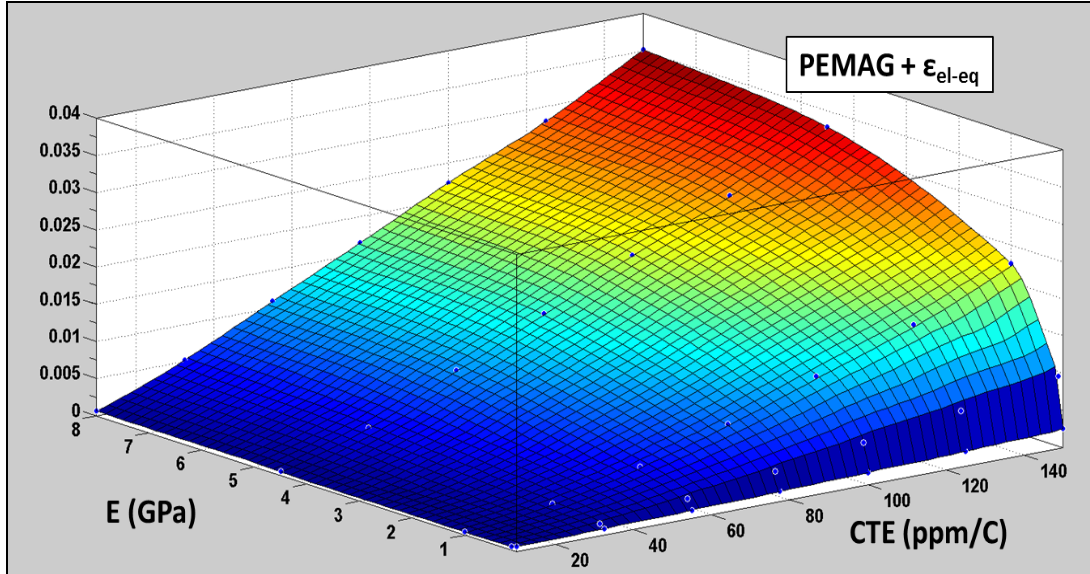

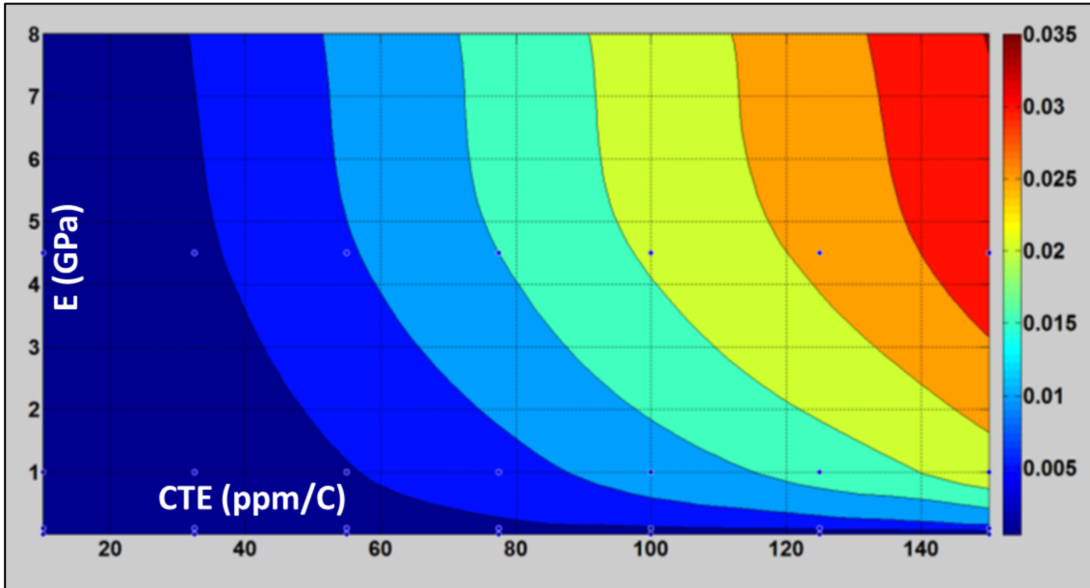

Figure 32. Response surface (top) and contour (bottom) for the average equivalent strain values calculated at the lead bend

Table 15. PEMAG+ ε_{el-eq} values for lead bend as a function of encapsulant properties

Lead Bend		**CTE** (ppm/C)						
		10	**32.5**	**55**	**77.5**	**100**	**125**	**150**
E (GPa)	**0.01**	7.12E-04	8.94E-04	1.13E-03	1.38E-03	1.67E-03	2.01E-03	2.52E-03
	0.1	5.07E-04	1.31E-03	2.51E-03	3.92E-03	5.51E-03	7.20E-03	9.34E-03
	1.0	4.08E-04	1.99E-03	4.71E-03	8.18E-03	1.23E-02	1.68E-02	2.25E-02
	4.5	5.16E-04	4.17E-03	9.58E-03	1.50E-02	2.06E-02	2.61E-02	3.28E-02
	8.0	6.28E-04	5.22E-03	1.09E-02	1.65E-02	2.23E-02	2.81E-02	3.52E-02

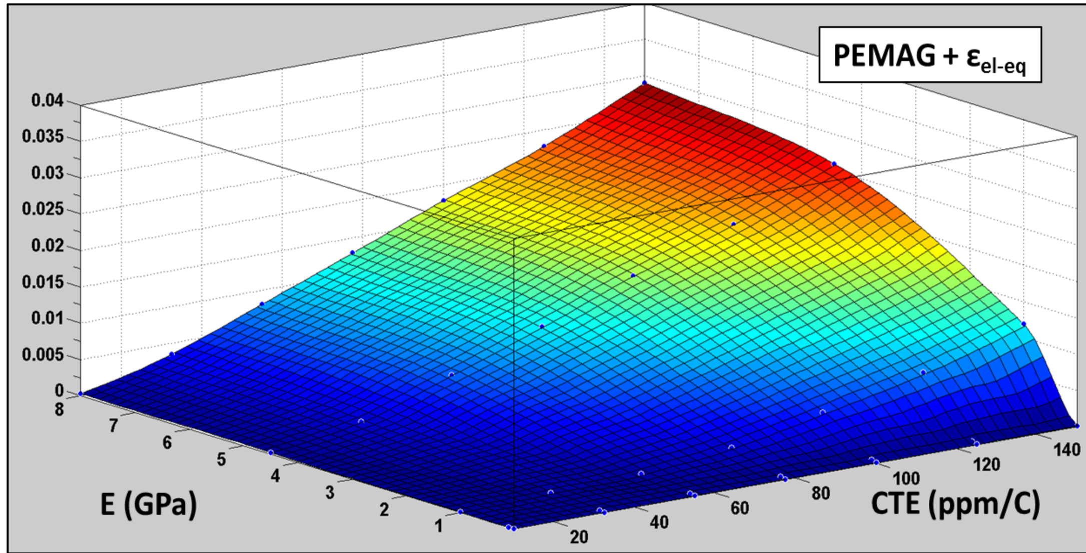

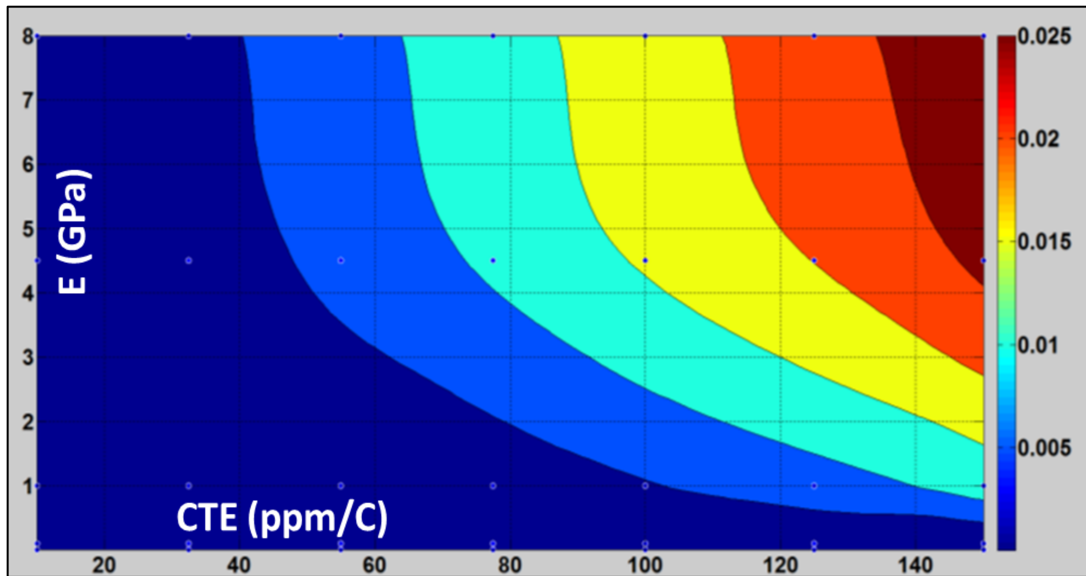

Figure 33. Response surface (top) and contour (bottom) for the average equivalent strain values calculated at the busbar adjacent to the weld regions

Table 16. PEMAG + ε_{el-eq} for busbar adjacent to the weld as a function of encapsulant properties

Busbar at Weld Region		**CTE** (ppm/C)						
		10	**32.5**	**55**	**77.5**	**100**	**125**	**150**
E (GPa)	**0.01**	4.17E-05	5.17E-05	6.35E-05	7.58E-05	8.91E-05	1.03E-04	1.19E-04
	0.1	2.89E-05	8.53E-05	1.52E-04	2.17E-04	2.84E-04	3.55E-04	4.46E-04
	1.0	6.90E-05	4.26E-04	7.82E-04	2.19E-03	4.68E-03	7.74E-03	1.19E-02
	4.5	2.32E-04	2.18E-03	6.39E-03	1.08E-02	1.55E-02	2.01E-02	2.59E-02
	8.0	3.38E-04	3.45E-03	8.11E-03	1.29E-02	1.78E-02	2.28E-02	2.90E-02

Chapter 3: Design optimization of an encapsulated beam-lead component using a combined FEM and DOE approach

In this chapter, a Taguchi fractional-factorial parametric study is conducted to explore how the stress distribution in the encapsulated beam-lead component of Chapter 2 depends on selected design features. These features include the encapsulant material properties, encapsulant out-of-plane thickness, lead dimensions and geometry, and busbar dimensions. Similar to the previous study, the assembly consists of a beam-lead component welded to slender copper busbars and encapsulated in a single encapsulant material. As in Chapter 2, the assembly is modeled using finite elements.

3.1 Approach

A Taguchi Design of Experiments approach is for this parametric sensitivity study. An initial screening study with a larger set of potential design parameters is used to identify the critical design parameters impacting the outcome of interest. In this study the interest is in reducing the deformation and stresses around the package, leads, and interconnect regions. Once the critical design parameters have been identified, a more detailed characterization design of experiment matrix is employed. This characterization study utilizes more runs with less parameters, allowing for greater resolution and granularity on the main effects and parameter interactions. This helps identify the critical parameters and their optimal settings. Response surface models can also be developed to help identify which designs are plausible and which are not realistic for a particular application or combination of parameters. A flowchart of the approach for this study can be seen in Figure 34.

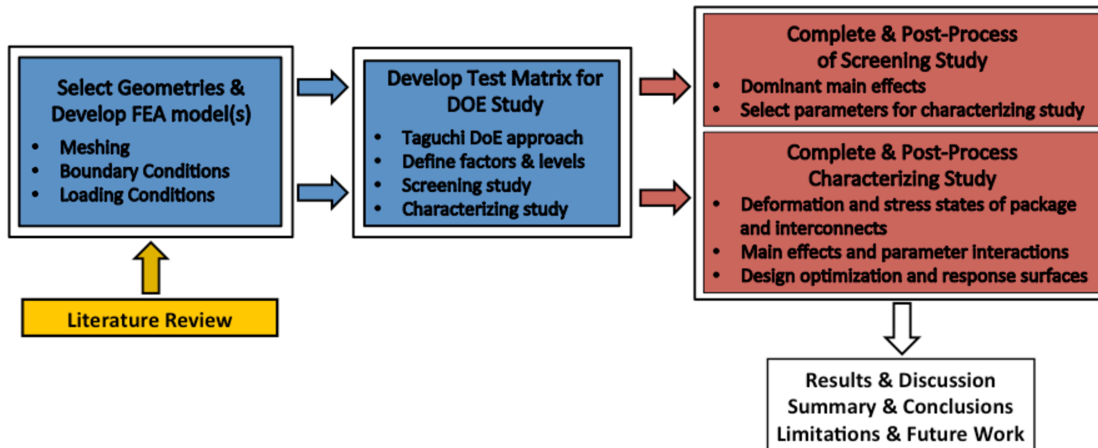

Figure 34. Flowchart of Approach for Study 2

3.1.1 Assembly Configuration, Boundary Conditions, and Loading Conditions

The model is similar to that used in the previous study, with select features varied as part of the parametric study. This is explained in detail in the next two sections. The boundary conditions and weld regions are modeled the same way as in the previous chapter. An Accelerated Thermal Cycling (ATC) loading profile is used in the DOE study. ATC tests are often used in both modeling and experimental approaches to generate thermo-mechanical fatigue failures in components of complex assemblies. A popular example is solder interconnection failure in electronic assemblies. The ATC selected in this study is based on an experimental test profile used for a similar assembly, and is in line with typical profile characteristics seen in JEDEC standard JESD22-A104D [52]. The ATC has the following characteristics:

Table 17. ATC profile characteristics

Parameter	T_{min} (^oC)	T_{max} (^oC)	ΔT (^oC)
Value	-40	85	125

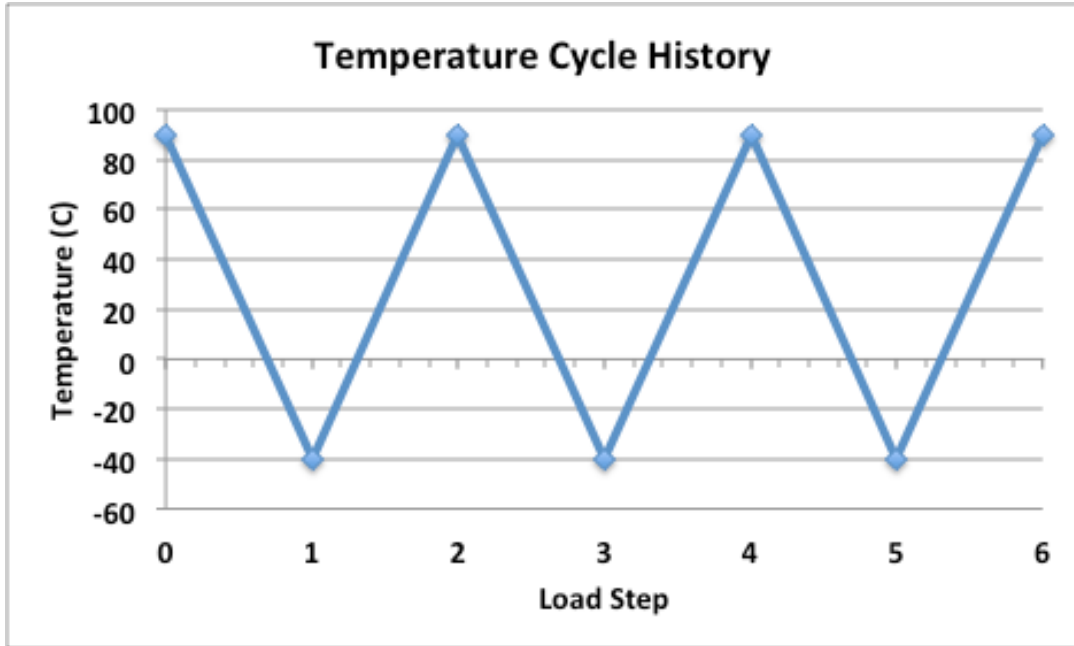

Figure 35. Accelerated thermal cycle profile

This is a static analysis with rate independence, therefore no dwell is used and no ramp rate is specified. As mentioned in the material properties section, there is no solder in this model and a simplified modeling approach is used for the encapsulant material (namely no viscoelasticity is modeled for the encapsulant). Therefore the effects of a temperature dwell or specific ramp rate are assumed to be negligible. This allows for reasonable computation time to run all cases within design space. Sufficiently small increments lengths are used in each load step such that the model converges. A three cycle profile is applied with an initial stress free temperature at $T_{max} = 90^{o}C$, based on the cure process that would take place for a typical laminate or encapsulated assembly. All measured metrics of interest are output during the final cycle. The profile is seen in Figure 35. It is important to note that this cyclic thermal loading is applied as a field condition. This assumes that there are no gradients in the model.

3.2 Screening Study – Background, Test Design, and Approach

A parametric study is conducted using a fractional-factorial approach Design of Experiments (DOE). The primary goal of the study is to determine which parameters have the dominant influence on the stress and deformation in the components leads, interconnects and suspected failure sites. The variable of interest is the equivalent strain metric used in the previous chapter, calculated at multiple locations within the assembly. In order to accomplish this, a parameter test matrix is developed for the fully encapsulated thermal model. Design parameters are systematically varied using a Taguchi scheme. The Taguchi approach provides the ability to identify the influence of critical parameters with a significantly reduced number of runs.

3.2.1 Factor selection

Several design parameters are selected as part of the initial screening study, as listed in Table 18. For this screening study a L_{12} Taguchi orthogonal array is selected.

Table 18. Taguchi DOE screening study - factors and levels

Parameter	Factor	Levels	Level 1	Level 2
Material Properties	A	2	E = 0.01GPa CTE = 150ppm/^{o}C	E = 8GPa CTE = 10ppm/ ^{o}C
Stress Relief Type	B	2	Flat	GW Lead
Length of Encapsulation	C	2	2x Diode Region (Per Side)	10x Diode Region (Per Side)
Busbar Height	D	2	0.4 mm	0.6 mm
Busbar Out-of-Plane Thickness	E	2	5.3 mm	6.625mm
Lead Out-of-Plane Thickness	F	2	3.0 mm	4.4 mm

Encapsulant Out-of-Plane Thickness	G	2	8.25mm	11.0mm

The seven design parameters for the screening study are varied between two levels – a high and low level, in accordance with Taguchi's L_{12} array, to examine their influence on the stresses experience by package, leads and interconnect regions. In the screening study only the main effects are examined. In the characterization study, the main effects and select 2nd order parameter interactions are examined based on the critical parameters identified in the screening study. Detailed review of each of the seven design parameters follows below.

Table 18 – *Factor A (Material Properties).* Two sets of encapsulant material properties are considered in the screening Taguchi study. Similar to the previous chapter, the elastic modulus and coefficient of thermal expansion are varied for each set of encapsulant properties. In both cases, the encapsulant is model with temperature dependent elastic properties. Similar to the previous chapter, the encapsulant properties are varied up to ± 20% as function of temperature. These properties are specifically of interest because they are important driving forces of the mechanical stresses generated on the encapsulated component during thermal cycling. The first encapsulant property set, E = 0.01GPa (10MPa) and CTE = 150ppm/^{o}C is meant as a rough linear elastic approximation of a typical elastomer encapsulant. Silicone rubber, a common example of such a material, is widely used in industry for molding and encapsulation of electronics. This type of rubber or elastomer is frequently modeled with hyperplastic constitutive models. This is due to the fact that

linear elastic models do not always adequately capture the nonlinear nature of the rubber's mechanical properties, especially for applications that require high fidelity. In this study, the elastomer is approximately represented with elastic material having a low Young's modulus and high coefficient of thermal expansion. The second encapsulant property set, E = 8.0GPa (10MPa) and CTE = 10ppm/^{o}C is meant to represent the behavior of typical stiff polymers, resins, epoxies or molding compounds with fillers. These two materials are selected as they are typically used in various encapsulation applications and exhibit a rather sizeable difference in material properties. The materials are selected from opposite corners of the design space from the previous study (labeled as Regions A and C of Figure 17).

Table 18 – *Factor B (Stress Relief Type).* For the initial screening study two types of stress reliefs are considered. Here, stress relief refers to the geometric compliance incorporated into component lead-busbar interconnect region. The two configurations are denoted as 'flat' and 'gull wing.' For the flat configuration, the component leads are unformed as seen in Figure 36b. The components leads overlap the busbar and welded in a lap joint manner. This configuration has a stiff interconnection. Please refer to Appendix E for local images of the meshed diode regions in this study.

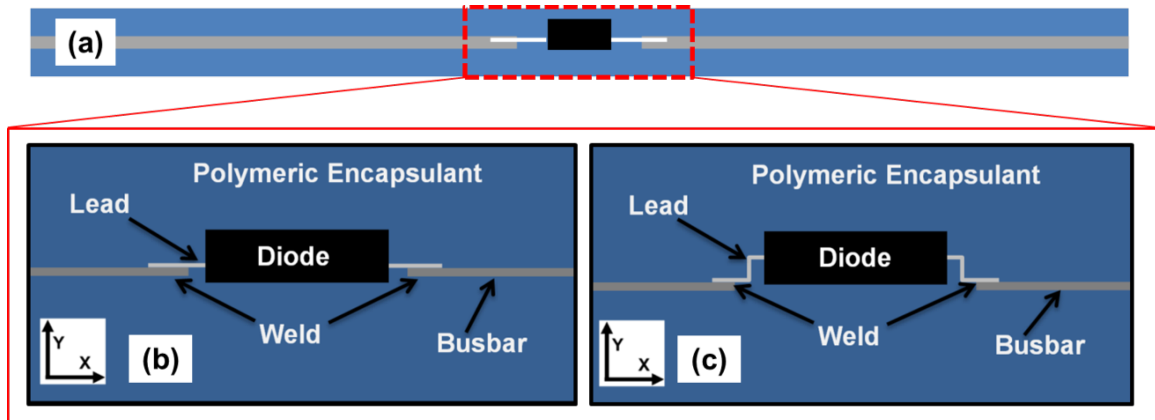

Figure 36. (a) Global schematic (b) Flat configuration (c) Gull wing configuration

The compliant configuration (Figure 36c) utilizes the same beam lead component. In this case, the compliance is incorporated by forming a gull wing shape in either the diode lead or the busbar itself. In both cases the lead is spot welded to the busbar. Please refer to Section 2.3.1 for further details on the FE model geometry, meshing, and material properties.

Table 18 – *Factor C (Length of Encapsulation)*. Two lengths of busbar and encapsulant are considered. The lengths are determined as a function of the length of the diode region. The low level (short length) has a span of busbar and encapsulant equivalent to approximately twice the length of the diode region on either side of the diode. Similarly, the high level has approximately ten times the length of the diode region on either side of the diode.

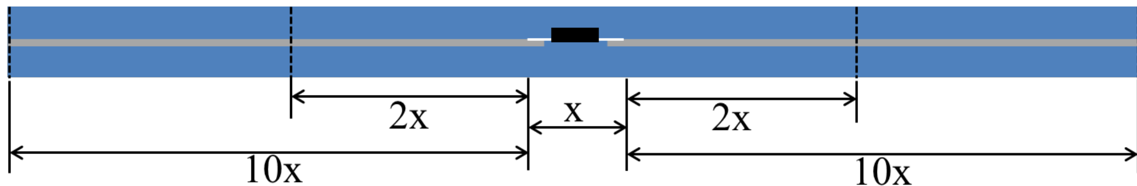

Figure 37. Length of encapsulation as a function of the diode region

Table 19. Length of busbar and encapsulant as a function of diode region

	Flat Lead Model

				Total Length	
	Diode Region	**2x (per side)**	**10x (per side)**	**2x Model**	**10x Model**
Length (mm)	23.8	47.6	238.0	119.0	499.8
	Gullwing Lead Model				
				Total Length	
	Diode Region	**2x (per side)**	**10x (per side)**	**2x Model**	**10x Model**
Length (mm)	21.7	43.4	217.0	108.5	455.7

Figure 37 depicts the different lengths of encapsulation as a function of the length of diode region. The length of the diode region varies slightly depending on the configuration, therefore the lengths of busbar and encapsulant, shown in Table 19, also vary slightly as a function of the configuration. Mechanical stresses are generated in this assembly during thermal cycling as a result of expansion mismatches between the encapsulant and other materials. Therefore changing the length and configuration of the encapsulant and busbar can have an effect on those stresses. It is hypothesized that increasing the length and volume of the encapsulant may lead to higher stresses within the assembly. However, it is difficult to estimate how large such an effect is relative to other variable parameters. Including this parameter as part of the screening DOE study will help determine the influence of the encapsulant length on the stresses in the component and interconnect regions. From a product design perspective, it is important to consider what configurations and dimensions are plausible or practical for a specific application. A wide range of encapsulant and busbar lengths are used in this study in order to try and reasonably bound the lengths that could be of interest to designers of such an encapsulated structure in electronic systems.

Table 18 – *Factor D (Busbar Height).* This parameter and its two levels are selected with several considerations in mind. The first is that adjusting the busbar geometry will have an effect on the system's structural stiffness and could therefore influence the deformation and stress states under cyclic thermal loading. This could cause a change or shift in the stresses and strains occurring at the critical failure sites. Second, the busbar height is something that is relatively easy to adjust from a manufacturability perspective.

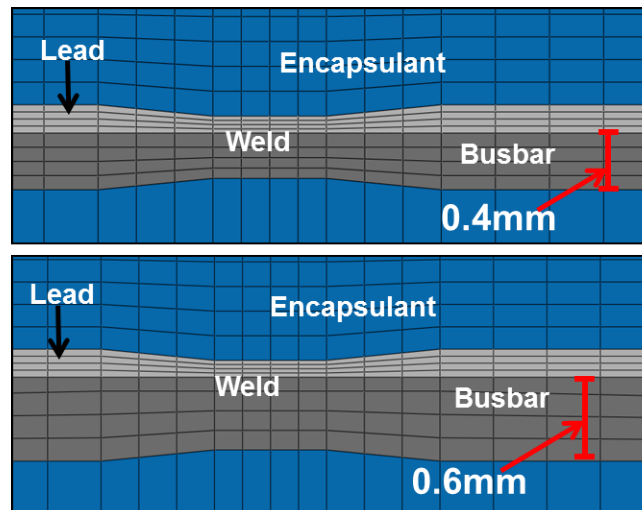

Figure 38. Busbar thickness adjustment for screening study

Additionally, there may also be piece-to-piece variability in the busbar during production. Therefore studying such a parameter may be a rapid and cost-effective way to do a relative comparison of different heights to also understand the influence of manufacturing tolerances. Figure 38 shows FE model snapshots of the two levels of busbar height.

Table 18 – *Factor E (Busbar Out-of-Plane Thickness).* This parameter is labeled as dimension 'b' of Figure 5, which contains a top view schematic of the model. Similar

to the busbar height (Factor D), adjusting the busbar geometry will have an effect on the system's structural stiffness and could therefore influence the deformation and stress states under cyclic thermal loading. Since this parametric study is run with two-dimensional FEA models, the out-of-plane thickness is varied by changing the section thickness of the busbar material. The manufacturer of the particular beam lead component used for this study suggests a pad layout of at least 5.1 mm for out-of-plane direction. Therefore, the minimal or lower level thickness is set as 5.3 mm (see Table 18). The upper level is set at 6.625 mm, which represents a 25% increase in out-of-plane thickness for the busbar. This provides a good range of variability for the assembly that is also reasonably within the typical range of manufacturing for such a busbar material. The busbar thickness in the weld region is intended to represent the weld diameter and is hence not adjusted in this case.

Table 18 – *Factor F (Lead Out-of-Plane Thickness).* The out-of-plane dimensions can be visualized by examining Figure 5. In this case, dimension 'c' represents the out-of-plane thickness of the busbar. The out-of-plane thickness was selected in this case so as to not exceed the out-of-plane thickness of the busbar and beam-lead package. Similar to Factor E, adjusting this parameter will have an effect on the system's structural stiffness and will potentially have to carry more axial stresses (if the out-of-plane thickness is reduced) during horizontal extension and compression during thermal cycling. In this case the nominal manufacturer value from this type of COTS component is 4.4 mm. The second value selected is 3.0mm which represents approximately a 30% reduction in out-of-plane thickness.

Table 18 – *Factor G (Encapsulant Out-of-Plane Thickness)*. Similar to the previous two factors, this parameter is best visualized as dimension 'a' of Figure 5. The material must fully encapsulate the component, and therefore should be at least as long out of plane as the component. Another consideration is to not use so much material that it becomes inefficient from a manufacturing perspective. The increase/decrease in encapsulant material volume could have a large effect on the stress state of the component and interconnect regions, as all mechanical stresses are generated from thermal expansion mismatches during temperature cycling. In this case values of 11.0 mm and 8.25 mm are selected. 11.0 mm represents approximately double the value of the busbar and component out-of-plane thickness. 8.25 mm, which is a 25% reduction from the 11.0 mm, represents approximately a 1.5x the value of busbar and component out-of-pane thickness.

3.2.2 Test matrix design

Taguchi test orthogonal arrays use a special form of fractional factorial design. In typical Taguchi robust designs, an inner and outer array system is used. In this case, the inner array is populated by parameters that are considered controllable factors. These normally consist of design parameters that are of primary interest in the design optimization process. An outer array is also developed, consisting of uncontrollable or expensive (i.e. difficult to change) parameters known as noise factors. Examples of noise factors include environmental variabilities such as temperature & humidity, piece-to-piece quality variability, differences in the work of different operators or machines, and other uncontrollable factors. The inner array is then repeated over the

outer array and signal-to-noise ratios can be calculated. This allows the ability to study and minimize the effects of the uncontrollable factors by adjusting those that are controllable. In experimental settings, tests are often replicated and a mean response is evaluated using the Taguchi method. In the case of FEM analysis, it is not feasible to produce replicates for the same conditions. A consequence of using orthogonal arrays is that all levels of each variable are considered to be equally significant and that each variable is evaluated independent of each other.

An L_{12} Taguchi orthogonal array is used in this initial screening study. This orthogonal array requires twelve runs and can support up to eleven two-level parameters. This particular array only examines the main effects of the parameters. This study utilizes the seven two-level parameters described in Table 18, therefore only the first seven columns of the L_{12} orthogonal array are needed. The combinations of the parameters for each run are displayed in Figure 39.

$L_{12}(2^{11})$

No.	1	2	3	4	5	6	7	8	9	10	11
1	1	1	1	1	1	1	1	1	1	1	1
2	1	1	1	1	1	2	2	2	2	2	2
3	1	1	2	2	2	1	1	1	2	2	2
4	1	2	1	2	2	1	2	2	1	1	2
5	1	2	2	1	2	2	1	2	1	2	1
6	1	2	2	2	1	2	2	1	2	1	1
7	2	1	2	2	1	1	2	2	1	2	1
8	2	1	2	1	2	2	2	1	1	1	2
9	2	1	1	2	2	2	1	2	2	1	1
10	2	2	2	1	1	1	1	2	2	1	2
11	2	2	1	2	1	2	1	1	1	2	2
12	2	2	1	1	2	1	2	1	2	2	1
	1	2									

Figure 39. Taguchi L_{12} orthogonal array

Table 20. L_{12} Taguchi screening design

L12 – Taguchi Screening Design							
Factor	**A**	**B**	**C**	**D**	**E**	**F**	**G**
Run	**Material Properties**	**Stress Relief Type**	**Length of Encapsulant**	**Busbar Height (mm)**	**Busbar Thickness (mm)**	**Lead Thickness (mm)**	**Encapsulant Thickness (mm)**
1	Silicone	Flat	2x	0.4	5.3	3.0	8.25
2	Silicone	Flat	2x	0.4	5.3	4.4	11.0
3	Silicone	Flat	10x	0.6	6.625	3.0	8.25
4	Silicone	GW	2x	0.6	6.625	3.0	11.0
5	Silicone	GW	10x	0.4	6.625	4.4	8.25
6	Silicone	GW	10x	0.6	5.3	4.4	11.0
7	Epoxy	Flat	10x	0.6	5.3	3.0	11.0
8	Epoxy	Flat	10x	0.4	6.625	4.4	11.0
9	Epoxy	Flat	2x	0.6	6.625	4.4	8.25
10	Epoxy	GW	10x	0.4	5.3	3.0	8.25
11	Epoxy	GW	2x	0.6	5.3	4.4	8.25
12	Epoxy	GW	2x	0.4	6.625	3.0	11.0

Table 20 contains the permutations of runs for the L_{12} array. Shorthand is used for the material property and stress relief type parameters to identify the different levels. For example, "silicone" is used in place of the material property level containing a small modulus and large CTE value, while "epoxy" is used for the other level. Several FE models are built in order to capture all the different combinations of the Taguchi design. The models are run for all twelve cases. Post-processing and analysis of the results are discussed in the next section.

3.3 Screening Study - Results and Discussion

This section contains the result and discussion of the L_{12} screening study. Similar to the study in the previous chapter, the total equivalent strain is used as a comparison metric across all locations and for all runs of the fractional-factorial design. The same four locations in the assembly from the previous chapter are used to measure and compare the parameters of interest in this study. Please refer to Figure 29 for these locations.

3.3.1 Screening study - equivalent strain results

Table 21 contains the volume weighted average total equivalent strain values. This value is calculated using the same approach as the previous chapter. In this case, since a cyclic thermal loading profile is used, PEMAG represents a slightly different value. While it is always positive, PEMAG is able to reverse under cyclic loading. The plastic equivalent portion of this calculation is therefore estimated as range of the maximum and minimum values over the last cycle.

Table 21. Equivalent total strain values for the screening study at various locations of interest

	PEMAG + $\varepsilon_{el\text{-}eq}$ (with element averaging)				
Run	**Lead at EMC Package**	**Lead Adjacent to Weld Region**	**Busbar Adjacent to Weld Region**	**Lead Bend**	**Max Regardless of Location**
1	1.03E-03	1.06E-03	8.14E-05	9.97E-04	1.06E-03
2	4.96E-04	3.96E-04	1.05E-04	4.69E-04	4.96E-04
3	2.04E-03	2.21E-03	2.29E-05	2.14E-03	2.21E-03
4	3.88E-03	2.02E-03	5.75E-05	1.15E-02	1.15E-02
5	4.71E-03	1.26E-03	1.87E-04	6.02E-03	6.02E-03
6	2.59E-03	7.07E-04	1.92E-04	7.45E-03	7.45E-03
7	8.66E-04	1.14E-03	6.41E-04	1.02E-03	1.14E-03
8	1.85E-03	2.03E-03	6.52E-04	1.93E-03	2.03E-03
9	9.77E-04	1.22E-03	2.56E-04	1.16E-03	1.22E-03
10	2.88E-03	2.64E-03	5.68E-04	2.88E-03	2.88E-03
11	7.90E-04	8.59E-04	3.77E-04	9.79E-04	9.79E-04
12	4.13E-03	3.88E-03	5.09E-04	4.35E-03	4.35E-03

For this analysis the maximum total equivalent strain value is taken regardless of location. The reasoning behind this is that the largest strain may shift location from run to run, thereby shifting the failure location as well. Accordingly, it is logical to use the maximum strain value for each run in order to identify the most influential parameters. For the ‘Max’ column of Table 21 the minimum value occurs at run 11 with a value of 9.79E-4 while the maximum value occurs in run 4 with a value of 1.15E-2. This is a considerably large range, with more than an order of magnitude difference between the largest and smallest values. In almost all cases, the largest amount of total equivalent strain occurs at the lead bend and the lead adjacent to the weld region, however in some cases it also occurs at the lead adjacent to the EMC package.

Figure 40 contains the plots of the main effects of the means of each parameter. Figure 40a contains individual plots of each of the main effects while Figure 40b contains plots of the main effects combined on a single axis. These two plots highlight the influential main effects. It is evident that the material properties and stress relief type have the highest influence on the maximum total equivalent strain. Table 22 provides a range of the effect for the mean of each parameter (labeled ‘delta’) as well as ranking of all the parameters relative to one another. The ranking is as follows from most influential to least influential: material properties (factor B), stress relief type (factor A), busbar out-of-plane thickness (factor E), encapsulant out-of-plane thickness (factor G), busbar out-of-plane thickness (factor D), lead out-of-plane thickness (factor F), and length of encapsulation (factor C).

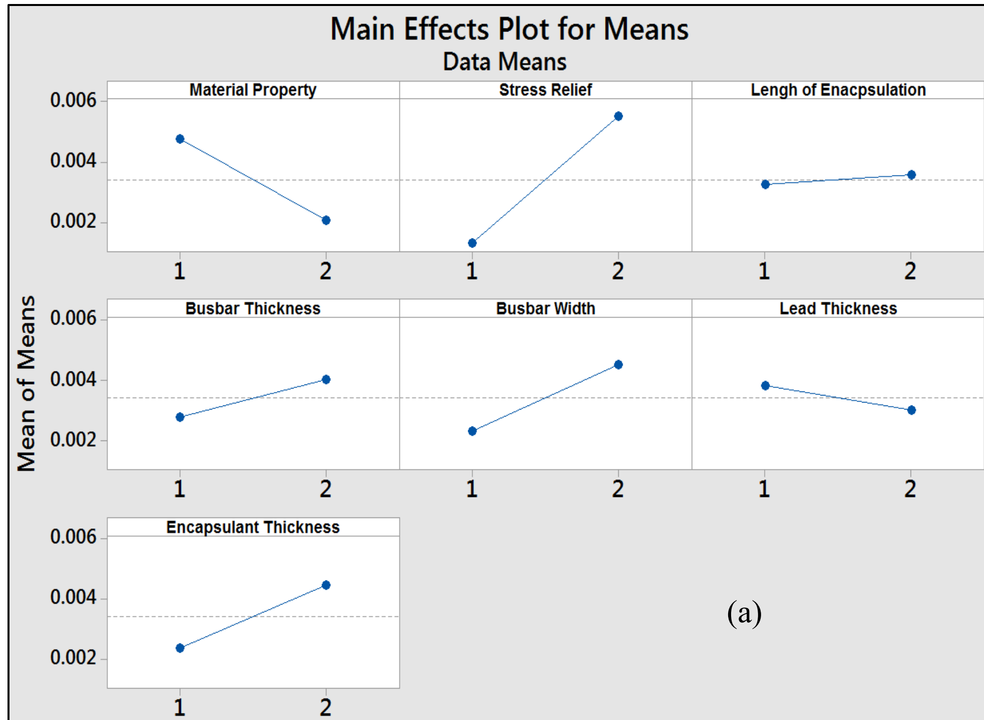

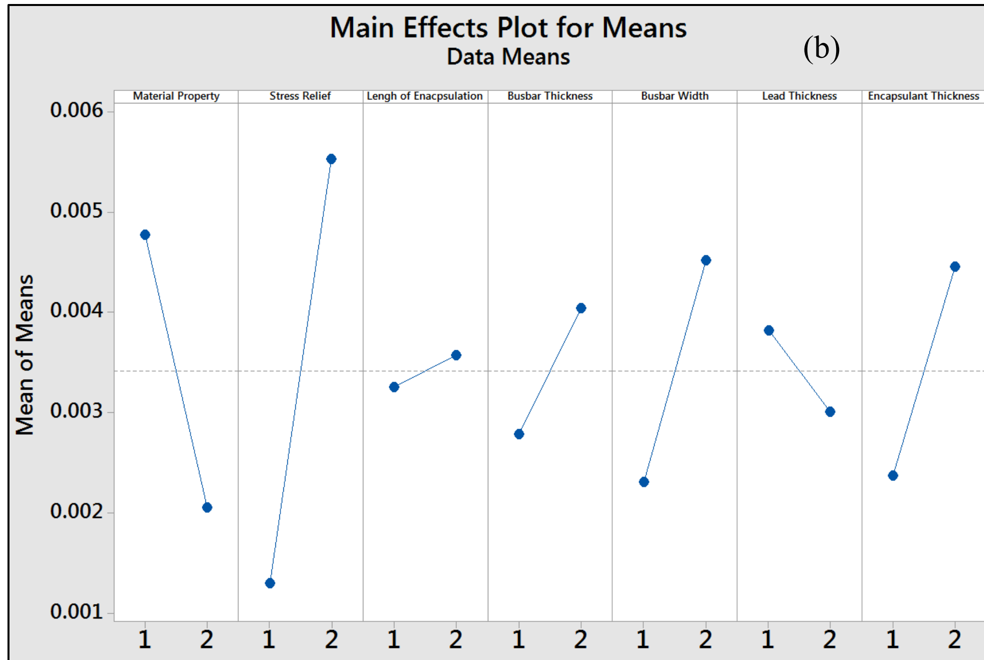

Figure 40. Main effects of parameters from screening study - (a) individual parameters (b) all parameters plotted side-by-side

Table 22. Response table for main effect means and parameter rankings

Level	A	B	C	D	E	F	G
1	0.00478	0.001359	0.003261	0.002806	0.002333	0.003849	0.002394
2	0.002102	0.005523	0.003621	0.004076	0.004549	0.003033	0.004488
Delta	0.002678	0.004163	0.00036	0.00127	0.002216	0.000817	0.002094
Rank	2	1	7	5	3	6	4

Table 23 contains an ANOVA analysis of the results of the study. For a significance level of 0.01, it is clear from the P-values of the stress relief type (0.017) and material properties (0.066) that these two parameters are significant. The P-values of the busbar out-of-plane thickness (0.106) and encapsulant out-of-plane thickness (0.121) are also reasonably close to being statistically significant. This two-level DOE analysis may be aliasing some of the effects of these parameters (i.e. non-linear effects), therefore it is useful to include parameters in the more detailed characterization study that follows this analysis. Accordingly, these four factors (B, A, E and G) are selected for the expanded characterization study.

Table 23. Anova for L_{12} screening study

Source	Factor	DF	Seq SS	Adj SS	Adj MS	F	P
Material Properties	A	1	0.000022	0.000022	0.000022	6.32	0.066
Stress Relief Type	B	1	0.000052	0.000052	0.000052	15.27	0.017
Length of Encapsulant	C	1	0	0	0	0.11	0.752
Busbar Height	D	1	0.000005	0.000005	0.000005	1.42	0.299
Busbar Thickness	E	1	0.000015	0.000015	0.000015	4.33	0.106
Lead Thickness	F	1	0.000002	0.000002	0.000002	0.59	0.486
Encapsulant Thickness	G	1	0.000013	0.000013	0.000013	3.87	0.121
Residual Error		4	0.000014	0.000014	0.000003		
Total		11	0.000122				

Table 24 contains the coefficients of a linear model fit the means effects. This allows for a rough estimation of the maximum total equivalent strain value at any combination of the parameters in the screening study. An R^2 value of 0.89 indicates a

reasonable fit. A higher order fit, with non-linear terms, can also be obtained to try and increase the goodness of fit.

Table 24. Linear model fit to main effect means terms for screening study

Term	Coefficient
Constant	0.003441
Material Properties	0.001339
Stress Relief	-0.00208
Length of Encapsulant	-0.00018
Busbar Height	-0.00064
Busbar Thickness	-0.00111
Lead Thickness	0.000408
Encapsulant Thickness	-0.00105
R^2 = 88.9%, R^2(adj.) = 69.4%	

Figure 41 contains analysis of the regular residuals from this analysis. This is the difference between the values observed and those predicted by the model. The residual probability plot in the top left corner as well as the residual versus frequency histogram in the bottom left corner of Figure 41 indicate that the residuals follow a fairly normal distribution. This is a positive indication of goodness of the model fit.

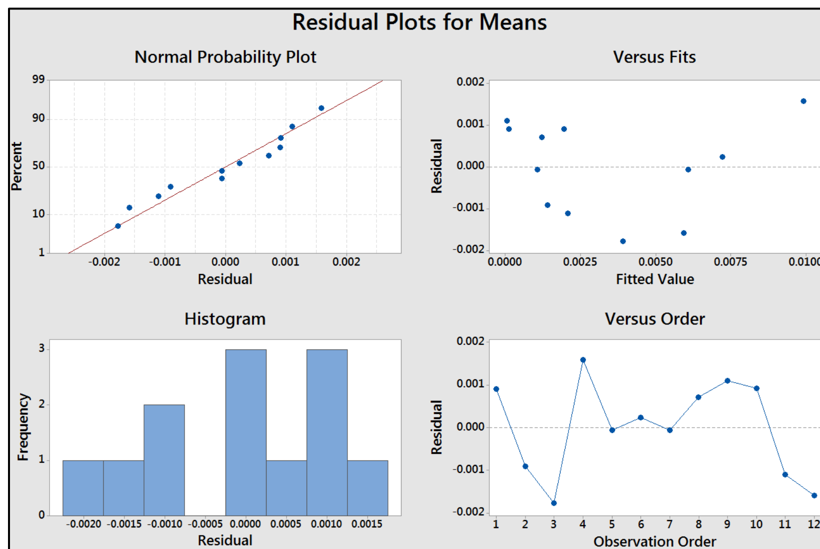

Figure 41. Plots of the residual means of model fit for screening study

3.4 Characterization Study – Background, Factor Selection, and Test Design

For the characterization study a L_{27} Taguchi orthogonal array is selected to expand on the results of the screening study. This section provides a detailed overview of the selected factors and test matrix design.

3.4.1 Factor selection

Factors are selected based on the results of the previous screening study. The four factors with the largest effects from the screening study are selected for this detailed characterization study. While the screening study helps identify critical parameters, using a two-level approach makes the assumption that these effects are linear. Consequently, all parameters are expanded to three levels for the characterization study. Expanding to a third level gives greater granularity to parameter main effects and interactions, allowing nonlinear non-monotonic effects to be captured. This additional level is included in column two ('Level 2') of Table 25. A best attempt is made to ensure that the additional level is bounded by the initial high and low levels of the screening study. Although parameter effects and parameter interactions may exhibit some non-linear trends within their bounded range, the critical factors identified in the screening study were for a specific range of dimensions or configurations. Selecting a third level outside of this range may not only be impractical for the assembly design, but also may no longer be linked to the ranking of the parameters' effects given in the results of the screening study. For quantitative parameters this expanded level is fairly straightforward to select, while for qualitative parameters this is more challenging. Aside from an additional third level, the

remaining parameters are the same as those described in Section 3.2.1 for the screening study. Please refer to that section for a comprehensive description of those parameters. Details of the expanded levels and any changes to all of the parameters in Table 25 are given in the next section.

The values of the three parameters found to be least influential from the screening study were fixed at a single level for the characterizing study. The lead out-of-plane thickness was fixed at 4.4 mm, as this was the nominal value provided by the manufacturer of this COTS component. The vertical height of the busbar was fixed at a value of 0.4 mm. The length of the encapsulant was fixed at a value of 10 times that of the diode region.

Table 25. Taguchi DOE characterizing study - factors and levels

Parameter	Factor	Levels	Level 1	Level 2	Level 3
Material Properties	A	3	E=0.01GPa CTE=150ppm/C	E=2GPa CTE=55ppm/C	E=8GPa CTE=10ppm/C
Stress Relief Type	B	3	Flat	Low Gull Wing	High Gull Wing
Busbar Out-of-Plane Thickness	C	3	5.3 mm	5.9625mm	6.625mm
Encapsulant Out-of-Plane Thickness	D	3	8.25mm	9.625mm	11.0mm

Table 25 – *Factor A (Material Properties).* Three sets of encapsulant properties are considered. Levels 1 and 3 are the same as those described in the screening study. The additional Level 2 consists of an encapsulant property set of E = 2.0GPa and CTE = 55ppm/^{o}C. This is meant to represent a material from Region B of the design

space from the previous chapter (Figure 17). The characterization study selects materials along the diagonal of the design space, with a single material selected from each region A-C (Figure 42). Selecting a material from each of the regions provides a reasonable variety of potential encapsulant materials to be included in the DOE study.

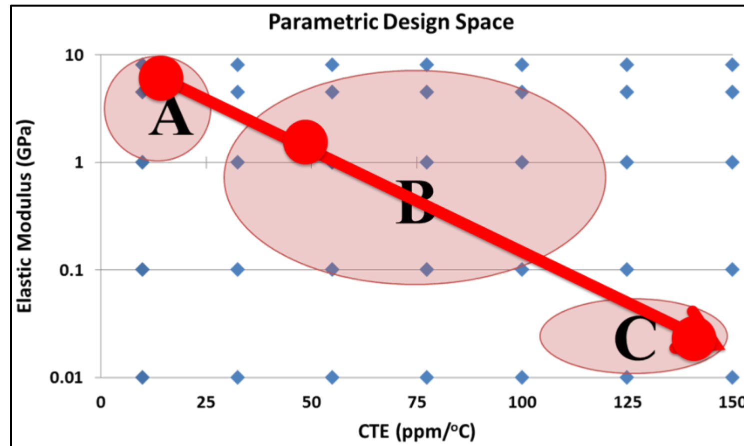

Figure 42. Encapsulant property sets selected from the design space in Chapter 2

Table 25 – *Factor B (Stress Relief Type).* Three stress relief types are considered. The different stress relief configurations are qualitative factors, making it non-trivial to select a middle level. Levels 1-3 represent progressively increasing lead stiffness. Levels 1 and 3 are the same as those included in the screening study. Level 2 is a gull wing configuration with a lower standoff height and bends with smaller radii of curvature. Therefore Levels 2 and 3 represent variations of a gull wing configuration while Level 1 represents an unformed flat lead configuration. The flat configuration is how the component is provided by the manufacturer, so this serves almost as a control case. The gull wing formation with the higher standoff, donated as GW_{High}, has bends with radii of curvature of approximately 0.7mm and a standoff height of approximately 1.35mm. The gull wing formation with the lower standoff, donated as

GW_{Low}, has bends with radii of curvature of approximately 0.4mm and a standoff height of approximately 0.6mm. The total lead length, 9.0mm, is the same regardless of the configuration. Therefore the overlap length of the lead and busbar is adjusted for the different configurations. This however, does not affect the geometry of the welded region, which is the same regardless of the configuration. Figure 43 contains a schematic with all three configurations. Although they are not to scale, Figure 43c and Figure 43d give a relative comparison of the two gull wing configurations. The components lead's structural stiffness is a function of both its material properties and its geometry. Decreasing the component's standoff height should reduce the lead's compliance. This will have an impact on the deformation and stress state of the assembly under the same loading conditions. Please refer to Appendix E for local images of the meshed diode regions for each of the three configurations in this second study.

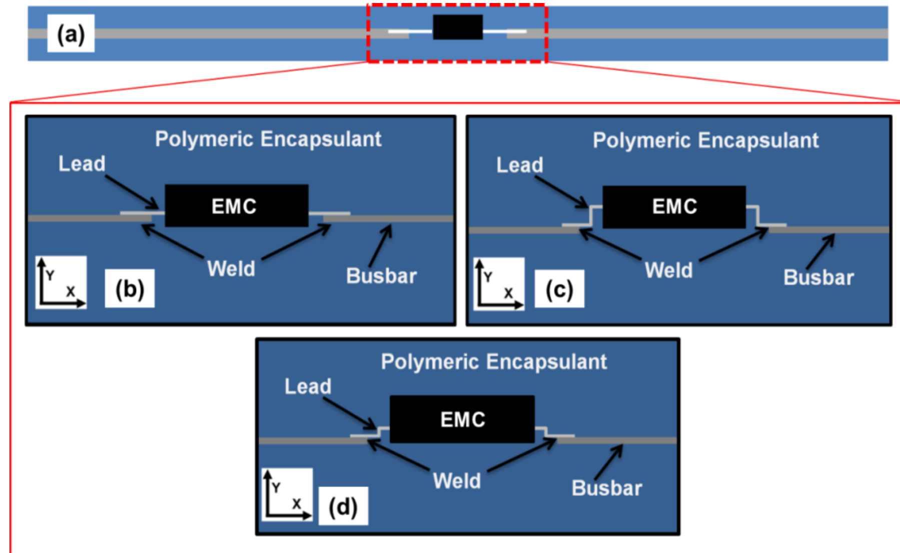

Figure 43. (a) Global schematic (b) Flat lead (c) High gull wing lead (d) Low gull wing lead

Table 25 – *Factor C (Busbar Out-of-Plane Thickness).* Three values for the busbar out-of-plane thickness are considered. The adjustment of this parameter can be visualized from the 'b' dimension in the top view schematic of the model in Figure 5. The busbar geometry will have an effect on the system's structural stiffness and could therefore influence the deformation and stress states under cyclic thermal loading. The expanded value is selected in between the two levels of the screening study. This represents a 25% range from the lowest level, which is the nominal value provided by the manufacturer.

Table 25 – *Factor D (Encapsulant Out-of-Plane Thickness).* Three values for the encapsulant out-of-plane thicknesses are considered. Similar to factor C, this is a quantitative factor. It is therefore straightforward to select dimension values between the values of the screening study. The range between the greatest and smallest values is 25% of the highest level, which is the nominal value provided by the manufacturer. Mechanical stresses are generated during cyclic thermal loading, due to the presence of different materials with different expansion coefficients. The encapsulant, which makes up the largest portion of the assembly, is a driving force of these thermomechanical stresses. Finding an optimal amount of encapsulant may not only improve reliability but could also potentially reduce costs for the assembly.

3.4.2 Test matrix design

This new four factor three-level design is captured with a Taguchi L_{27} orthogonal array. All four factors are considered control factors in this case. Figure 44 shows the combinations of this 27 run design. The study only utilizes four parameters so only

four out of the thirteen columns are needed. Careful consideration is given in this case on the column selection of each parameter. Due to the nature of fractional factorial designs such as Taguchi designs, the effects of parameters and parameter interactions may be confounded with each other. Furthermore, certain columns can be used to represent parameter interactions, but it is important to understand which columns relate to which parameters. Figure 45 is a linear graph that helps visualize the column placements for parameters and parameter interactions. The numbers in the linear graph represent columns of the L_{27} array. Each circle represents a parameter, while lines represent interactions between parameters (circles). The numbers labeled on each circle or line signifies the columns that correspond to those parameters or interactions. Since only four parameters are used in this characterization study, they are placed in columns 1, 2, 5, and 9. With this approach, the interactions can be examined between parameters in columns 1-and-2, 2-and-5, and 1-and-5. No interactions are studied with the final parameter placed in column 9. In this case the material properties, stress relief type, and busbar out of plane thickness are included in columns 1, 2, and 5. This allows the interactions between these parameters to be examined. The encapsulant out-of-plane thickness is included in column 9, therefore on the main effects of this parameter are studied. This L_{27} 3^{4-1} design is a resolution IV design. This means that all of the parameter main effects remain unconfounded by two-factor interactions. Two-factor interactions can also be estimated but they may be confounded with other two factor interactions. Higher order interactions are considered to be negligible. The run combinations for this specific study can be seen in Table 26.

$L_{27}(3^{13})$

No.	1	2	3	4	5	6	7	8	9	10	11	12	13
1	1	1	1	1	1	1	1	1	1	1	1	1	1
2	1	1	1	1	2	2	2	2	2	2	2	2	2
3	1	1	1	1	3	3	3	3	3	3	3	3	3
4	1	2	2	2	1	1	1	2	2	2	3	3	3
5	1	2	2	2	2	2	2	3	3	3	1	1	1
6	1	2	2	2	3	3	3	1	1	1	2	2	2
7	1	3	3	3	1	1	1	3	3	3	2	2	2
8	1	3	3	3	2	2	2	1	1	1	3	3	3
9	1	3	3	3	3	3	3	2	2	2	1	1	1
10	2	1	2	3	1	2	3	1	2	3	1	2	3
11	2	1	2	3	2	3	1	2	3	1	2	3	1
12	2	1	2	3	3	1	2	3	1	2	3	1	2
13	2	2	3	1	1	2	3	2	3	1	3	1	2
14	2	2	3	1	2	3	1	3	1	2	1	2	3
15	2	2	3	1	3	1	2	1	2	3	2	3	1
16	2	3	1	2	1	2	3	3	1	2	2	3	1
17	2	3	1	2	2	3	1	1	2	3	3	1	2
18	2	3	1	2	3	1	2	2	3	1	1	2	3
19	3	1	3	2	1	3	2	1	3	2	1	3	2
20	3	1	3	2	2	1	3	2	1	3	2	1	3
21	3	1	3	2	3	2	1	3	2	1	3	2	1
22	3	2	1	3	1	3	2	2	1	3	3	2	1
23	3	2	1	3	2	1	3	3	2	1	1	3	2
24	3	2	1	3	3	2	1	1	3	2	2	1	3
25	3	3	2	1	1	3	2	3	2	1	2	1	3
26	3	3	2	1	2	1	3	1	3	2	3	2	1
27	3	3	2	1	3	2	1	2	1	3	1	3	2
	a	b	a	a	c	a	a	b	a	a	b	a	a
			b	b^2		c	c^2	c	b	b^2	c^2	b^2	b
									c	c^2		c	c^2
	1	2			3								

Figure 44. Taguchi L_{27} orthogonal array

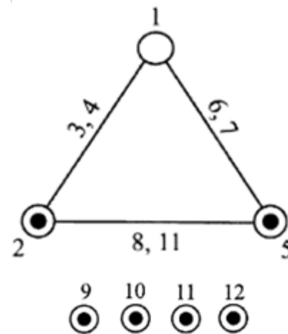

Figure 45. Taguchi L_{27} linear graph

Table 26. L_{27} Taguchi characterization design

	Column 1	Column 2	Column 9	Column 10
	A	B	C	D
Run	Material Properties	Stress Relief Type	Busbar Thickness (mm)	Encapsulant Thickness (mm)
1	Silicone	Flat	5.3	8.25
2	Silicone	Flat	5.9625	9.625
3	Silicone	Flat	6.625	11.0
4	Silicone	GW_{LOW}	5.9625	9.625
5	Silicone	GW_{LOW}	6.625	11.0
6	Silicone	GW_{LOW}	5.3	8.25
7	Silicone	GW_{HIGH}	6.625	11.0
8	Silicone	GW_{HIGH}	5.3	8.25
9	Silicone	GW_{HIGH}	5.9625	9.625
10	Epoxy	Flat	5.9625	11.0
11	Epoxy	Flat	6.625	8.25
12	Epoxy	Flat	5.3	9.625
13	Epoxy	GW_{LOW}	6.625	8.25
14	Epoxy	GW_{LOW}	5.3	9.625
15	Epoxy	GW_{LOW}	5.9625	11.0
16	Epoxy	GW_{HIGH}	5.3	9.625
17	Epoxy	GW_{HIGH}	5.9625	11.0
18	Epoxy	GW_{HIGH}	6.625	8.25
19	Stiff Epoxy	Flat	6.625	9.625
20	Stiff Epoxy	Flat	5.3	11.0
21	Stiff Epoxy	Flat	5.9625	8.25
22	Stiff Epoxy	GW_{LOW}	5.3	11.0
23	Stiff Epoxy	GW_{LOW}	5.9625	8.25
24	Stiff Epoxy	GW_{LOW}	6.625	9.625
25	Stiff Epoxy	GW_{HIGH}	5.9625	8.25
26	Stiff Epoxy	GW_{HIGH}	6.625	9.625
27	Stiff Epoxy	GW_{HIGH}	5.3	11.0

3.5 Characterization Study - Results and Discussion

This section contains the result and discussion of the L_{27} characterization study. The total equivalent strain is used as a comparison metric across all locations and for all runs of the fractional-factorial design. The same four locations in the assembly from the previous chapter are used to measure and compare the parameters of interest in this study. Please refer to Figure 29 for these locations.

3.5.1 Characterization study - equivalent strain results

Table 27 contains the volume weighted average total equivalent strain values. For this analysis, the main effects and parameter interactions are calculated for each individual location as well as the maximum value regardless of location. This is done for two primary reasons. The first is that it allows for a comparison between individual locations within the assembly as well as the maximum value regardless of location. The second is that assembly designs are sometimes concerned with specific failure sites or failure modes, either based on experimental results, previous finite element analysis or actual failure modes seen from environmental use. For these reasons it is useful to analyze the influence of the four parameters on the individual locations as well the overall maximum. Values are measured in the same four locations as those used in the screening study. Please refer to Figure 29 for those four locations. The same volume weighted averaging scheme is used for all output values.

Table 27. Equivalent total strain values for the characterization study at locations of interest

	PEMAG + ε_{el} Equivalent (with element averaging)				
	Lead at EMC Package	Lead Adjacent to Weld Region	Busbar Adjacent to Weld Region	Lead Bend	Max Regardless of Location
1	4.93E-04	4.35E-04	8.65E-05	4.82E-04	4.93E-04
2	7.39E-04	6.98E-04	9.85E-05	7.35E-04	7.39E-04
3	9.60E-04	9.08E-04	2.57E-04	9.59E-04	9.60E-04
4	2.31E-03	1.03E-03	2.57E-04	2.52E-03	2.52E-03
5	2.69E-03	1.24E-03	2.55E-04	3.26E-03	3.26E-03
6	2.87E-03	1.47E-03	2.33E-04	2.87E-03	2.87E-03
7	4.81E-03	1.06E-03	3.10E-04	8.36E-03	8.36E-03
8	4.82E-03	1.24E-03	2.77E-04	6.44E-03	6.44E-03
9	5.33E-03	1.52E-03	2.76E-04	7.82E-03	7.82E-03
10	3.18E-02	2.20E-02	1.75E-02	2.46E-02	3.18E-02
11	3.40E-02	2.48E-02	1.74E-02	2.73E-02	3.40E-02
12	3.10E-02	1.96E-02	1.17E-02	2.35E-02	3.10E-02
13	3.25E-02	2.32E-02	1.75E-02	2.64E-02	3.25E-02
14	2.94E-02	1.87E-02	1.19E-02	2.28E-02	2.94E-02
15	3.18E-02	2.17E-02	1.22E-02	2.58E-02	3.18E-02
16	2.97E-02	1.66E-02	1.21E-02	2.36E-02	2.97E-02
17	3.23E-02	1.93E-02	1.20E-02	2.67E-02	3.23E-02
18	3.52E-02	2.20E-02	1.20E-02	2.96E-02	3.52E-02
19	1.53E-03	1.56E-03	1.02E-03	1.56E-03	1.56E-03
20	1.35E-03	1.39E-03	5.96E-04	1.38E-03	1.39E-03
21	1.81E-03	1.86E-03	6.55E-04	1.84E-03	1.86E-03
22	1.21E-03	1.18E-03	6.95E-04	1.27E-03	1.27E-03
23	1.67E-03	1.61E-03	7.47E-04	1.73E-03	1.73E-03
24	2.18E-03	2.13E-03	7.80E-04	2.27E-03	2.27E-03
25	1.66E-03	1.33E-03	8.06E-04	1.66E-03	1.66E-03
26	2.20E-03	1.76E-03	8.32E-04	2.21E-03	2.21E-03
27	1.71E-03	1.55E-03	4.49E-04	1.71E-03	1.71E-03

Looking at Table 27, The overall minimum of 8.65E-05 occurs in the first run in the busbar adjacent to the weld, while the overall maximum of 3.52E-02 occurs in lead adjacent to the EMC in run 18. This is almost a three order of magnitude difference. There are also several runs that contain unrealistically large total equivalent strain values. This occurs in runs 10 through 18, with total equivalent percent strain values

ranging from 2.94 to 3.52. In this case response surface models are helpful to avoid combinations where such large strain values occur. For almost all the runs the maximum occurs in either the lead adjacent to the EMC package or in the lead bending. Conversely, the minimum total equivalent strains occur in the busbar adjacent to the weld in all 27 runs.

Figure 46 contains plots of the main effects and parameter interactions of the means. In this case the output variable of interest is the maximum total equivalent strain value regardless of location. Figure 46a contains plots of the main effects while Figure 46b contains plots of the select parameter interactions studied based on the linear graph in Figure 45. The main effects plot shows that the encapsulant material property, Factor A, is the most influential as compared to the other parameters. Furthermore, this plot also indicates a highly nonlinear non-monotonic trend where the maximum occurs at the level two of the factor. This is at the material property set of E=2GPa and CTE=55ppm/^{o}C.

The interaction plots also show very little interaction and once again the non-linear effects are seen in the interaction terms containing the encapsulant material property (interactions AB and AC). Similar plots are provided in Appendix F for the total equivalent strains values at each individual location. Interestingly, the same trends are observed for each individual location. However, in this case the amount of non-linearity differs from the location to location. The four locations differ as follows (from most to least non-linear): the lad adjacent to the EMC, the lead bend, the lead adjacent to weld region, and the busbar adjacent to weld region. Additionally the

main effects of the other three parameters vary slightly in shape and influence from location to location, but they are all still very small when compared to the non-linear effects of the encapsulant material property. The interaction plots show very similar overall trends as well with different magnitudes. There are some minor crossovers observed however there is not considerable interaction between terms.

The non-linear influence seen from the encapsulant material property is in reasonable agreement with results from the design space study in the previous chapter. The three levels of encapsulant selected for this study go across a specific diagonal of the encapsulant material property design space from the previous chapter (see Figure 42). This diagonal goes from a high modulus and low CTE to a low modulus and high CTE. Looking along this diagonal across the response surface models generated in the previous chapter, the largest strain values tended to occur in the midpoint. This agrees with the results of the characterization study and indicates that there is also considerable interaction between the modulus and CTE.

Table 28. Parameter factors for characterization study

Factor	A	B	C	D
Parameter	Encapsulant Material Property	Stress Relief Type	Busbar Out-of-Plane Thickness	Encapsulant Out-of-Plane Thickness

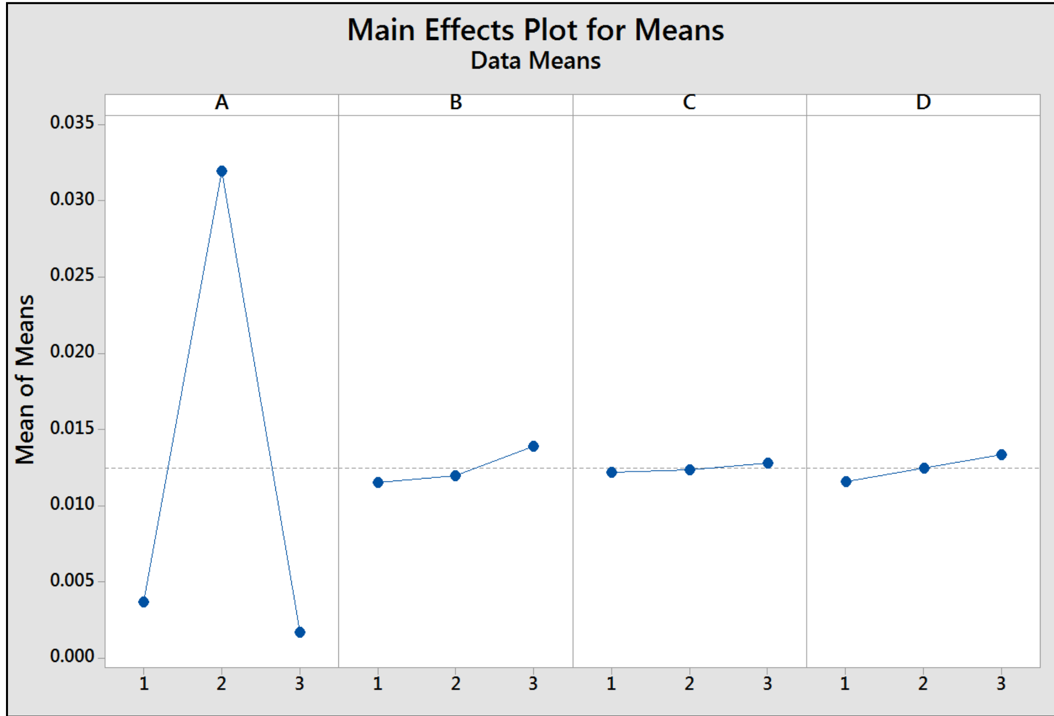

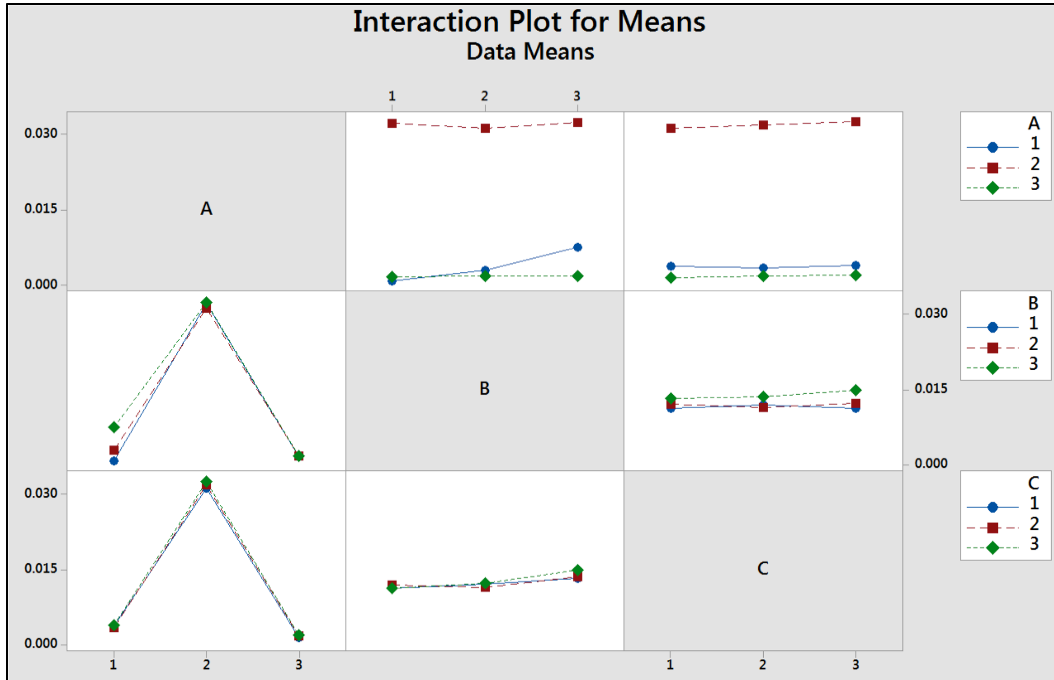

Figure 46. Maximum total equivalent strain regardless of location: (top) parameter main effect plots for means (b) parameter interaction plots

Table 29. Response table for main effect means and parameter rankings

Level	A	B	C	D
1	0.003718	0.011534	0.012207	0.011586
2	0.031967	0.011958	0.012385	0.01247
3	0.00174	0.013933	0.012832	0.013369
Delta	0.030227	0.0024	0.000625	0.001783
Rank	1	2	4	3

Table 29 provides a range of the effect for each parameter as well as ranking of all the parameters relative to one another. The ranking is as follows from most to least influential: material properties (factor A), stress relief type (factor B), busbar out-of-plane thickness (factor C), and encapsulant out-of-plane thickness (factor D).

Table 30. Anova for L_{27} screening study

Source	DF	Seq SS	Adj SS	Adj MS	F	P
A	2	0.005147	0.005147	0.002573	2657.75	0.000
B	2	0.00003	0.00003	0.000015	15.25	0.004
C	2	0.000002	0.000002	0.000001	0.96	0.433
D	2	0.000014	0.000014	0.000007	7.39	0.024
A*B	4	0.000046	0.000046	0.000011	11.8	0.005
A*C	4	0.000001	0.000001	0	0.36	0.828
B*C	4	0.000005	0.000005	0.000001	1.3	0.369
Residual Error	6	0.000006	0.000006	0.000001		
Total	26	0.00525				

Table 30 contains an ANOVA analysis of the results of the study. Minitab shows the resulting P-value for the encapsulant material property to be zero. This is not the case, rather it is significantly smaller than any of the other values. This is confirmed by observing how much larger the F-value is when compared to the F-value of other parameters. Other parameters such as the stress relief type (factor B), the encapsulant out-of-plane thickness (D), and the interaction of the encapsulant material property

and stress relief (interaction A*B) are shown to be significant according to the results of the ANOVA. However, they are considerably less significant than the encapsulant material property (factor A).

Table 31 contains the coefficients of a linear model fit. Main effects and parameter interaction terms are included in the fit. This allows for a rough estimation of the maximum total equivalent strain value at any combination of the parameters in the screening study. An R^2 value of 0.999 indicates a good fit.

Table 31. Linear model fit to main effect means terms for characterization study

Term	**Coefficient**
Constant	0.012475
A 1	-0.008757
A 2	0.019492
B 1	-0.000941
B 2	-0.000517
C 1	-0.000268
C 2	-0.000089
D 1	-0.000889
D 1	-0.000005
A*B 1 1	-0.002046
A*B 1 2	-0.000318
A*B 2 1	0.001241
A*B 2 2	-0.000216
A*C 1 1	0.000341
A*C 1 2	-0.000149
A*C 2 1	-0.000365
A*C 2 2	0.000023
B*C 1 1	0.000019
B*C 1 2	0.000599
B*C 2 1	0.000407
B*C 2 2	-0.000405
R^2 = 99.9%, R^2(adj.) = 99.5%	

Figure 47 contains analysis of the regular residuals from this analysis. This is the difference between the values observed and those predicted by the model. The residual probability plot in the top left corner as well as the residual versus frequency histogram in the bottom left corner of Figure 47 indicate that the residuals follow a fairly normal distribution. The fitted value versus the residual (top right of Figure 47) shows the disparity in fitted values from the non-linear effects, but the even distribution above and below the zero line also indicates that the residuals follow a normal distribution. This is a positive indication of goodness of the model fit.

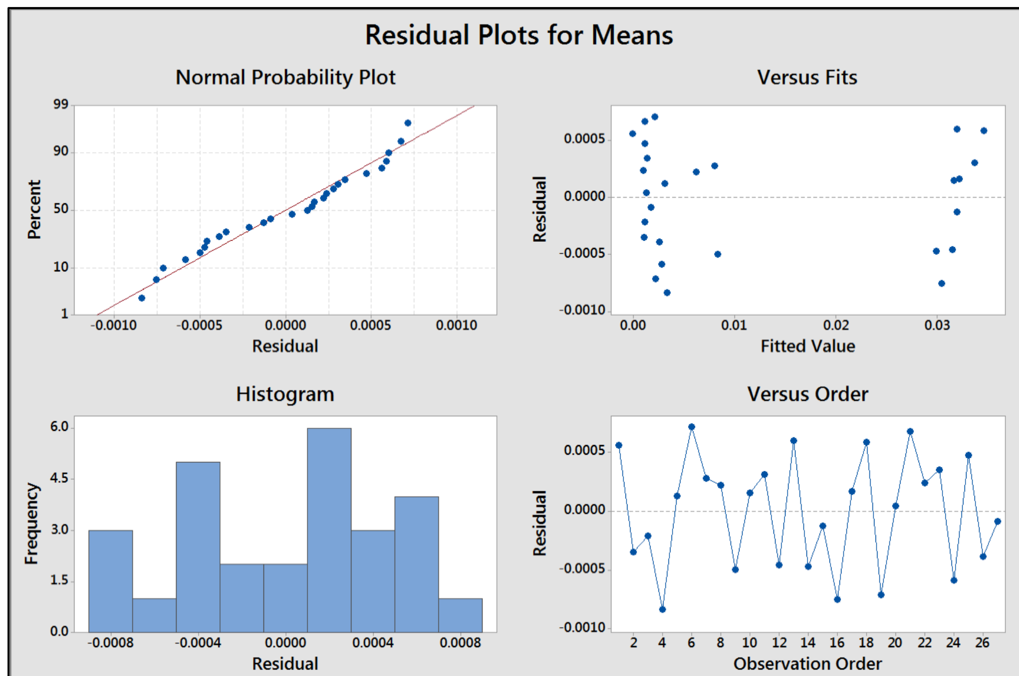

Figure 47. Plots of the residual means of model fit for characterization study

Chapter 4: Summary and General Conclusions

In this thesis, parametric studies are conducted, using 2D finite element models, to examine the effects of different design parameters on the stresses and deformation of an encapsulated assembly under thermal loading. The assembly considered is a COTS beam lead component that is welded to slender busbars and encapsulated in a single polymeric encapsulant.

Two main studies are conducted. In the first study, a two-dimensional design space is constructed to parametrically vary the temperature-dependent Young's modulus and CTE values of the encapsulant. For this study, only the encapsulant's material properties are varied while all other design parameters are held constant. The design space is selected to bound the material properties of different encapsulants used for such applications. The assembly is subjected to a thermal ramp loading profile, in order to understand the physics behind the problem statement. The axial forces, bending moments, and total equivalent strain values are output at multiple potential failure sites. Response surface models are generated for each metric at each location of interest. Some response surface models showed expected or monotonic trends. This included the axial forces adjacent to the weld, the peel force in the weld, and the total equivalent strain values in multiple locations in the assembly. For these parameters, a fair amount of parameter interaction was observed between the Young's modulus and CTE values. In all of these cases the maximum values were observed to occur at the largest combination of Young's modulus and CTE values. Some non-monotonic behavior was observed in the response surfaces, such as the axial force measured in the component lead adjacent to the component EMC and the shear force

measure in the weld. Expanded investigations are conducted to try and understand these phenomena.

In the second study, a two-step Taguchi DOE approach is used to understand the influence of multiple design parameters on the stresses and deformation of the encapsulated assembly. For both steps the total equivalent stain, calculated at multiple locations, was used as the metric of interest. In this case the assembly is subjected to an accelerated thermal cycle loading profile. The varied parameters are expanded beyond just the encapsulant material properties to include other features such as the lead geometry and dimensions, busbar dimensions, and encapsulant dimensions. For this study, the selected encapsulant properties are based on the results of the previous study as well as the values in the literature. An initial screening study is run to narrow the list of influential parameters. Seven two-level parameters are used in this initial screening study. Only the main effects are considered in this initial screening study. The four most influential parameters – the encapsulant material properties, the component lead stress relief geometry, the busbar out-of-plane thickness, and the encapsulant out-of-plane thickness are selected for a more detailed characterization study. Main effect plots, ANOVA table, and linear model coefficients are provided for this screening study. The characterization study is an expanded 27 run study that increases each parameter to three levels to provide more granularity and to capture any nonlinear non-monotonic effects of the various parameters. The expanded third level is selected to be in between the two levels of the screening study. The results of this study showed that the encapsulant was both the most influential parameter and had highly non-linear effects. The middle set of encapsulant properties was shown to

provide the harshest condition. This is confirmed by the trends observed in the initial design space study.

In some cases, for both studies, the measured strain values are unrealistically large. Fitting models or developing response surface models in these studies allows the designer to identify the regions of the design space or combinations of parameters to avoid.

Chapter 5: Thesis Contributions

The contributions of this paper will be provided in an itemized list for each study.

5.1 Parametric study – Effects of encapsulant properties on a welded beam lead SMT component under thermal cycling using Finite Element Analysis

- This study provides general insight towards the design of a welded and encapsulated component in a large and thin laminate form factor. Specifically, this study explores the influence of the encapsulant's stiffness and CTE values. Relative trends observed in the response surface approach provide helpful insights towards design and inputs to the second study. The design space approach for this uncommon assembly provides rapid relative comparisons between potential designs.
- This study focuses on a fairly uncommon encapsulated assembly, which consists of a welded component encapsulant in a large laminate structure. This study provides response surface models for the forces, bending moments, and total equivalent strains values for this uncommon assembly.
- This study highlights that complex and encapsulated heterogeneous assemblies, such as this one, often have non-trivial stress and deformations states. These studies are aimed at understanding the non-trivial results of the response surface models.

5.2 Design optimization of an encapsulated beam-lead component using a combined FEM and DOE approach

- This study helps provide insight towards general design considerations for this type of large laminated assembly. The relative influence of multiple design

parameters such as the encapsulant properties, component geometry and dimensions, and interconnect dimensions are provided.

- The study highlights that in some cases there are non-linear effects and that the design can be dominated by a single parameter. In this case the encapsulant's material properties had the largest and most non-linear effect on the total equivalent strain values measured at multiple locations within the assembly.
- This study uses a Taguchi DOE approach to identify the influential design parameters. Response surface models are generated for the DOE results and the model coefficients are provided.

Chapter 6: Limitations and Future Work

There are several limitations to the work presented in this study. First, the encapsulant in this study is modeled with temperature dependent elastic properties. Many polymeric materials used for similar applications are known to have both temperature and time dependent properties and are modeled as viscoelastic. This is typically done using a combination of a prony series (derived from creep or relaxation tests) and a time-temperature superposition model. This would also allow for a slightly adjusted thermal loading profile, allowing for specific dwell times and ramp rates. While this would provide higher fidelity to the model, it may be both inefficient and costly to use such an approach for a design space methodology. Furthermore, this approach adds to the complexity of how the design space would be constructed, since the parameters of the prony series and time-temperature superposition model could not simply be parametrically varied. If this type of study were to be used for a rapid comparison during the design stage product development cycle, characterizing the viscoelastic properties of a large quantity of encapsulants many not even be feasible.

The second limitation relates to the validation of the FEA models. There is no direct experimental work used to validate the models in this study. Some of the work in this study is based on the modeling and experimental work of a more complex but very similar composite laminate assembly. However, no experimental work is conducted explicitly for this particular assembly. Since this is a generalized FEA parametric study, material properties are also taken from this similar study and from the literature. Experimental tests of this assembly subjected to thermal ramp loading and thermal cycling would allow for better calibration of the model. However, similar to

the viscoelasticity limitation, such a calibration may not be feasible to do over the entire design space. Instead, it may only be practical to calibrate the model with a select few encpasulants and diode-region geometries. Future work could be conducted to characterize some of these materials and perform experimental tests to calibrate the FEA models.

The last main limitation relates to the use of 2D finite element models. For this study, 2D generalized plane strain models are used to best mimic a three-dimensional representation of the assembly. However, it is well known that 2D models do not always adequately approximate the stress and deformation states of the loaded assembly. This can lead to either over or under predicting results. For this specific assembly, the primary concern is that the 2D model may not sufficiently capture the out-of-plane deformation and stresses. Additionally, no section overlay is used in the 2D model over the diode or busbars. This does not fully capture how the encapsulant encloses the busbar and diode regions. For these parametric studies, selecting 2D models is a matter of limited resources. While it may not be cost-effective to run the parametric studies with three-dimensional models, a good approach could be to utilize a 2D-to-3D transfer function. Future work could be done to generate this transfer function, at least for the design space study, using a reduced number of runs for the three-dimensional model. Furthermore, the nature of the parametric studies provide comparisons on a relative basis. This means that the absolute values of the study may present less critical information when compared the to overall trends observed in the studies. In this sense, some of the potential inaccuracies associated with 2D models may be mitigated.

Appendices

Appendix A-1. SBR diode technical drawing [44]

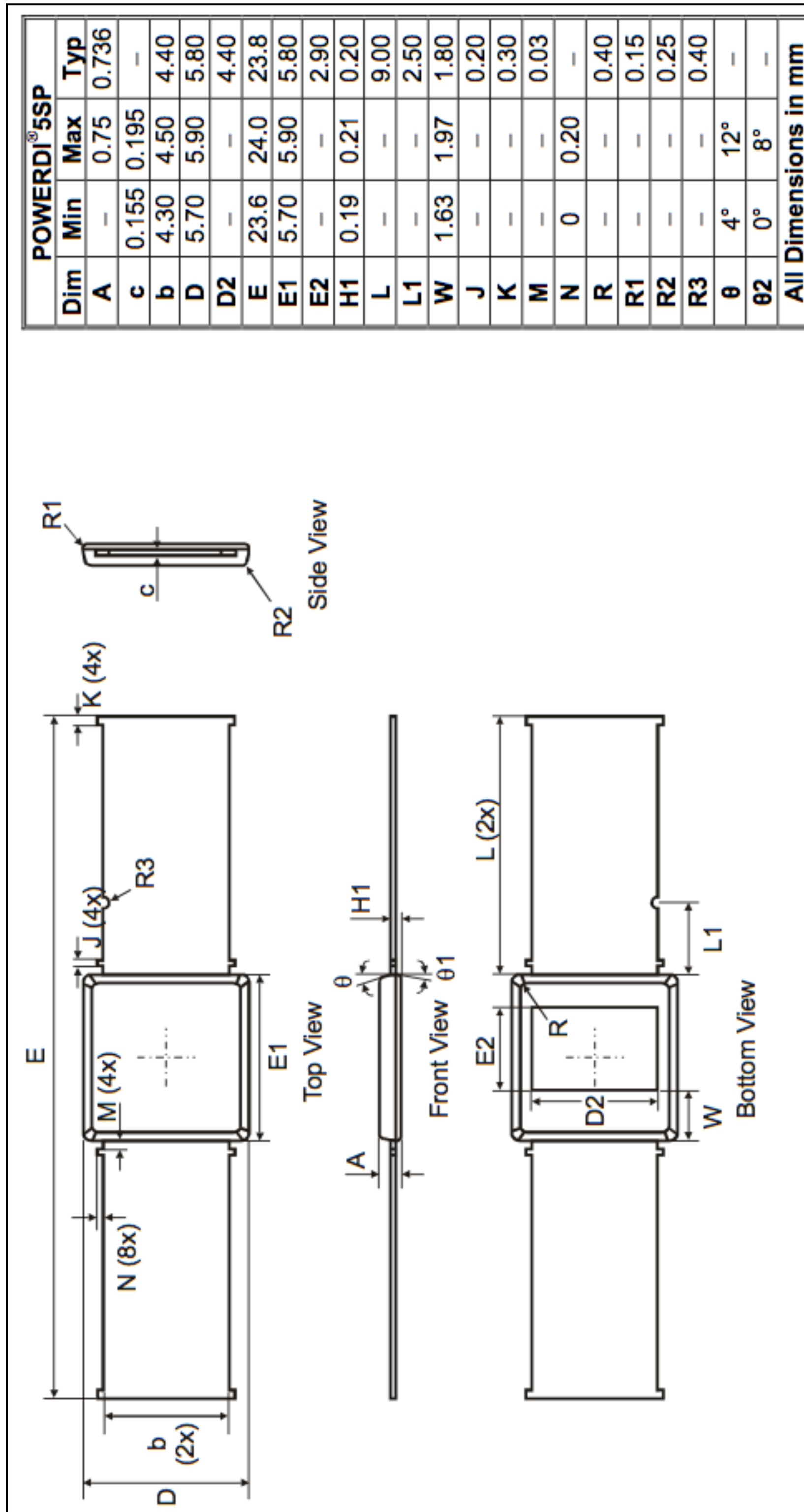

POWERDI® 5SP			
Dim	Min	Max	Typ
A	–	0.75	0.736
c	0.155	0.195	–
b	4.30	4.50	4.40
D	5.70	5.90	5.80
D2	–	–	4.40
E	23.6	24.0	23.8
E1	5.70	5.90	5.80
E2	–	–	2.90
H1	0.19	0.21	0.20
L	–	–	9.00
L1	–	–	2.50
W	1.63	1.97	1.80
J	–	–	0.20
K	–	–	0.30
M	–	–	0.03
N	0	0.20	–
R	–	–	0.40
R1	–	–	0.15
R2	–	–	0.25
R3	–	–	0.40
θ	4°	12°	–
θ2	0°	8°	–
All Dimensions in mm			

Appendix B-1. Encapsulant material properties
(Electronic Packaging - Harper 2000)

TABLE 3.4 Mechanical Strength Properties of Common Electronic Packaging Materials

Material	Young's Modulus (GPa)	Yield Stress (MPa)	Tensile Strength (MPa)
Organic Materials			
Epoxy	3.1		69
Polyimide	4.2	105	65
Epoxy-glass	17		276
Polyaramid (Kevlar®)	59–124		2760
Polycarbonate	2.3–2.4		55–75
Polyurethanes			1.4–5.5
Silicones (RTV)	0.06–2.2		6.5–10.3
Polyether ether ketone (PEEK)	3.7–4.0		7–100
Polymethyl methancrylate (PMMA)	2.4–3.3		80

TABLE 1.1 Properties of Thermosetting Plastics

		Epoxy		Phenolics		
	DAP (GDI-30)	Glass-filled	Mineral-filled	General-purpose	Glass-filled	Mineral-filled
Dielectric constant, D-150, 60 Hz	4.2	5.0	4.0	12.0	50.0	6.0
10^6 Hz	3.5	4.6	5.0	6.0	10.0	6.0
Dissipation factor, D-150, 60 Hz	0.004	0.01	0.01	0.3	0.3	0.07
10^6 Hz	0.01	0.01	0.01	0.7	0.8	0.10
Dielectric strength, D-149; V/mil	400	360	400	400	350	400
Volume resistivity, D-257; Ω · cm	10^{13}	3.8×10^{15}	9×10^{15}	10^{13}	10^{13}	10^{14}
Arc resistance, D-495; seconds	140	140	180	50	70	180
Specific gravity, D-792	1.7	1.8	2.1	1.45	1.95	1.83
Water absorption, D-570; % 24 h	<0.2	0.2	0.04	0.7	0.5	0.5
Heat deflection temperature, D-648; at 264 lb/in², °F	500	400	250	340	400	500
Tensile strength, D-638; lb/in²	10,000	30,000	15,000	10,000	7000	11,000
Impact strength (Izod), D-256; ft · lb/in	5.0	10	0.4	0.3	3.5	15.0
Coefficient of thermal expansion, D-696; 10^{-5}/°F	2.6	1.7	2.2	2.5	—	0.88
Thermal conductivity, C-177; Btu · in/(h · in · ft² · °F)		6	—	0.3	0.34	0.2

TABLE 1.1 Properties of Thermosetting Plastics (*Continued*)

	Alkyds		Polyester			
	MAG	MAI-60	GPO-3	Polyimide	Polyurethane	Mineral-filled silicone
Dielectric constant, D-150, 60 Hz	6.3	5.6	4.5	3.5	6	3.6
10^6 Hz	4.7	4.6	—	3.4	3	3.7
Dissipation factor, D-150, 60 Hz	0.04	0.10	0.05	0.0025	0.1	0.005
10^6 Hz	0.02	0.02	—	0.01	0.04	0.003
Dielectric strength, D-149; V/mil	400	375	300	6500	500	425
Volume resistivity, D-257; Ω · cm	10^{14}	10^{13}	—	10^{18}	10^{14}	10^{15}
Arc resistance, D-495; seconds	>180	180	>180	230	120	240
Specific gravity, D-792	2.24	2.07	1.95	1.4	1.1	2.05
Water absorption, D-570; % 24 h	0.08	0.07	0.5	2.9	0.2	0.15
Heat deflection temperature, D-648; at 264 lb/in², °F	350	>400	—	680	190	>500
Tensile strength, D-638; lb/in²	3000	6000	9000	17,000	1000	6500
Impact strength (Izod), D-256; ft · lb/in	0.3	9.5	8.0	1.5	25	0.5
Coefficient of thermal expansion, D-696; 10^{-5}/°F	3	2	2	2.8	25	2.8
Thermal conductivity, C-177; Btu · in/(h · in · ft² · °F)	7.2	3.6	4	6.8	0.1	3.1

Appendix B-2. Encapsulant material properties
(Electronic Packaging Materials and Their Properties (Pecht et al 1999)

Table 36 Physical properties of typical resin systems (Harper 1991, Mumby 1989a)

Resin System	Temperature Tg (°C)	Elastic Modulus (GPa)	Poisson's Ratio	CTE (ppm/°C)	Thermal Conductivity (W/m°C)	Dielectric Constant @ 23°C, 1MHz	Loss Tangent @ 23°C, 1MHz
Epoxy	120-140	3.45	0.37	69	0.19	3.6	0.032
Polyimide	240-300	2.8	0.33	50	0.18	3.2	0.020
Cyanate Ester	260	2.6	-	55	0.20	3.1	0.005
PTFE	-	0.35	0.46	99	0.19	2.0	0.0002
BT	250	-	-	-	0.20	3.1	0.003

Table 37. Mechanical and electrical properties of selected epoxy resins (Clayton 1989)

Property	Anhydride	Aliphatic	Aromatic amine	Catalytic	High-temperature anhydride	Epoxy Novalac anhydride	Di-anhydride
Resin / Curing agent	DGEBA/ HHPA	DGEBA/ DETA	DGEBA/ MPDA	DGEBA/ BF3MEA	DGEBA/ NMA	NOVOLAC/ NMA	DGEBA/ PMDA
Heat deflection temperature(°C)	130	125	150	174	170	195	280
Tensile strength (MPa), @ 23°C	72	75	85	43	75	66	22
Tensile modulus (GPa), @ 23°C	2.80	2.87	3.30	2.70	3.40	2.94	2.70
Tensile strength (MPa), @ 100°C	37	32	45	29	46		14[b]
Tensile modulus (GPa), @ 100°C	2.10	1.80	2.20	1.90	1.40		
Flexural strength (MPa), @ 23°C	126	103	131	112	112	147	59
Flexural modulus (GPa), @ 23°C	3.22	2.48	2.80		4.80	3.69	3.61
Compressive strength (MPa), @ 23°C	111	224	234		116	159	254
Compressive modulus (GPa), @ 23°C	5.09	1.86	2.31		0.73	2.22	2.41
Volumetric resistivity (Ω-cm), @ 23°C	4e14	2e16	1e16		2e14	1e16	
Dielectric constant, @ 23°C and 1 MHz	3.2	3.33	3.85	3.20	2.99	3.20	3.34
Dissipation factor, @ 23°C and 1 MHz	0.013	0.034	0.038	0.024	0.021	0.016	0.022

NB.: HHPA, hexahydrophthalic anhydride; DETA, diethylenetriamine; BF3 MEA, boron trifloride monoethylamine complex; NMA, nadic methyl anhydride; PMDA, pyromellitic dianhydride; BDMA, benzyldimethylamine *b:* Measured @ 150°C.

Appendix B-3. Encapsulant material properties
(Materials for Electronic Packaging - Chung 1995)

Table 12.1 Modulus and coefficient of thermal expansion (CTE) for some potential encapsulants.

Encapsulants	*CTE* ($10^{-6}\,°C^{-1}$)	*Modulus (psi)*
Epoxy	40–80	$1\text{–}5 \times 10^6$
Polyimide	3–80	1×10^6
Parylene	35–40	0.4×10^6
Silicone–polyimide	5–100	0.4×10^6
Silicone gel	200–1 000	0–400

Table 12.2 Overview of potential encapsulants.

Encapsulants	*Application*	*Advantages*	*Disadvantages*
Epoxies	Normal dispensing or molding	Good solvent resistance Excellent mechanical strength	Not repairable High stress Marginal electrical performance
Polyimides	Normal dispensing (spin coat)	Good solvent resistance Thermally stable (~500°C)	Not repairable High stress
Polyxylylene (Parylene, Union Carbide)	Thermal deposition (reactor)	Good solvent resistance Conformal coating	Thin film only Not repairable
Silicone–polyimide	Normal dispensing	Less stress than polyimide Better solvent resistance than silicone	Higher CTE than polyimides Thin film only
Silicone (RTV gel)	Normal dispensing	Good temperature cycling Good electrical properties Very low modulus	Poor solvent resistance Low mechanical strength

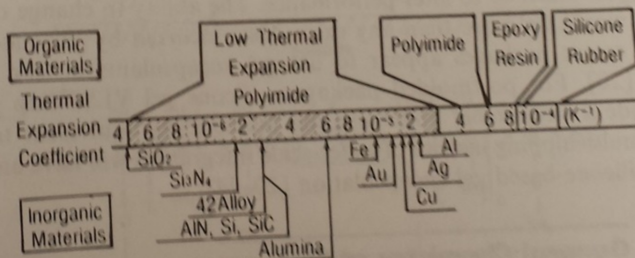

Figure 12.2 Thermal expansion coefficients of various materials used in IC fabrication.

Appendix B-4. Encapsulant material properties
(Electronic Packaging - Lau et al 1998)

TABLE 5.2 Typica

	Thermal	Physical[h]						
	Safe use temp. (°C)	Linear expansion × 10⁵/°C	Ultimate tensile strength (kpsi)	Ultimate tensile strength (MPa)	Ultimate elongation (%)	Hardness[g]	Relative adhesion[c]	General comments
Thermoplastics								
Asphalt and tars[k]	70	8	0.6	4	5	SD 60	4	Lowest cost
Fluorocarbon	260	5.5	3	20	200	SD 60	none	Good solvent resistance
Polyethylene[k]	115	9.5	4.4	30	1000	SD 65	5	Flexible
Polystyrene[k]	85	4	7.3	50	1.5	M 80	4	Rigid
Polyvinyl chloride	100	3	3	20	100	SD 80	3	Costing material
Wax[k]	55	11	0.3	2	5	SD 30	4	Melt, pour, and chill
Silicone-polyimide[a]	400	3–10	2	14	200	—	1	Good solv. resist. high temp.
Parylene[d]	120	3.5–4.0	10.2	70	200	—	4	Conformal costing
Polyketone	260	5.7	13.8	95	150	—	2	High temperature Crystalline material
Polyetherketone	—	4.4	15.2	105	50	M 105	2	High temperature Crystalline material
Polyetheretherketone	250	4.7	14.5	100	5	M 99	2	High temperature Crystalline material
Polyaryletherketone	250	4.0	10	69	5	M 86	2	High temperature Crystalline material
Polysulfone[i]	200	3.0	12.2	84	6	M 69	2	High temperature Crystalline material
Polyethersulfone[i]	235	3.0	13	89	7	M 88	2	High temperature Crystalline material
Liquid crystal polymers	180–240	0–2.5	20.3–34.8	140–240	1–7	M 60–M 100	2	High performance materials
Thermosets								
Alkyd[k]	120	4	8	55		SD 90	2	
Allylester[k]	100	4	5.8	40		M 70	3	
Butadiene styrene[k]	245	5	4.4	30	4	SD 80	4	
Epoxode[k]	230	4–8	10.2	70	<1	M 90	1	Excellent solvent resistance
Phenolaldehyde[k]	80	4	7.3	50	1.5	M 126	2	
Polyester[k]	165	6	8.0	55	<5	M 100	3	
Silicones[k]	260	13–100	2.5	17	8		4	Excellent THB performance
Polyimides[e]	<430	0.3–80	14–20	100–140	10–80	—	3	Good solv. resist. h temp
Silicone-Epoxy[f]	<200	3–6	8	55		SD 60	3	Good for molding
Benzocyclobutene[e]	350(N_2)	3.4	10.3	71	<1	3H	1	High temperature
Elastomers								
Buna-S rubber	120	6	0.3	2	400	SA 50	2	Flexible
Chloro rubber	—	9	2.5	17	500	SA 70	3	Flexible
Natural rubber	65	4	3	20	700	SA 50	2	Flexible
Silicone rubber[k]	260	—	0.58	4	100	SA 60	4	Flexible
Thioplast[k]	120	10	0.3	2	400	SA 40	2	Poor elec. props h temp.
Urethane[k]	95	10	5.1	35	400	SA 60	1	Poor elec. props. temp.
Inorganics								
SiO_2	760	0.05–0.09	14–56	100–390	0		4	Excellent passiv
Si_3N_4	370–760	0.45–0.54	14–140	100–1,000	0		4	Excellent passiv
SiON	500	0.05–0.35	14–140	100–1,000	0			

[a] Ablestiks.
[b] In 24 hours, ⅛ inch

Appendix C-1. Matlab source code – bending moment sample calculation

```
%% Bending Moment (sample calculation)

x=[0 0.0453825 0.163564 0.281772 0.4]; %position values along the
cross section output by ABAQUS in displacement distribution plot

S11=[80.39656 70.095967 43.39095 13.72062 0.45485]; %S11 (axial
stress) range values along the cross section

xi=0:0.001:0.4; % Number of partitions/sections used for numerical
approximation
S_xx=interp1(x,S11,xi); % Linear interpolation between S11 values
output from ABAQUS based on number of sections for numerical
approximations

dy=0.4/length(xi); %dy is the infinitesimal length, based on the
number of rectangles used for approximation

y_NA=-1.*[-0.2:0.001:0.2]; %distance from nuetral axis (from -0.2mm
to 0.2mm)
t=5.3 % of-of-plane thickness

m=t.*(y_NA).*S_xx.*dy; %Momement section values
M_y=sum(m) %Sum of all sections equating to bending moment
approximation
```

Appendix C-2. Matlab source code – sample response surface fit code

```
function [fitresult, gof] = createFit(CTE, E, EqStr)
%CREATEFIT(CTE,E,EQSTR)
%  Create a fit.
%
%  Data for 'untitled fit 1' fit:
%      X Input : CTE
%      Y Input : E
%      Z Output: EqStr
%  Output:
%      fitresult : a fit object representing the fit.
%      gof : structure with goodness-of fit info.
%
%  See also FIT, CFIT, SFIT.

%  Auto-generated by MATLAB on 01-Jun-2014 17:39:57

%% Fit: 'Response Surface'.
E=[0.01 0.1 1 4.5 8]
CTE=[10 32.5 55 77.5 100 125 150]
Strain=[8.17E-04    1.04E-03    1.29E-03    1.54E-03    1.81E-03
        2.08E-03    2.41E-03    5.83E-04    1.43E-03    2.43E-03
        3.49E-03    4.68E-03    6.05E-03    8.02E-03    5.37E-04
        1.87E-03    5.78E-03    1.14E-02    1.71E-02    2.30E-02
        2.95E-02    6.07E-04    3.92E-03    1.05E-02    1.69E-02
        2.29E-02    2.88E-02    3.59E-02    6.46E-04    5.04E-03
        1.16E-02    1.78E-02    2.38E-02    2.99E-02    3.72E-02]

[xData, yData, zData] = prepareSurfaceData( CTE, E, EqStr );

% Set up fittype and options.
ft = 'cubicinterp';
opts = fitoptions( ft );
opts.Normalize = 'on';

% Fit model to data.
[fitresult, gof] = fit( [xData, yData], zData, ft, opts );

% Plot fit with data.
figure( 'Name', 'untitled fit 1' );
h = plot( fitresult, [xData, yData], zData );
legend( h, 'untitled fit 1', 'EqStr vs. CTE, E', 'Location',
'NorthEast' );
% Label axes
xlabel( 'CTE' );
ylabel( 'E' );
zlabel( 'EqStr' );
grid on
```

Appendix D-1. Bending moment response surface – lead adjacent to EMC

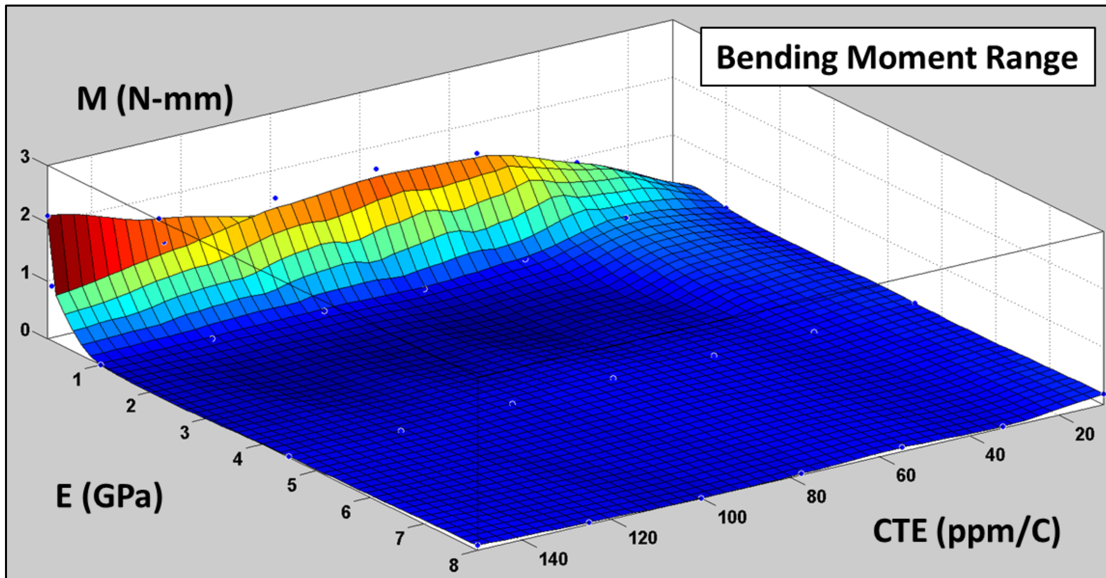

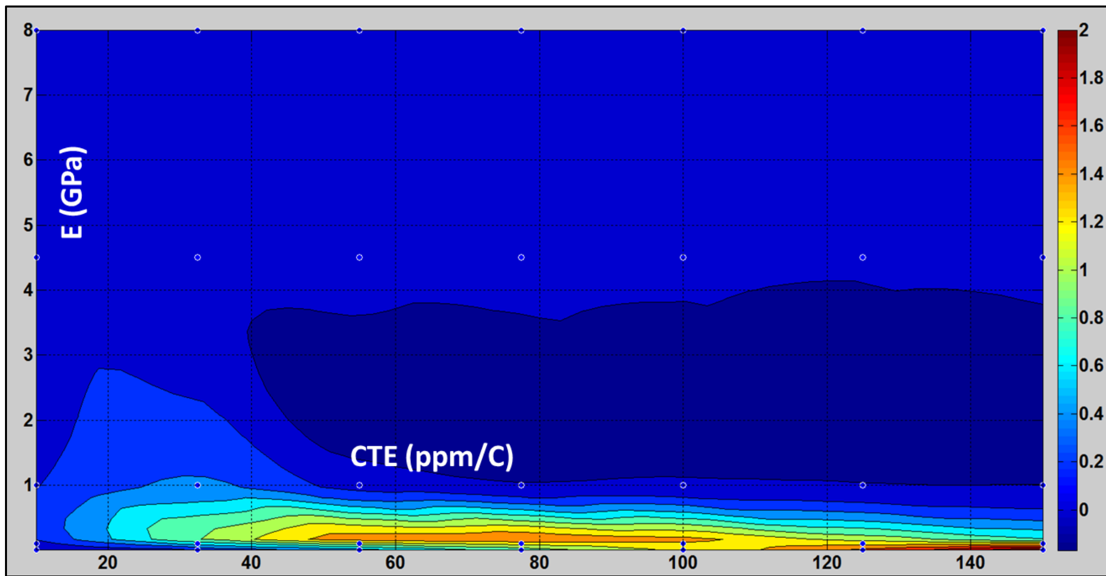

Bending Moment (N-mm)		CTE (ppm/C)						
		10	32.5	55	77.5	100	125	150
E (GPa)	0.01	1.78E-2	2.30E-1	5.36E-1	8.84E-1	1.24E+0	1.62E+0	2.12E+0
	0.1	1.63E-1	9.69E-1	1.54E+0	1.67E+0	1.57E+0	1.26E+0	9.44E-1
	1.0	1.90E-1	4.33E-1	1.20E-1	1.37E-2	3.71E-2	7.80E-3	4.06E-4
	4.5	1.51E-1	5.98E-2	5.18E-2	6.81E-2	3.27E-2	9.70E-3	2.14E-2
	8.0	1.88E-1	3.43E-2	7.38E-2	2.72E-2	1.30E-3	4.03E-2	8.89E-2

Appendix D-2. Bending moment response surface – lead adjacent to weld region

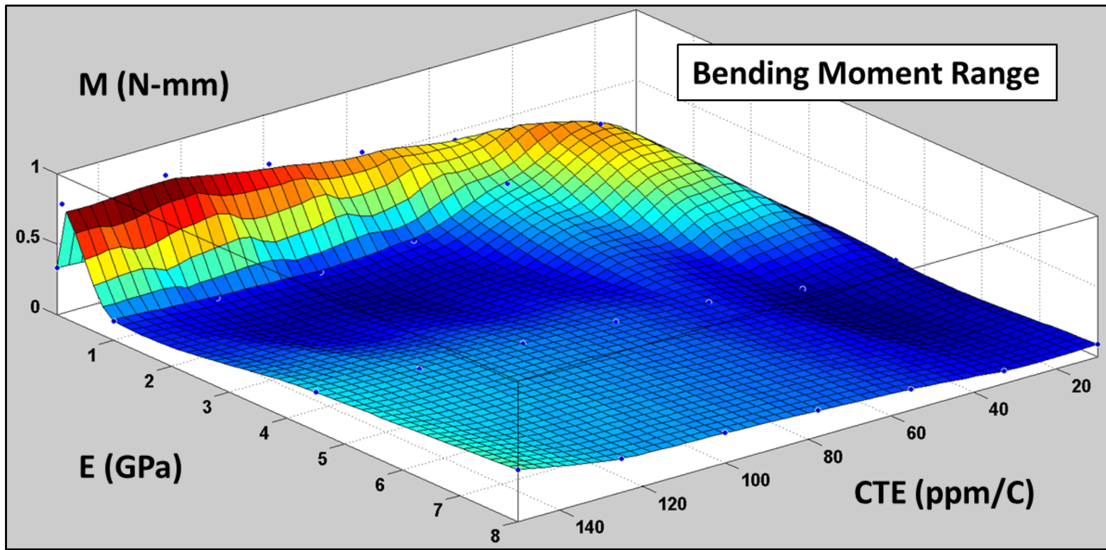

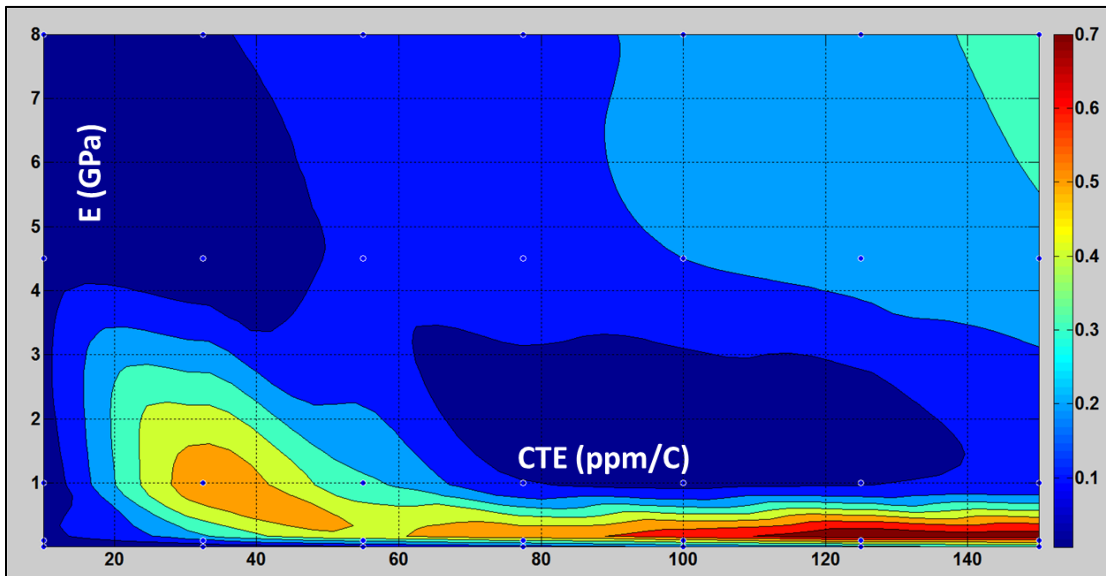

Bending Moment (N-mm)		CTE (ppm/C)						
		10	**32.5**	**55**	**77.5**	**100**	**125**	**150**
E (GPa)	**0.01**	3.47E-2	3.21E-2	9.84E-2	1.63E-1	2.21E-1	2.73E-1	3.32E-1
	0.1	5.93E-2	2.56E-1	4.62E-1	5.65E-1	6.70E-1	8.00E-1	8.02E-1
	1.0	2.41E-2	5.56E-1	3.19E-1	1.04E-1	6.58E-2	9.12E-2	1.36E-1
	4.5	4.37E-2	2.47E-2	1.19E-1	1.68E-1	2.00E-1	2.33E-1	2.75E-1
	8.0	8.91E-2	9.01E-2	1.47E-1	1.83E-1	2.11E-1	2.39E-1	3.66E-1

Appendix D-3. Bending moment response surface – busbar adjacent to weld region

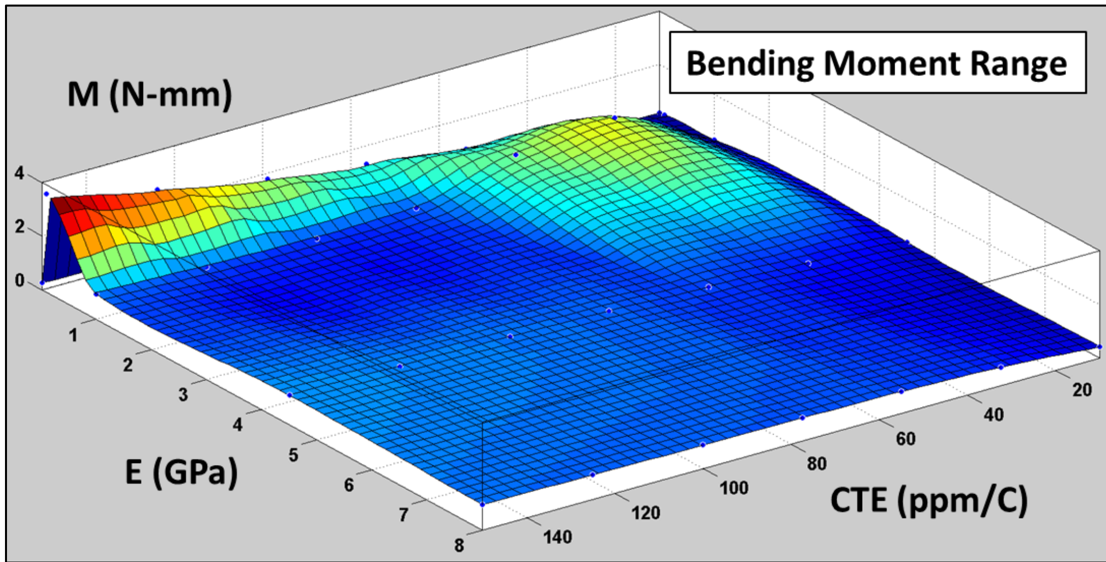

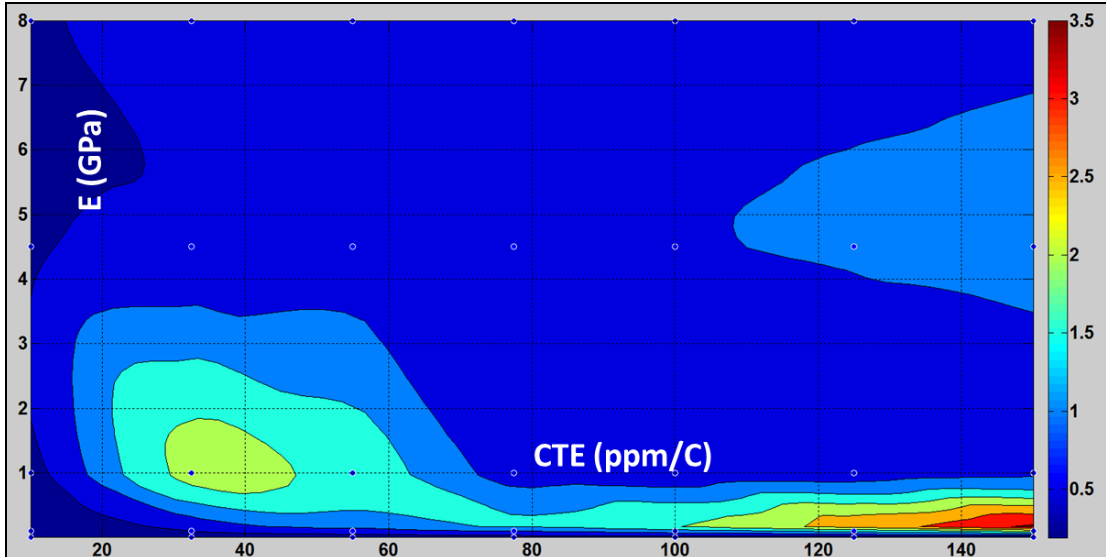

Bending Moment (N-mm)		CTE (ppm/C)						
		10	**32.5**	**55**	**77.5**	**100**	**125**	**150**
E (GPa)	**0.01**	1.91E-1	2.27E-1	2.73E-1	3.25E-1	3.37E-1	3.11E-1	2.64E-1
	0.1	2.30E-1	5.78E-1	1.00E+0	1.46E+0	1.95E+0	2.68E+0	3.67E+0
	1.0	3.08E-1	2.14E+0	1.80E+0	8.36E-1	7.35E-1	7.97E-1	9.30E-1
	4.5	4.04E-1	6.43E-1	7.83E-1	9.11E-1	9.81E-1	1.03E+0	1.09E+0
	8.0	4.40E-1	7.07E-1	8.27E-1	8.64E-1	8.83E-1	9.08E-1	9.46E-1

Appendix E. Meshes of local component region for each configuration in the characterization study

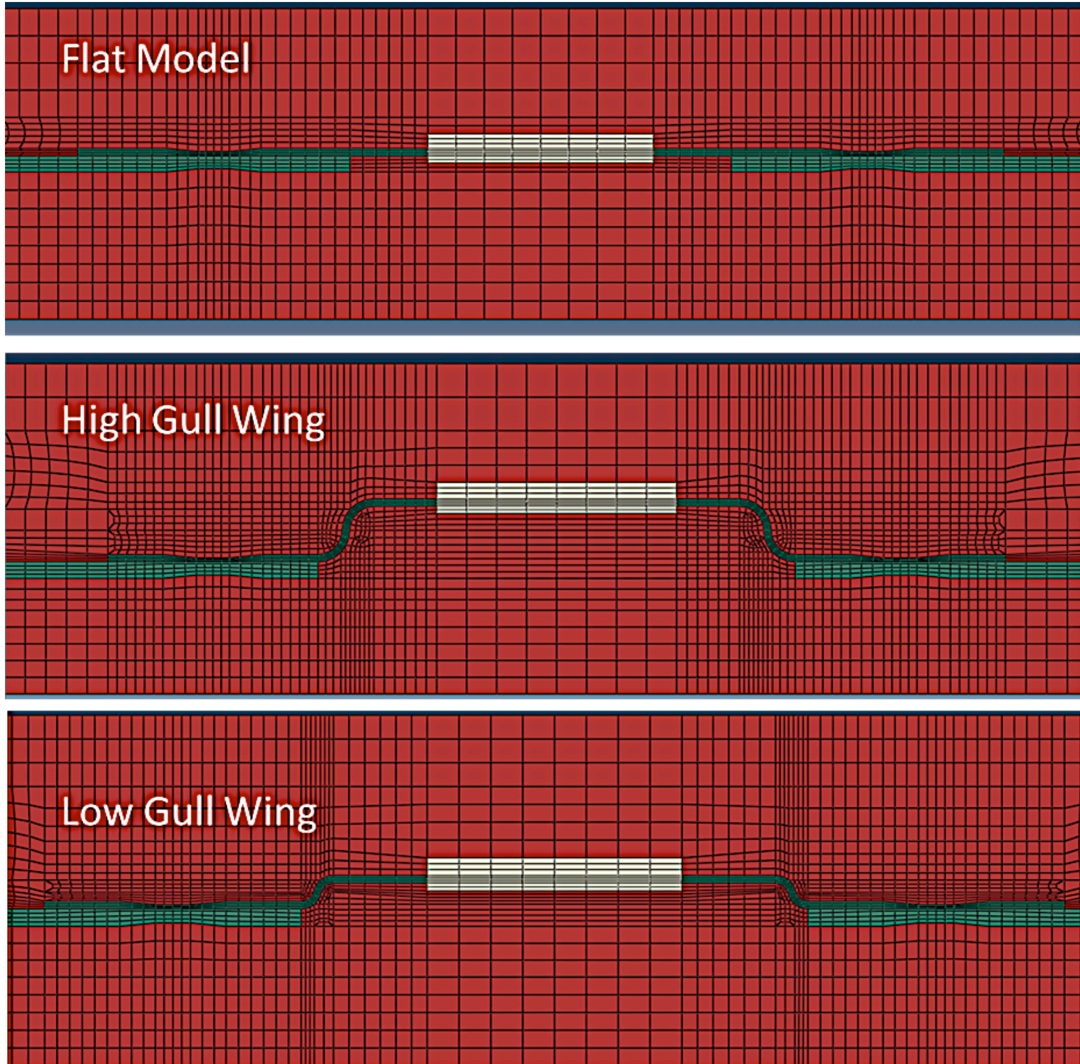

Appendix F-1. L_{27} Main effect plots for individual locations

Factor	A	B	C	D
Parameter	Encapsulant Material Property	Stress Relief Type	Busbar Out-of-Plane Thickness	Encapsulant Out-of-Plane Thickness

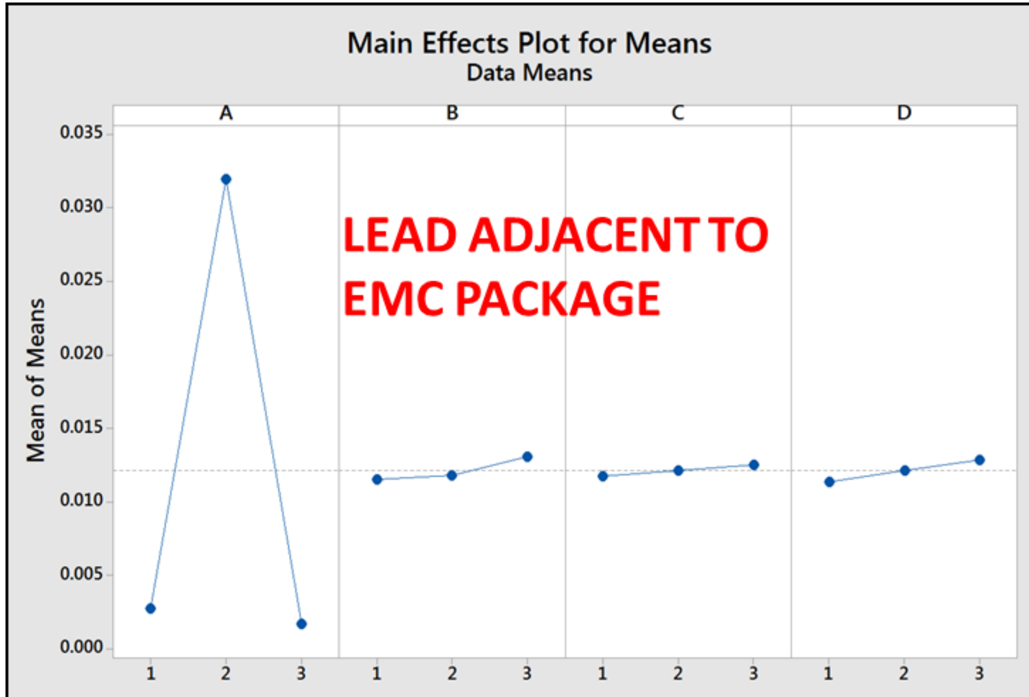

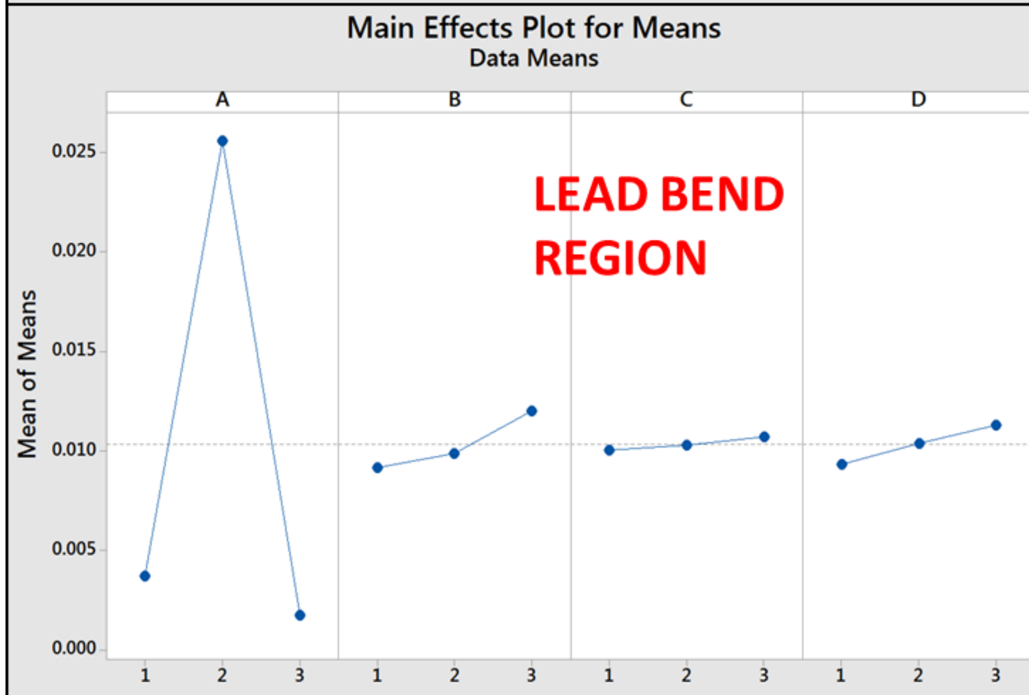

Appendix F-1. L_{27} Main effect plots for individual locations

Factor	A	B	C	D
Parameter	Encapsulant Material Property	Stress Relief Type	Busbar Out-of-Plane Thickness	Encapsulant Out-of-Plane Thickness

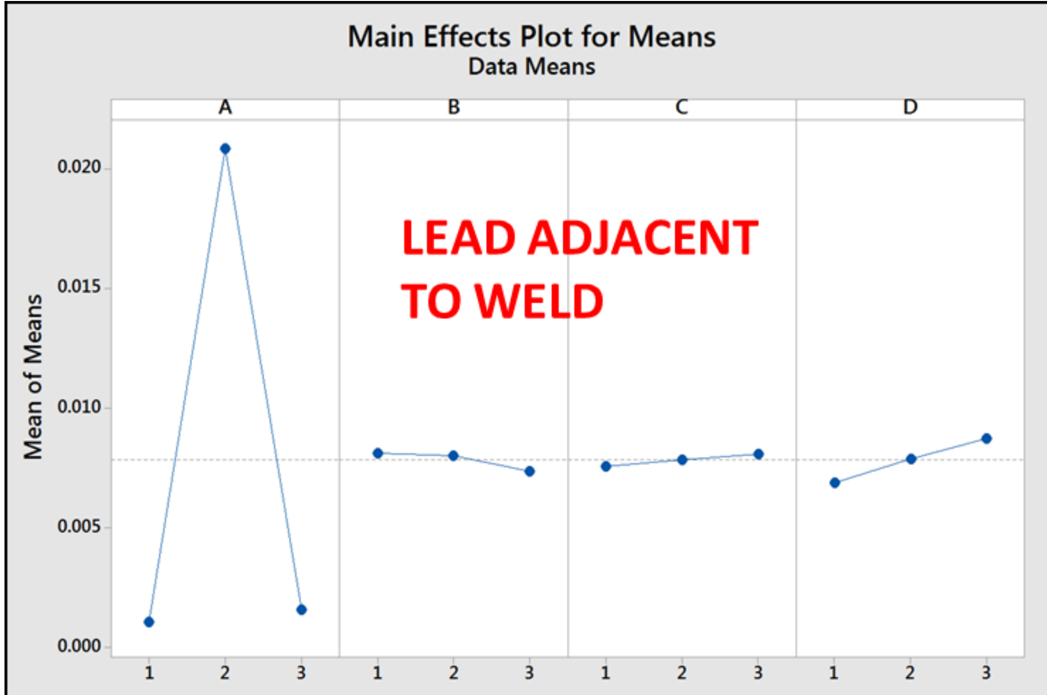

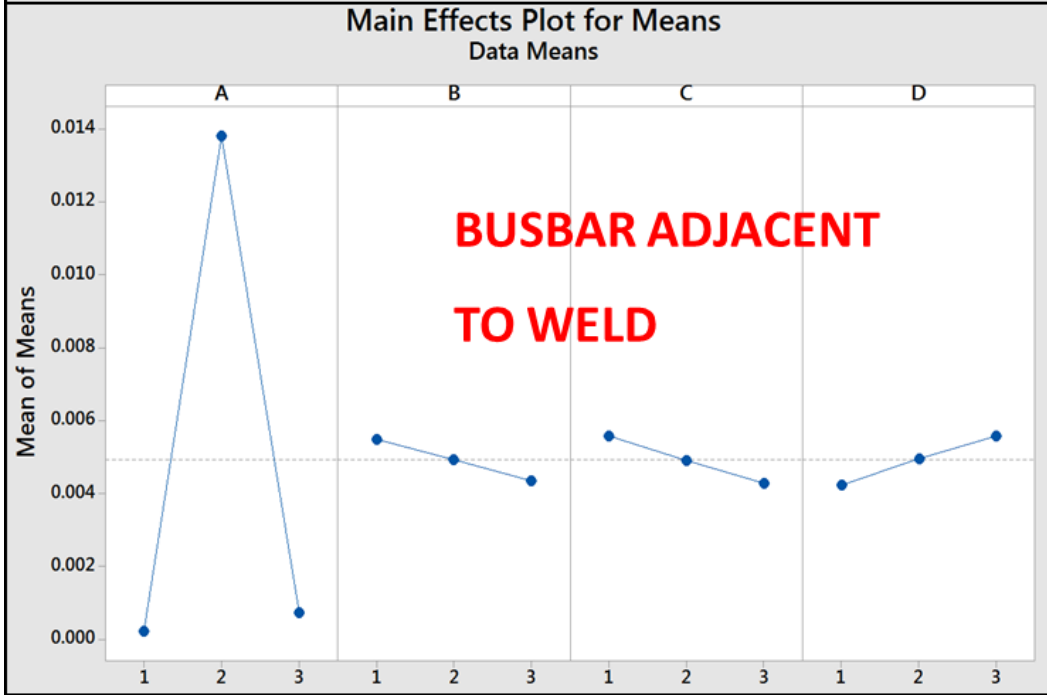

Appendix F-2. L_{27} Parameter plots for individual locations

Factor	A	B	C	D
Parameter	Encapsulant Material Property	Stress Relief Type	Busbar Out-of-Plane Thickness	Encapsulant Out-of-Plane Thickness

LEAD ADJACENT TO EMC

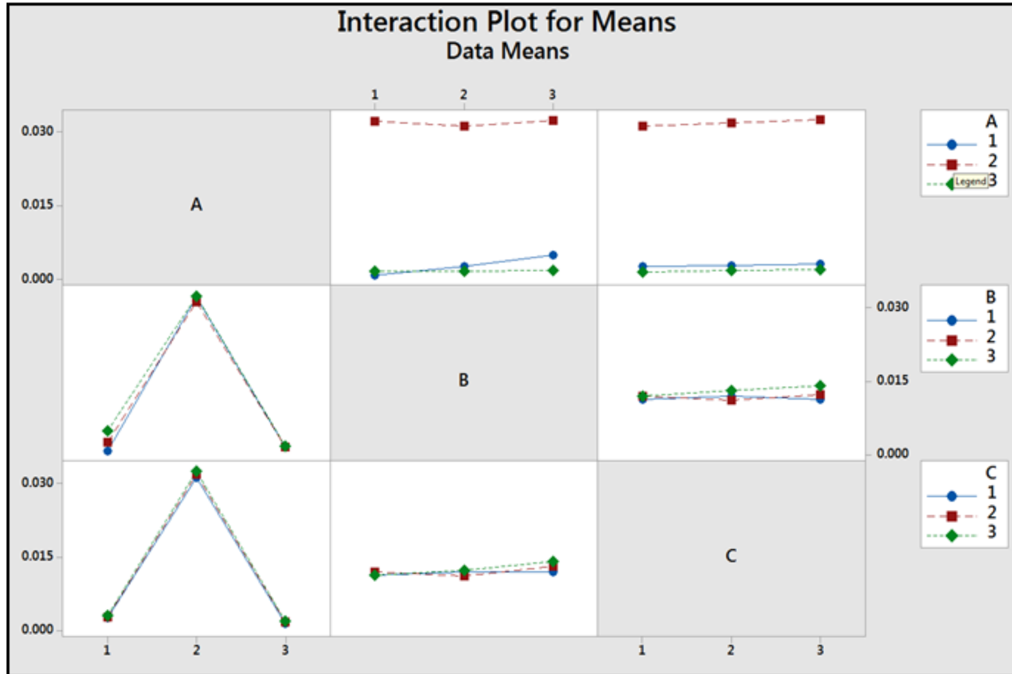

LEAD BEND REGION

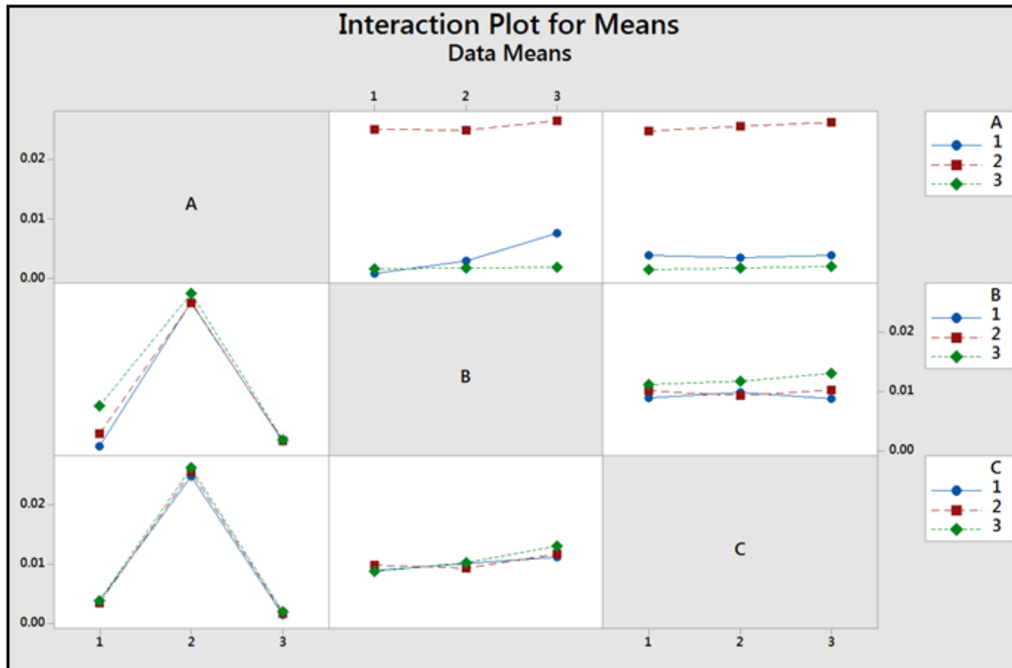

Appendix F-2. L_{27} Parameter plots for individual locations

Factor	A	B	C	D
Parameter	Encapsulant Material Property	Stress Relief Type	Busbar Out-of-Plane Thickness	Encapsulant Out-of-Plane Thickness

LEAD ADJACENT TO WELD

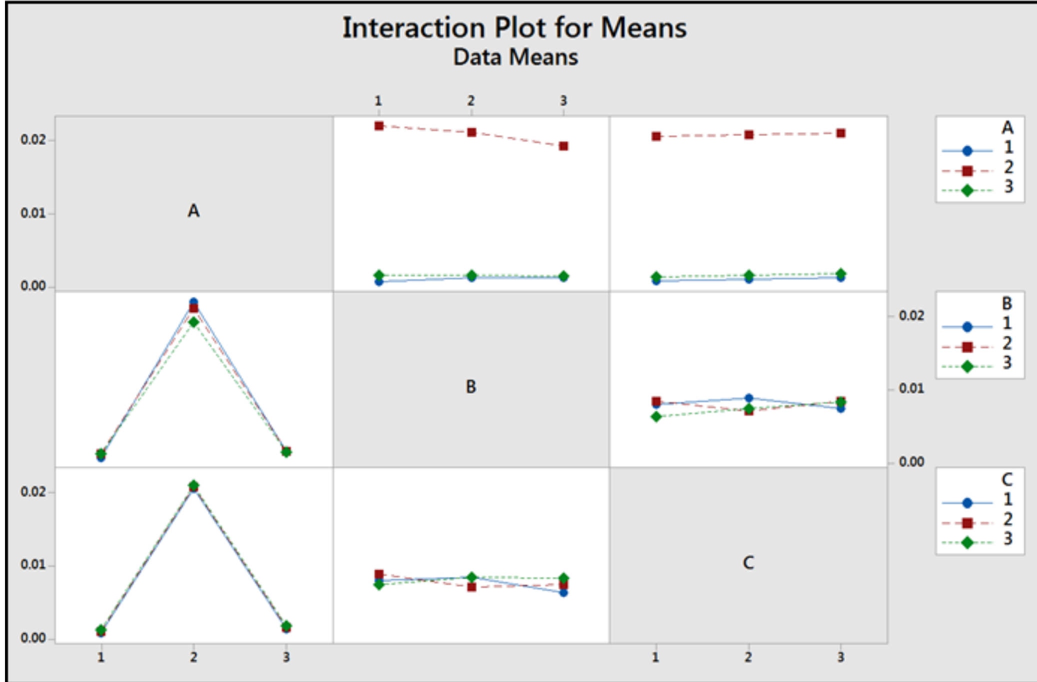

BUSBAR ADJACENT TO WELD

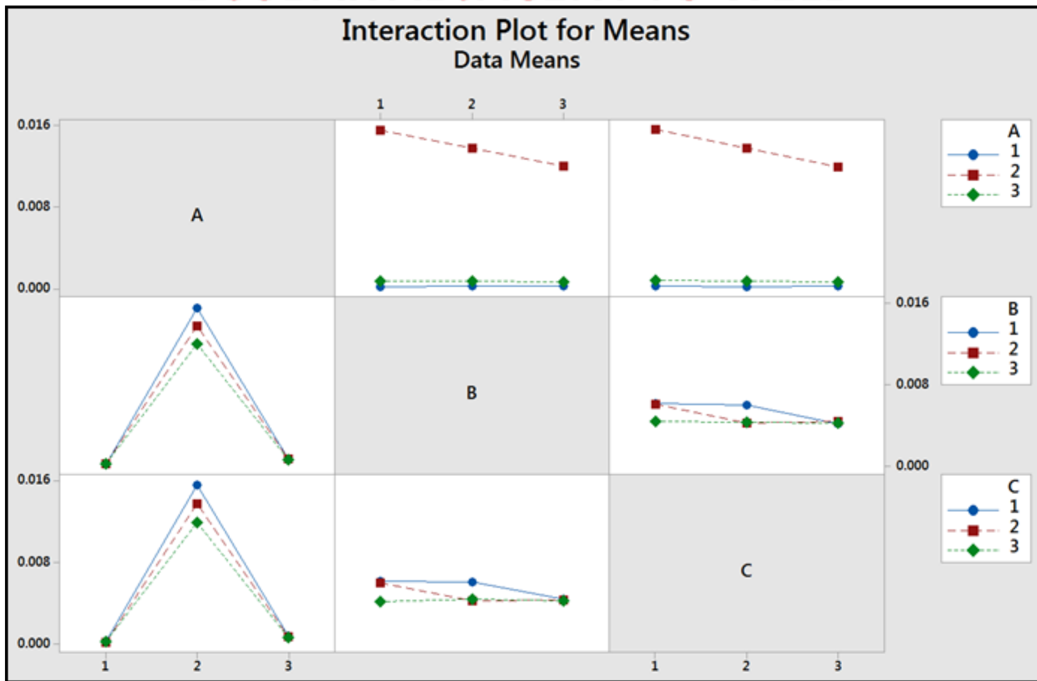

Bibliography

[1] Dowling, N.E., *Mechanical Behavior of Materials*, 2nd Edition, Upper Saddle River, New Jersey, 1999.

[2] Lee, K.J., "Fabrication and Reliability Assessment of Embedded Passives in Organic Substrate," Master's Thesis, Georgia Institute of Technology, 2005.

[3] Qiu W., Pan K., Yuan C., and Wang J., "Study on Reliability of Embedded Passives in Organic Substrate", Proc 10th International Conference on Electronic Packaging Technology & High Density Packaging, Beijing, China, Aug. 2009, pp124-127.

[4] Chen, Qian *et al.*, "Thermo and Mechanical Study on Integrated High-density Packaging," ICEPT-HDP 2008, pp. 1-4.

[5] Suryanarayana, D., Hsiao, R., Gall, T.P., McCreary, J.M., "Flip-chip solder bump fatigue life enhanced by polymer encapsulation," 40th Electronic Components and Technology Conference, May 1990, vol. 1, pp.338-344.

[6] Okura, J., Shetty, S., Dasgupta, A., Caers, J., Reinikainen, T., "Guidelines to Select Flip Chip Underfill and Compliant Interposers for CSP Assemblies," *Intl Journal of Microelectronics Reliability*, Vol. 40, pp. 1173-1180, 2000.

[7] Darbha, K., Okura, J., Shetty, S., Dasgupta, A., Reinikainen, T., Zhu, J., Caers, J., "Thermomechanical Durability of Flip Chip Interconnects with underfill," ASME Journal of Electronic Packaging, Vol. 121, pp. 237-242, 1999.

[8] Zhong, Z., "Reliability of FCOB with and without encapsulation," Soldering & Surface Mount Technology, 2001, vol. 13, no. 2, pp.21-25.

[9] Young, S. J., "Underfilling BGA for Harsh Environment Deployment," Proceedings of the 1999 International Conference on High Density Packaging and MCMs, pp. 409-413, Denver, CO, April 6-9, 1999.

[10] Burnette, T., Johnson, Z., Koschmieder, T., and Oyler, W., "Underfilled BGAs for Ceramic BGA Packages and Board Level Reliability," Proceedings of the 2000 Electronic Components and Technology Conference, pp. 1221-1226, Las Vegas, NV, May 30 - June 2, 2000.

[11] Pippola, J., Marttila, T., and Frisk, L., "Effect of protective casting materials on product level reliability under accelerated test conditions," 2013 European Microelectronics Packaging Conference (EMPC), Sept. 2013, pp.1-6.

[12] Zhang, Q., "A novel solder ball coating process with improved reliability," Proceedings. 55th Electronic Components and Technology Conference, Vol. 1, pp.399-405, May-June 2005.

[13] Licari, J.J., *Coating Materials for Electronic Applications - Polymers, Processes, Reliability, Testing.* William Andrew Publishing/Noyes, 2003.

[14] Fillion, R.A., Wojnarowski, R.J., Gorcyzca, T.B., Wildi, E.J., Cole, H.S., "Development of a plastic encapsulated multichip technology for high volume, low cost commercial electronics," Components, Packaging, and IEEE Transactions on Manufacturing Technology - Part B: Advanced Packaging, Feb 1995, vol.18, no.1, pp.59-65.

[15] Thomas, T., Becker, K.F., Dijk, M.v., Wittler, O., Braun, T., Bauer, J., Lang, K.D., " Reliability assessment of molded Smart Power Modules," 8th International Conference on Integrated Power Systems (CIPS), Feb. 2014, pp.1-8.

[16] Sarvar, F., Teh, N.J., Whalley, D.C., Huntt, D.A., Palmer, P.J., "Thermo-mechanical modelling of polymer encapsulated electronics," The Ninth Intersociety Conference on Thermal and Thermomechanical Phenomena in Electronic Systems (ITHERM), June 2004, vol.2, pp.465,472.

[17] Takei, Y., Ueda, K., Hisanaga, N., Nakata, H., Ishii, K., Nagi, T. Okuno, A., "Unique high reliability urethane resin for car electronic module packaging," *IEEE 9th VLSI Packaging Workshop of Japan (VPWJ). Dec 2008*. pp.109,112.

[18] Simpson, R., Gehrke, F., Holt, M., "Molded interconnects for high reliability undersea connector interfaces," OCEANS 2009, MTS/IEEE Biloxi - Marine Technology for Our Future: Global and Local Challenges , Oct. 2009, pp.1-7.

[19] Parsa, E., Huang, H., Dasgupta, A., "Multi-physics simulations for combined temperature/humidity cycling of potted electronic assemblies," 14th International Conference on Thermal, Mechanical and Multi-Physics

Simulation and Experiments in Microelectronics and Microsystems (EuroSimE), April 2013, pp.1-6, 14-17.

[20] Thakur, S., Kaisare, A., Tonapi, S., "Thermo-mechanical analysis of a typical solar module: A parametric study," 13th IEEE Intersociety Conference on Thermal and Thermomechanical Phenomena in Electronic Systems (ITherm), 2012, pp.1255-1263.

[21] Akman, J., Choi, C., Mukherjee, S., Meng, J., Mirbagheri, E., Haddad, G., Das, D., Dasgupta, A., Gaston, R., Kauffmann, K., Feng, J., Liu, H., Ramesh, N., "Durability assessment of photovoltaic (PV) products under environmental thermal cycling," 13th IEEE Intersociety Conference on Thermal and Thermomechanical Phenomena in Electronic Systems (ITherm), 2012, pp.1264-1273.

[22] Kraemer, F., Wiese, S., "FEM stress analysis of various solar module concepts under temperature cycling load," 15th international conference on Thermal, mechanical and multi-physics simulation and experiments in microelectronics and microsystems (eurosime), April 2014, pp.1-8.

[23] D. D. L. Chung, *Materials for Electronic Packaging*, Newton: Butterworth-Heinemann, 1995.

[24] Pecht, M. G., *et al., Electronic Packaging: Materials and Their Properties*, Boca Raton: CRC Press LLC, 1999.

[25] Harper, C. A., *Electronic Packaging and Interconnection Handbook*, New York: McGraw-Hill, 2000.

[26] Lau, J., *et al.*, *Electronic Packaging: Design, Materials, Process, and Reliability*, New York: McGraw-Hill, 1998.

[27] Ardebili, H. and Pecht, M. G., *Encapsulation Technolgoies for Electronic Applications*, Oxford: William Andrew, 2009.

[28] Peace, G. S., *Taguchi Methods*, Oxford: Addison-Wesley Publishing Company, Inc., 1993.

[29] Montgomery, D. C., *Design and Analysis of Experiments*, Oxford: John Wiley & Sons, Inc., 2005

[30] Kim, H.S., “A combined FEA and design of experiments approachfor the

design and analysis of warm forming of aluminum sheet alloys," The International Journal of Advanced Manufacturing Technology, Nov. 2010, Vol. 51, Issue 1-4, pp. 1-14.

[31] Rao, T.B., and Krishna, A.G., "Design and Optimization of Extrusion Process Using FEA and Taguchi Method," International Journal of Engineering Research & Technology (IJERT), Oct. 2012, Vol. 1, Issue 8.

[32] Lu, X., Chen, L., Cheng, Z., Liu, J. "Reliability analysis of embedded chip technique with design of experiment methods," International Symposium on Electronics Materials and Packaging (EMAP), Dec. 2005. pp.43-49.

[33] Hsieh, M.C., Lee, W., "FEA modeling and DOE analysis for design optimization of 3D-WLP," 2nd Electronics System-Integration Technology Conference (ESTC), Sept. 2008. pp.707-712.

[34] Dasgupta, A., Pecht, M.G., Mathieu, B., "Design-of-experiment methods for computational parametric studies in electronic packaging," Finite Elements in Analysis and Design, Vol.30, Issues 1–2, July 1998, pp. 125-146.

[35] Guofeng, X., Fei, Q., Si, C., Tong, A., "Thermal fatigue reliability design of solder bumps in TSV interposer package based on finite element analysis," 14th International Conference on Electronic Packaging Technology (ICEPT), Aug. 2013, pp.517-520.

[36] Kotlowitz, R. W., "Comparative Compliance of Generic Lead Designs for Surface Mounted Components," Proceedings 1987 International Electronics Packaging Society Conference, Boston, MA, November 9-11, 1987, Vol. 2, pp. 965-984. Reprinted in Proceedings 1988 National Electronic Packaging and Production Conference, NEPCON East, Boston, MA June 14-16, 1988, pp. 95-120, and International Electronics Packaging Society Journal, Vol. 10, No. 1, pp. 7-19.

[37] Kotlowitz, R. W., and Engelmaier, W., "Impact of Lead Compliance on the Solder Attachment Reliability of Leaded Surface Mounted Devices," Proceedings 1986 International Electronics Packaging Society Conference, San Diego, CA, November 17-19, 1986, pp. 841-865.

[38] Kotlowitz, R. W., "Compliance Metrics for Surface Mount Component Lead Design," Proceedings 1990 IEEE Electronic Components and Technology Conference, Las Vegas, NV, May 21-23, 1990, Vol. 2, pp. 1054-1063.

[39] Emerick, A., Ellerson, J., McCreary, J., Noreika, R., Woychik, C., Viswanadham, P., "Enhancement of TSOP solder joint reliability using encapsulation," 43rd Proceedings. Electronic Components and Technology Conference, June 1993, pp.187-192.

[40] Cummings, D. A., " Quantitative Comparison of Electronic Component/Solder Joint Stress Relief in Encapsulated Assemblies," IEEE, Transactions on Components, Hybrids, and Manufacturing Technology. Dec 1979. Vol. 2, No. 4.

[41] Dais, J., and Howland, F., "Fatigue Failure of Encapsulated Gold-Beam Lead and TAB Devices," *IEEE Transactions on Components, Hybrids, and Manufacturing Technology,* vol.1, no.2, pp.158-166, June 1978.

[42] Lau, J.H. Rice, D. and Harkins, C.G., "Thermal stress analysis of tape automated bonding packages and interconnections," 39th Proceedings of the Electronic Components Conference. pp.456-463, May 1989.

[43] Hewlett-Packard Application Note 993-1, Thermal Stress Relief In Beam Lead Diode Assembly. http://www.hp.woodshot.com/hprfhelp/4_downld/lit/diodelit/ an993-1.pdf

[44] http://www.diodes.com/datasheets/SBR12U45LH.pdf

[45] http://www.personal.psu.edu/users/j/h/jhk5143/edesgn100/project4/welding/index.html

[46] Hewlett-Packard Application Note 992, Beam Lead Attachment Methods. http://www.hp.woodshot.com/hprfhelp/4_downld/lit/diodelit/an992.pdf

[47] Dalla Palma, M., "Hardening parameters for modelling of CuCrZr and OFHC copper under cyclic loadings," *IEEE 25th Symposium on Fusion Engineering (SOFE),* pp.1-5, June 2013.

[48] Ayers, L.J., "The Hardening of Tpe 316L Stainless Steel Welds with Thermal Aging," Master's Thesis, Massachuesetts Institute of Technology, 2012.

[49] Alialhoseini, E. and Bahman, A., "Change in hardness yield strength and UTS of welded joints produced in St37 grade steel," *Indian Journal of Science and*

Technology, Vol. 3, no. 12, pp. 1162-1164, 2010.

[50] Mali, V.I., Bataev, A.A., Bataev, I.A., Malyutina, Y.N., Esikov, M.A., Lozhkin, V.S., "Microstructure and mechanical properties of copper-tantalum joints produced by explosive welding," 8th International Forum on Strategic Technology (IFOST), vol.1, pp.9-12, June-July 2013.

[51] JEDEC Solid State Technology Association., JESD22-A104D: *Temperature* Cycling. 2009.